ADDENDA

p.48 A tacit assumption has been made between the first and second sentences of paragraph 1 of section 3-6, namely that collisional processes play an insignificantly small role in deactivating the levels of interest.

p.68, second paragraph

The observation by Jensen, Collins and Bennett, Jr. (to be published) of CW laser action in the transitions at 6102 Å and 6021 Å in Zn II indicates that the lifetime ratio for these transitions, given in table 4.1b, may be in error. The most probable explanation would seem to be that simultaneous laser action in the transitions at 7588 Å and 7733 Å artificially reduces the lifetime of the 5p levels, enabling a population inversion to be established between the 5d and 5p levels (see Figure 3.7). The summary of results on page 49, paragraph 2, should be altered appropriately to include the new C.W. laser transitions mentioned above.

ERRATA

p.10 Last line , for 'Furguson' read 'Ferguson'.

p.11 First line, for 'rear-sonic' read 'near-sonic'.

Third line below Equation (1.4), for 'zero-nder' read 'zero-order'.

p.21 Last line, for 'Figure 3-1' read 'Figure 2-1'.

p.22 Second line, for 'focul' read 'focal'.

Second line of paragraph two, for 'Baush' read 'Bausch'.

p.24 Second line, for 'Thom' read 'Thorn'.

p.25 Last line but one, delete 'the'.

p.31 For $6d\,^2D_{5/2}$ column (13) should read 0·075.

p.99 Seventh line, for 'Sorm' read 'orn'.

p.101 Ninth line, for 'A/v' read 'v/A'.

p.119 Second line, for 'β' read 'β_i'.

p.123 Columns (4) and (5), for 'C arbitrary constant' read 'k arbitrary constant'.

p.135 Seventh line should read 'than with either helium or neon.'.

INVESTIGATIONS OF THE PRODUCTION OF EXCITED STATES IN IONS

A. R. Turner-Smith

ABSTRACT

Excitation by thermal energy charge transfer has been postulated as the pumping mechanism responsible for laser action in certain transitions of the recently announced He-Cd and He-Zn laser systems. In this thesis a study of these reactions and others of the same class is presented. The technique employed in the present work overcomes the difficulty in interpretation of data present in previously published studies of this class of reaction, which arose from the failure to distinguish between charge transfer excitation, electron collisional excitation and Penning excitation. The reactions are studied in a flowing afterglow of a rare gas under conditions such that the plasma electrons have insufficient energy to cause appreciable optical excitation. Discrimination between excitation due to charge transfer and Penning reactions is achieved by selective modulation of the relevant reactant particle concentrations. Measurement of the relative emission intensities of transitions in the daughter metal ion enables the relative charge transfer rate to each level in the ion to be determined.

A review is presented of the current state of theories of thermal energy charge transfer reactions. In particular, the prediction that the cross-section should be largest for reactions in which the energy defect is positive and of order 1000 cm^{-1} is found to be in accord with the experimental results. Further experimental conclusions relate to the influence of statistical weight and spin of the final level on the reaction rate. Evidence is presented that in certain cases a third body may enhance the reaction rate.

INVESTIGATIONS OF THE PRODUCTION OF EXCITED STATES IN IONS

A. R. Turner-Smith

Oriel College

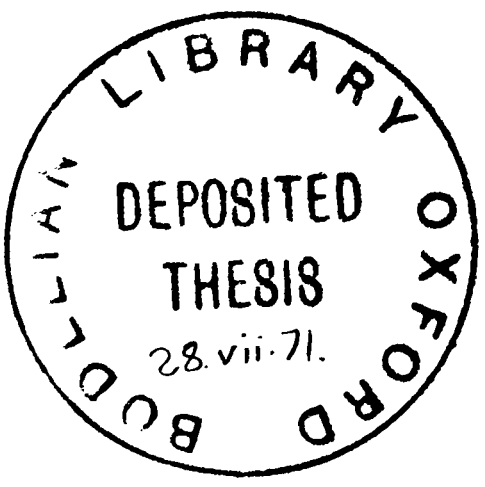

A thesis submitted for the degree of Doctor of Philosophy in the University of Oxford

Clarendon Laboratory
Oxford

Hilary Term 1971

To my wife

'Only when genius is married to science can the highest results be produced.'

Herbert Spencer

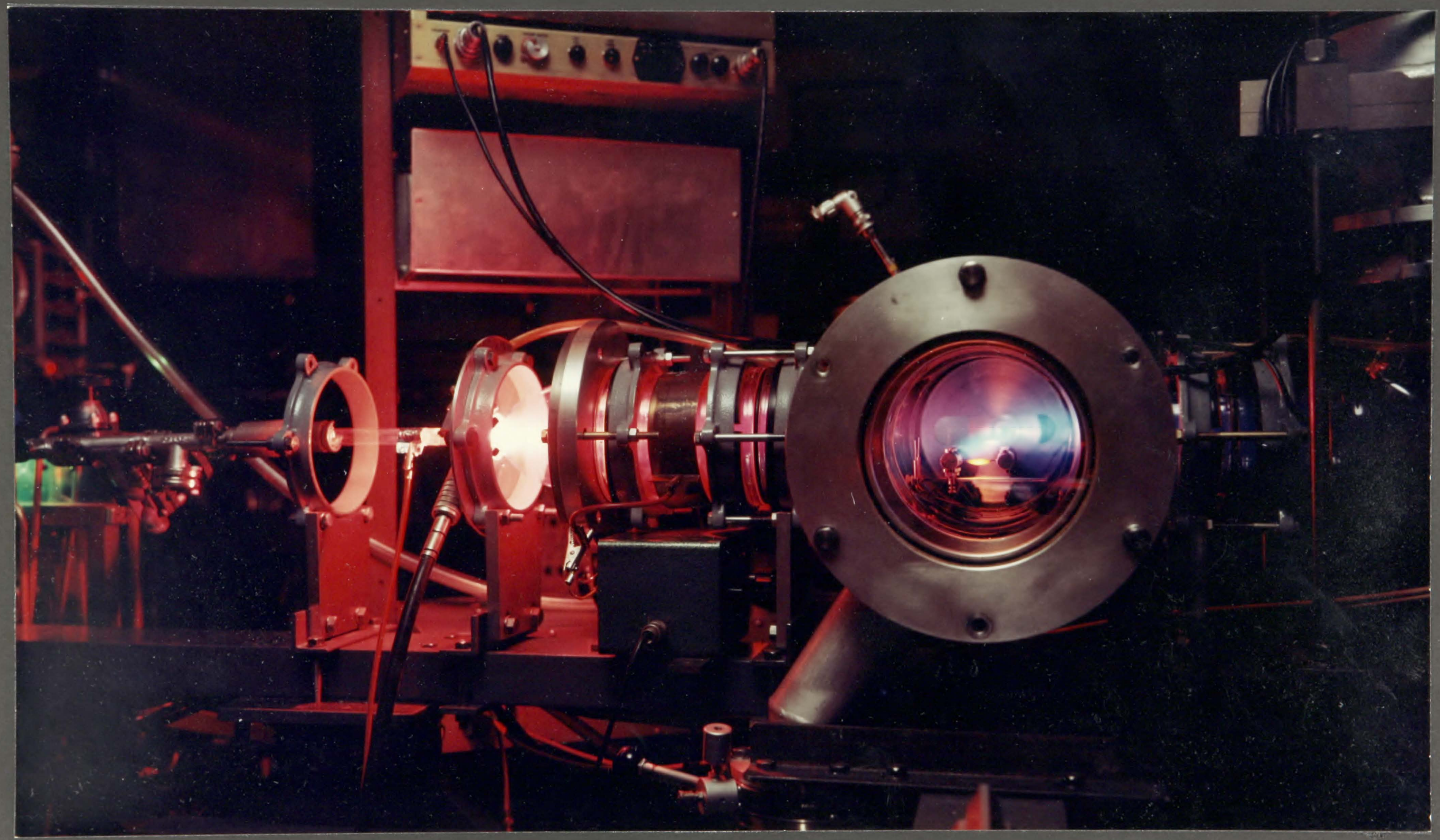

Figure P1 Magnesium in a Neon Afterglow

CONTENTS

	Figure P1	3
Chapter 1	INTRODUCTION	6
1-1	Motivation	7
1-2	Early Work	8
1-3	The Flowing Afterglow Method	10
	References	12
	Figure 1.1	13
Chapter 2	APPARATUS	14
2-1	Introduction	15
2-2	The Pumping System	15
2-3	The Flow Tube	16
2-4	The Gas Control Bench	18
2-5	The Primary Discharge	19
2-6	R.F. Reheating	20
2-7	The Reaction Region	21
2-8	The Optical System	22
2-9	The Photomultipliers	22
2-10	Calibration of the Optical System	23
2-10.1	Standard Lamps	24
2-10.2	Calibration Procedure	24
2-10.3	Spectral Response	25
	References	26
	Table 2.1	27
	Figures P2 to P6	28-32
	Figures 2.1 to 2.6	33-36
Chapter 3	PRELIMINARY EXPERIMENTS	37
3-1	The Flowing Afterglow	38
3-2	Probe Measurements	40
3-3	Initial Experiments with Zinc	42
3-4	Penning Reactions	45
3-5	Charge Transfer/Penning Reaction Discriminants	46
3-6	Preliminary Results, Zinc & Cadmium	48
3-7	3-body Reactions	49
	References	53
	Figures 3.1 to 3.10	54-63
Chapter 4	RESULTS	64
4-1	Further Experimental Details	65
4-2	Calculations on the Data	66
4-2.1	Theoretical Branching Ratios	66
4-2.2	Extended Calibration	67
4-2.3	Accuracy	67
4-3	Zinc	67
4-3.1	Helium-Zinc	67
4-3.2	Neon-Zinc, Argon-Zinc	68

Chapter 4-4		Cadmium	69
	4-4.1	Helium-Cadmium	69
	4-4.2	Neon-Cadmium and Argon Cadmium	71
	4-5	Magnesium	71
	4-6	Selenium	72
	4-7	Other Metals	74
	4-7.1	Aluminium	74
	4-7.2	Lead	75
	4-7.3	Manganese	75
		References	76
		Notes on the Tables	77
		Table 4.1 Helium-Zinc	79
		Table 4.2 Neon-Zinc	82
		Table 4.3 Helium-Cadmium	84
		Table 4.4 Neon-Magnesium	88
		Table 4.5 Helium-Selenium	92
		References to Tables	95
		Figure 4.1	96
Chapter 5		THEORY	97
		Symbols used frequently in Chapter 5	98
	5-1	Introduction	99
	5-2	Semi-classical theories	100
	5-2.1	The Adiabatic Hypothesis	100
	5-2.2	Langevin Orbiting	102
	5-2.3	Limitations of the Adiabatic Hypothesis	103
	5-3	Quantum Mechanical Theories	104
	5-3.1	Starting Equations	104
	5-3.2	Zone Formulation - Stueckelberg Method	106
	5-3.3	Zone Formulation - Demkov Method	107
	5-3.4	Zone Formulation - Rapp and Francis Method	108
	5-3.5	Curve Crossing Formulation - the SLZ Formula	110
	5-3.6	SLZ Formula - Applications	113
	5-4	Discussion	116
	5-4.1	Regions of Application	116
	5-4.2	Conclusions	117
	5-4.3	A Numerical Example	119
		References	121
		Tables 5.1 and 5.2	123, 124
		Figures 5.1 and 5.9	125-130
Chapter 6		CONCLUSIONS	131
	6-1	Statistical Weight	132
	6-2	Energy Defect	133
	6-3	Spin	134
	6-4	Reduced Mass	134
	6-5	3-body Reactions	135

Chapter 6-6	Summary	135
	References	136
	Figure 6.1	137
	APPENDIX	138
Appendix 1	Floating Double Probes	139
	Figures A1.1 and A1.2	141
Appendix 2	Orbiting Limitations	142
Appendix 3	Existence of a Critical zone	144
	ACKNOWLEDGEMENTS	145

CHAPTER 1

INTRODUCTION

'The thing to do is to supply light and not heat'

Woodrow Wilson

CHAPTER I

Introduction

1-1 MOTIVATION

A new class of laser excitation mechanism was announced in September 1968 with the publication of the discovery of continuous laser action in cadmium[1]. The mechanism responsible for pumping the laser transition at 4416Å in Cd II was postulated to be a Penning reaction:

$$He\ (2\ ^3S_1) + Cd \rightarrow He + Cd^+\ (5s^2\ ^2D_{5/2}) + e^- + 18,053\ cm^{-1} \qquad (1.1)$$

Shortly afterwards continuous laser action in zinc was announced[2] in which the mechanism responsible for pumping the transition at 7588Å in Zn II was suggested to be charge transfer e. g:

$$He^+ + Zn \rightarrow He + Zn^+\ (5d\ ^2D_{5/2}) + 4,545\ cm^{-1} \qquad (1.2)$$

Prior to the announcement of the c w laser transitions in zinc, work had already begun on these studies which were designed to evaluate the possibility that charge transfer reactions might provide an efficient pumping mechanism for metal ion laser transitions. The potential for improving the power of c w lasers pumped by Penning reactions appeared to be slight, for they would presumably suffer from the same power limitation, due to saturation of the helium metastable population, as in the helium-neon laser[3]. The charge transfer mechanism showed greater promise as no comparable limit to the density of the pump species (ions) exists. It might be expected, therefore, that charge transfer would combine the efficiency of a selectively pumped c w gas laser system without a corresponding inherent power limitation.

The main body of experimental evidence concerning charge transfer reactions, available in the literature at the outset of the project, was comprised in the work of Duffendack and co-workers[4], which indicated

that charge transfer from rare gas ions to excited states in metal atoms did occur with high efficiency. The interpretation of this data, however, was by no means straightforward (Section 1-2). It was decided, therefore, that a study should be made of charge transfer at thermal energies from the point of view of the atomic physics of these reactions, in the hope that criteria for new laser transitions would become apparent. This hope has largely been fulfilled in that the new laser transitions since discovered in Zn II and Cd II are just those which might be expected on the basis of this study.

1-2 EARLIER WORK

The reactions of interest are of the type

$$X^+ + M \rightarrow X + M^{+*} + \Delta \qquad (1.3)$$

in which X^+ and X denote the ground state species of the ion and atom of an element of high ionization potential (a rare gas in the experiments to be described) and M and M^{+*} denote the ground atomic and excited state of the singly ionised species of an element of lower ionization potential (a metal in the experiments to be described). The energy defect, Δ , between the initial and final states of the system at infinite inter-nuclear separation is usually positive.

Two established methods were available for the study of atomic collisions: atomic beam and drift tube experiments. Neither of these were particularly well adapted to this investigation since neither is capable of producing reaction rates sufficient to permit photometric detection. This is due to the small solid angles available to the required optical detection systems.

The method employed by Duffendack and co-workers[4] was to introduce a small quantity of metal vapour into an active discharge of a rare

gas. The differential (rare gas) pressure-dependence of intensity among the various transitions in the spectrum of the singly ionised metal was attributed to selective excitation, involving charge transfer from the rare gas. The relevent conclusions from this work may be summarised as follows:

i) The cross-section is maximised for zero energy defect.

ii) There is a sharper decrease of cross-section for increasing negative values of energy defect than for positive.

iii) The cross-section depends on the total angular momentum of the final state.

iv) The cross-sections concerned are large. The order of magnitude for the Ne-Mg reaction was estimated to be 10^5 $\mathring{A}^2$.

These findings are illustrated by Figure 1.1 in which data of Manley and Duffendack[4] for the Ne-Mg reaction are reproduced.

With the benefit of hindsight, the shortcomings of the technique used by Duffendack and co-workers become apparent. Apart from the impediment of photographic intensity measurements no means were available to permit resolution of contributions due to:

a) direct excitation by collisions of electrons with neutral metal atoms or ions,

b) Penning excitation (such as in Equation (1.1)),

c) excitation by charge transfer (such as in Equation (1.2)).

It is by no means certain that the differential pressure dependence observed could not have resulted from changes in the electron collisional excitation contribution arising from pressure dependence of the electron temperature or density in the discharge. Nevertheless, although the total reaction cross-section quoted for the Ne-Mg reaction is of an altogether incredible magnitude, the results presented in this thesis will be seen largely to bear out conclusions ii) and iii) above.

However, contrary to conclusion i), the present observations confirm the prediction of more recent theories which find that the cross-section reaches its maximum value for a small positive value of the energy defect.

It was clear at the outset of the present work that the method chosen to study charge transfer reactions must be one in which the contribution to the excitation rate due to electron collisions is negligible or clearly separable from the charge transfer contribution. A possible approach would have been to perform time-resolved measurements on the late afterglow of a pulsed discharge in a rare gas, seeded with a small quantity of metal vapour. In the late afterglow electrons would be expected to be insufficiently energetic to cause appreciable optical excitation, but rare gas ions would still be available in large numbers.

The disadvantage of such an approach is that it would require a high density of ions of high ionisation potential to be generated in the presence of atoms of a lower ionisation potential. The very low density of metal vapour consequently required would give rise to a very low reaction rate, the time resolved measurements of which would present extreme problems in detection sensitivity.

The technique adopted for the present work is that of the flowing afterglow, in which the afterglow is separated from the active discharge both in space as well as time.

The technique permits any quantity of metal vapour to be added without reduction of the initial rare gas ion density and allows continuous optical measurements of a system which is in dynamic equilibrium.

1-3 THE FLOWING AFTERGLOW METHOD

The flowing afterglow technique, previously employed in the study of reactions of atmospheric interest, has been described in detail in a recent review article by Ferguson, Fehsenfeld and Schmeltekopf[5].

The technique involves a rear-sonic flow of rare gas in which a strong discharge is generated, either in the body of a wide bore flow tube or just prior to entering it. The reactant gas or vapour is introduced into the flowing afterglow of this discharge in a reaction zone some distance further down the flow tube, corresponding to a later time in the decay of the plasma, when the electrons have thermalised to near room temperature.

The regime of gas pressure, flow velocity and tube diameter under which the method can be successfully operated is delineated by the need to preserve a high axial ion density in the flow tube. Since the dominant ion loss mechanism is ambipolar diffusion to the walls, it can be shown[5] that the axial ion density is proportional to $e^{-t/\tau}$ with t the time for the plasma to travel from the discharge and τ given by

$$\tau = \frac{r^2 P}{(2.405)^2 D_a} \qquad (1.4)$$

in which r is the radius of the flow tube, P is the pressure, D_a is the ambipolar diffusion coefficient at unit pressure and 2.405 is the first root of the zero under Bessel function, J_c.

Use of Equation (1.4) leads to the evaluation of a minimum mass flow rate of gas in the flow tube (in the viscous flow regime) which is determined solely by specifying a) the minimum separation of the discharge and the reaction zone and b) the tolerable ion loss factor between the discharge and the reaction zone. Assuming a minimum separation in a) of 30 cms, and a loss factor in b) of less than 10, the minimum flow rate calculated from Equation (1.4) is of order 100 torr l/sec of helium, or less for neon and argon.

The higher the operating pressure the lower will be the pumping speed required. However, a competing requirement is that the pressure in the system should not be too high (corresponding to large t), when other Loss mechanisms such as reactions with impurities

in the gas stream, conversion to the molecular ion or recombination may become important. In addition, however, the tube diameter should be as small as possible in order to maintain the highest axial density of ions. The compromise solution will use the smallest diameter tube of large enough conductance to permit the required mass flow rate to be maintained at the necessary pressure of operation, found by other workers to lie in the range 0.3 to 3 torr.

The diagnostic technique most frequently employed in flowing afterglow experiments has been mass spectrometry of the very late afterglow, in which the decay of ion density, as a function of the supply of reactant gas or vapour, leads to a value of the total reaction rate to all possible final states. The advantages of the flowing afterglow system are even more apparent, however, in the experiments to be described, in which optical measurements are employed to determine the relative, rather than absolute rates of reaction, for with this type of measurement extreme purity of the gas and detailed knowledge of the loss mechanisms of the ions are unnecessary.

REFERENCES

1 Silfvast, W.T., Appl. Phys. Lett., 13, 169 (1968)

2 Silfvast, W.T., Appl. Phys. Lett., 15, 23 (1969)

3 White, A.D., and Gordon, E.I., Appl. Phys. Lett., 3, 197 (1963)

4 Duffendack, O.S., and Smith, H.L., Phys. Rev., 34, 68 (1929)
Duffendack, O.S., Henshaw, C.L. and Goyer, M., Phys. Rev., 34, 1132 (1929)

Duffendack, O.S. and Thomson, K., Phys. Rev., 43, 106 (1933)
Manley, J.H. and Duffendack, O.S., Phys. Rev., 47, 56 (1935)

5 Ferguson, E.E., Fehsenfeld, F.C. and Schmeltekopf, A.L., Adv. At. Mol. Phys., 5, 1 (1969)

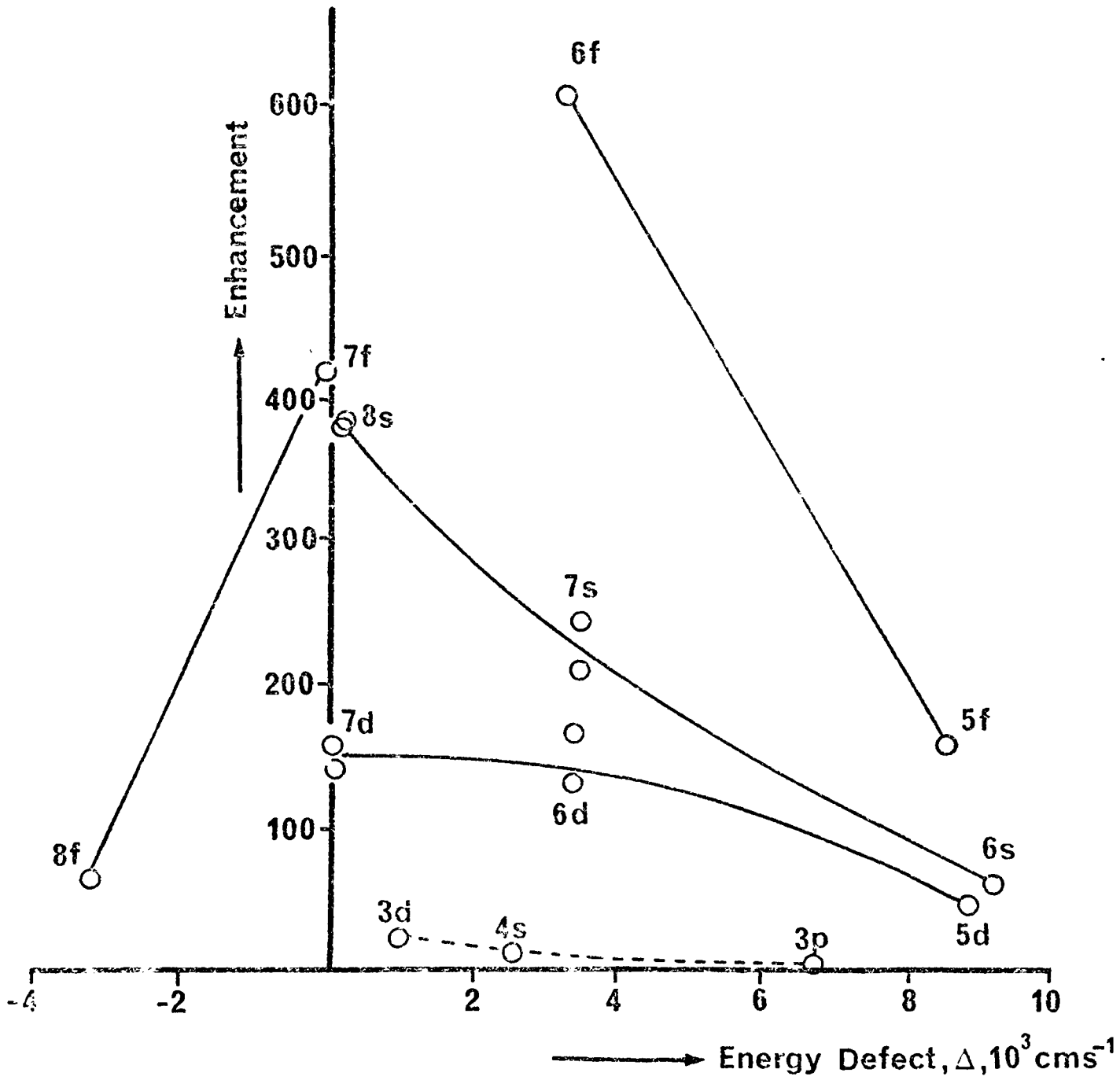

Figure 1.1 - Enhancement of magnesium lines in a magnesium-neon discharge (reproduced from reference 4, Chapter 1)

CHAPTER 2

APPARATUS

'Many things difficult to design prove easy to performance'

Samuel Johnson

CHAPTER 2

APPARATUS

2-1 INTRODUCTION

The general layout of the apparatus is illustrated in figure P.2 and a schematic diagram is shown in Figure 2.1. A high speed mechanical pumping system, coupled to the apparatus via a large diameter pumping line, maintains a near sonic flow of rare gas in a 4" diameter flow tube. At the entrance to this flow tube microwave power from a magnetron oscillator is coupled into the gas by a coaxial line termination, exciting a strong discharge. Metal is evaporated into the flowing afterglow 45 cm downstream from the primary discharge at the reaction region. The light from this region is monitored via silica windows by a Czerny-Turner monochromator equipped with photomultipliers covering the range 2,000-10,000Å. The optical detection system is calibrated for relative spectral sensitivity by use of quartz-bromine lamps of known colour temperature.

2-2 THE PUMPING SYSTEM

In chapter 1 it was shown that the pumping speed requirement would be of the order of 100 torr litres/sec in the afterglow region. To achieve this the pump combination selected was a Roots blower pump (Edwards type ER1000) backed by a large rotary pump (Edwards type ISC3000) which together had a nominal speed of 600 litres/sec in the pressure range 0.03 torr to 6 torr.

The noise and vibration generated by these pumps required them to be installed in a room adjacent to the experimental room, necessitating a pumping line about 6 m in length. This was fabricated from 1/8" aluminium sheet which was rolled and welded into four tubular sections of 8" internal diameter. Three of these sections were identical 90° bends of the maximum possible radius of curvature which connected the apparatus to the pumps in the most direct way possible.

The pump line was itself isolated from vibration of the Roots pump by a section of stainless steel bellows.

The dimensions of the pump line were such that it does not significantly reduce the pump speed[1] at the normal pressures of operation. (> 0.03 torr). Under some experimental conditions it was desirable to reduce the pump speed for which purpose a gate valve was fitted between the end of the pump line and the apparatus. This valve was designed only as a variable conductance element, not as a vacuum-tight seal. It consisted of a plate driven across the pipe by a calibrated rack and pinion drive, which could be reset to reproduce any particular flow conditions.

The ultimate vacuum achieved by a Roots pump is limited by back diffusion and thus depends on the backing pressure. It was found that the best vacuum could be achieved by backing the Roots pump with a small diffusion pump. This pump was isolated from the system whenever an appreciable quantity of gas was being pumped. Using the Roots pump backed by the diffusion pump an ultimate vacuum in the whole system of 3×10^{-5} torr was achieved. Small leaks in the Roots pump itself persisted but these could in no way influence the purity of the afterglow.

Low pressures were measured with an ionisation gauge (Leybold - Elliot). Pressures greater than 1 micron were measured using Pirani gauge heads (L K B 'Autovac') fitted at all key points in the system.

2-3 THE FLOW TUBE

The afterglow flows from the discharge to the reaction region, and on to the pump line, in the flow tube, whose dimensions were chosen to maintain the highest ion density. The internal diameter was 10 cm which was the smallest possible consistent with a conductance at least as large as the pump speed.

The flow tube was constructed of sections of thick wall glass tubing (Q V F Ltd). The advantages of this form of construction were that it provided flexibility in the lay-out of the flow tube and ease of dismantling for cleaning. From the entrance nozzle at the discharge to the pump line the parts, shown in Figure P1, were

i a 6 inch long spacer

ii a cross piece, which provided access to the reaction region in which the metal was evaporated

iii a 'T' piece which connected the flow tube to the pump line and provided another part to which a mass spectrometer was fitted.

Vacuum seals were made using ungreased 'Viton' 'O' rings supported by spacer rings between the ground standard tapered buttress ends of each pipe section.

All these parts, together with the gate valve, were clamped to a single 4 x 2 inch steel channel-section girder 8 feet in length supported by two triangular legs in 2 inch steel box-section. The clamps could be moved to any position along the bench and their height and angle adjusted to allow for small inaccuracies in alignment between the flow tube axis and the bench. At the cross piece an additional length of 4 x 2 inch channel section girder was clamped at right angles to the bench and supported from the floor (Figure P3). This provided support on one side for the collar providing electrical lead-ins and on the other for a 2 inch diffusion pump. Closing the gate valve and pumping the flow tube with the diffusion pump at the cross piece enabled the ultimate vacuum in the flow tube to be improved to 7×10^{-6} torr.

2-4 THE GAS CONTROL BENCH

Gas was supplied to the discharge by the gas control bench in which the gases from high pressure cylinders were cleaned and their flow and pressure regulated. A schematic diagram of the control bench is shown in Figure 2.2.

Cleanliness of the gas supplied to the discharge was of the utmost importance in preserving high ion densities in the late afterglow. Typical analyses of the gases, supplied by the manufacturers, are given in Table 2.1.

Further purification of the gases was accomplished by use of a 'molecular sieve', crystalline sodium alumino-silicate (Union Carbide type 13X in 1/8 inch pellet form). Molecular sieves operate most efficiently in high gas pressures and at low temperatures. In an earlier version of the gas control bench it was possible to isolate the molecular sieves altogether from the system. It was found they did provide an improvement to the cleanliness of the afterglow, but that cooling them with liquid nitrogen did not make any further improvement detectable in the optical measurements.

The tubing used was of the widest possible bore consistent with ease of fabrication, all the tubing runs in the bench being kept as short as possible. To facilitate modifications in design all major connections employed commercial 1/2 inch vacuum couplings (Edwards). By use of a small mercury diffusion pump provision was made to evacuate the entire control bench, including the pressure regulators fitted to the gas cylinders (Matheson Model 19, stainless steel diaphram).

The regulators were set to provide a supply pressure of 10 lb/in^2 to three constant flow regulators fitted with 'floating ball' type meters (G A Platon) which were calibrated 0-20 l/min helium, 0-1 l/min neon and 0-20 l/min argon. Although not calibrated for use at this supply pressure the meters enabled particular mass flow rates to be reproduced. Gases were fed from the flow meters

via small bore toggle valves to a manifold and then through the molecular sieve. To ensure efficient operation of the molecular sieve and the flow regulators the pressure in this section was maintained at about 1 atmosphere by adjustment of a needle valve (Edwards type LB2) with a 1/2 inch by-pass line. This pressure was monitored with a differential diaphram gauge.

In general it was found necessary to alter both the needle valve setting and the constant flow control in order to vary the flow over the entire experimental range. Particularly careful adjustments were necessary when mixing gases.

2-5 THE PRIMARY DISCHARGE

The primary discharge, which generated the plasma whose decay formed the afterglow observed in the flow tube, was generated by power from a magnetron microwave generator operating at 2.45 GHz. A simple and effective microwave termination has been described by Fehsenfeld, Evenson and Broida[2] which couples microwave power into a plasma with great efficiency over a wide range of discharge region geometries and gas flow conditions. A termination of this type was made and fitted at the neck of a silica tube (the nozzle) which formed the transition from the narrow bore (1/2 inch i.d.) flow tubing of the gas control bench to the wide bore (4 inch i.d.) flow tube. (See Figure P4). This arrangement took advantage of the desirable electrical characteristics of the gas in the narrow bore tubing, in which a high degree of ionisation could be developed more efficiently than at the lower gas pressure in the wider bore flow tube.

Two models of this nozzle were made. The first had an open throat (Figure 2.3a) while the second, which gave a significantly higher afterglow ion density, had a restriction in its throat (Figure 2.3b). Both nozzles gave rise to the 'jet'-like flow at high pressures described in Chapter 3.

Microwave power for the discharge was generated by a magnetron oscillator (Raytheon type RK 5609A) capable of delivering up to 60 watts of microwave power.

Modulation from fully on to fully off could be achieved by swinging the magnetron anode voltage by about 150V peak to peak. A circuit was developed which modulated the earth rail of the smoothing circuit in the magnetron power supply (Figure 2.4). With an input signal of -10V derived from a pulse generator it was possible to vary the microwave discharge pulse from 0.5 ms to 15 ms with a repetition rate of up to 1 KHz. However, the microwave discharge would not strike reliably without some source of pre-ionisation.

A unit was developed which delivered a high voltage pulse (10KV) of duration of order 0.2 ms at the start of the modulation pulse. The circuit is shown in Figure 2.5. When applied to a foil wrapped round the silica nozzle upstream of the microwave termination this pulse initiated a discharge reliably under all conditions of gas flow and repetition rates.

2-6 R. F. REHEATING

In order to discriminate between light from ions originating from charge transfer reactions and Penning reactions, it was found, as described in Chapter 3, that without affecting the metastable density the ion density in the afterglow could be reduced by more than two orders of magnitude by reheating the plasma. Preheating was performed most conveniently by application of r.f. power to the afterglow just downstream of the primary discharge.

The most satisfactory frequency and electrode configurations were found by trial and error. A 100 watt r.f. transmitter (Heathkit DX-100U) operating at 20 MHz was coupled to the afterglow via an L-C 'tank' circuit. The two electrodes were the steel flange supporting the silica nozzle, which was in direct contact with the plasma, and a 2 inch copper band wrapped around the 6 inch spacer tube externally, a few cms downstream of the steel flange.

The transmitter was keyed on by the gating circuit of a time-delay

oscilliscope (Tektronix type 545A) which enabled the reheat pulse to be varied in length and to occur at any time after the initiation of the microwave pulse.

2-7 THE REACTION REGION

The reactions under study took place in the reaction region 45 cm downstream of the primary discharge. Access to the region for changing the metal under study was gained through the side arms of a cross piece forming part of the flow tube. The lay-out of the reaction region is illustrated in Figure P5.

The metal under examination was evaporated from a tungsten boat of the type used in vacuum coating apparatus. The boat was clamped at each end in slots cut in two 1/2 inch diameter copper rods, which in turn were clamped into water-cooled, high current vacuum lead-ins of 600 amps capacity. The copper rods also provided support for the electron density probes which are described in Chapter 3.

The two high current lead-ins, together with two measurement current lead-in assemblies and a Pirani vacuum gauge head, were mounted radially on a collar which extended from one side arm of the cross-piece. This arrangement permitted largely uninterrupted observation of the entire reaction region through a 7 inch diameter glass window. To permit measurement of ultra-violet radiation the glass window was replaced by a window, 2" x 6", in optical quality silica (Spectrosil grade B) mounted on an aluminium plate.

A similar collar on the opposite arm of the cross-piece provided a short 2 inch i.d. pump line for the oil diffusion pump mentioned in Section 2-3. A second window of glass or silica was mounted in the same way on this collar.

The inter-connection of all the equipment described in paragraph 3 is shown in Figure 3-1.

2-8 THE OPTICAL DETECTION SYSTEM

Light from the reaction region passed through the silica window on the cross-piece, through a silica lens (f5, 10 cm focul length), through a monochromator and finally onto the photo cathode of a photomultiplier. The current from the photomultiplier was measured with a d.c. amplifier. Each of these components is part of the optical detection system which was calibrated for relative spectral response as a whole.

The monochromator was designed by Dr C E Webb and employed a Czerny-Turner mounting. The grating (Baush and Lomb) was ruled with 1,200 lines/mm over an area 2" x 3" and blazed at 7,500Å in first order. The instrument had an aperture of f10, a dispersion in first order of 10Å/mm and, by reducing the height of the slits, was capable of resolving completely lines of separation 0.5Å.

Multiple diffraction effects, which are common to instruments of this type[3], gave rise to spurious transmission peaks in the range 2,500Å to 3,000Å. These were suppressed successfully by masking a small area of one of the mirrors.

The grating mount was rotated by a sine-bar drive which was adjusted so that the wavelength could be read directly from a counter to an accuracy of ±1Å in the range 2,000Å to 10,000Å. The usefulness of this instrument lay chiefly in its great light gathering power, due to the high dispersion which allowed the use of wide slit settings.

2-9 THE PHOTOMULTIPLIERS

Two photomultipliers were employed. The first (EMI type 9656), used for measuring light in the range 2,000Å to 6,000Å, had an S13 cathode and silica window. The second (RCA 7102), used for measuring light in the range 5,000Å to 10,000Å had an S1 photo-cathode.

Both photomultipliers were cooled with dry ice and were housed in similar mounts, whose features are shown in Figure 2.6. Carbon dioxide, sublimated from the dry ice in the reservoir, is cooled by passing back down through the dry ice in two copper tubes and directed as two jets onto the surface of the photocathode. The entire photomultiplier is surrounded by dry carbon dioxide which constantly flows outwards through the monochromator exit slit, preventing air, which would cause condensation, from reaching the cold glass of the photomultiplier.

Two zener diodes were used in the dynode chain. The first, between the cathode and the first dynode, ensured low noise when operating the photomultiplier at low voltages. The second, between the last dynode and the anode, prevented non-linearity of response when high output currents were drawn[4]. Under no circumstances was a current greater than 1 mA ever drawn from the photomultipliers.

The photomultipliers were operated at one of five accurately reproduceable voltages, which were chosen to correspond to differences in gain of about a factor 20. The voltages were obtained by dividing the output from a highly stabilised high voltage supply (Isotope Developments type 532/D) with a high stability potentiometer unit. The relative response of the photomultipliers at the five voltages was calibrated to an accuracy of 1%.

The signal from the photomultipliers was measured with a d.c. current amplifier when intensity measurements were required. This instrument provided 9 switched ranges between 1 nA and 10 mA, with full back-off facilities, and was accurate to $\pm$2% over the entire range.

2-10 CALIBRATION OF THE OPTICAL SYSTEM

In order to measure the relative photon rates of transitions observed in the reaction region, a calibration was required which would yield the spectral response of the entire optical system. The calibration was performed by measuring the response of the system to lamps of known spectral output.

2-10.1 Standard lamps

The three lamps used for the calibration were single coiled coil tungsten-bromine lamps, rated at 420W, 120V (Thom type A1/227).

The d.c. currents required to operate the lamps at a colour temperature of 3150K were calibrated at the National Physical Laboratory and specified in terms of the voltage developed by them across a standard resistor. These currents were reproduced in the laboratory by measuring the voltage developed across the same standard resistor against the voltage of a standard Weston cell by use of a potentiometer.

Commercial lamp holders suffer from variable contact resistance. In the design of the stirrup-type lamp mounts shown in Figure P6 the gold plated tips of two copper rods, which supported the lamp and provided electrical continuity to the terminals, were pressed against the lamp contacts by the sprung side of the mount. This arrangement ensured good long-term stability.

2-10.2 Calibration Procedure

The lamps were set up on the side of the cross piece opposite to the monochromator so that light from them travelled through the entire optical system by the same path as light from the reaction region. It was possible that the distribution of light from the lamps was not the same as a fully diffuse source. A relative response factor was all that was required, not an absolute sensitivity, so that rather than attempting to diffuse the light, which would add the further complication of the spectral response of an additional element in the system, the light from the lamps was imaged directly on the monochromator slits. The exact positions of each lamp could not be reproduced exactly, so the final close agreement between the three calibrations confirmed that any assumption about imaging was not critical.

An attempt was made to calibrate the relative sensitivity of the monochromator in second and third order. However, the results were not reproduceable due to small instabilities and drifts in the spectral sources used to compare the first with second and third order

response. The calibration was therefore made directly in the first order. During the calibration light from higher orders was eliminated by use of a soda glass filter and an orange filter (Chance - Pilkington OY2).

The filter transmission factors were established to be constant over their range of use and their values determined to better than 1%.

2-10.3 Spectral Response

To derive the spectral response of the monochromator to line radiation from the calibration data, obtained from a continuum lamp spectrum, knowledge of three wavelength dependent quantities is required.

i The power per unit band width emitted by a black body at the lamp colour temperature

ii Emissivity of tungsten, absorption of bromine and other modifications to i) due to the particular features of the tungsten-bromine lamps

iii The small change in dispersion of the monochromator at different angular positions of the grating.

A table of the relative spectral radiant intensity from 3,000Å to 8,000Å for a tungsten-bromine lamp at a colour temperature of 3,150K was made available to us by Dr J R Moore of the National Physical Laboratory. The table was an estimate based on a compilation of data from a large number of tungsten-bromine lamps of similar construction to the ones used and disposed of factors i) and ii) together. Factor iii) represented only a small correction (less than 4%) for the particular monochromator in use, but allowance for it was made in the computations.

The responses from three lamps were averaged and for each photo-multiplier the mean spectral response was plotted, using an arbitary scale which indicated the relative current observed for a constant photon rate per unit band width originating from inside the reaction region. The scatter between readings from the three lamps at each wavelength setting was small and indicated an accuracy for the final calibration curves of about 3%. This was the most satisfactory agreement for measurements of this kind.

Three months after the initial calibration, and after the measurements on the afterglows, another calibration was made using only one of the lamps. The result fitted the earlier calibration to within ±6% over the entire range of calibration, indicating there had been no significant change in the spectral response of the optical system.

REFERENCES

1 Dushman, S, "Scientific Foundations of Vacuum Technique", New York: Wiley (1962)

2 Fehsenfeld, F.C., Evenson, K.M. and Broida, H.P., Rev.Sci. Instr. 36, 294 (1965)

3 Mitteldorf, J.J., and Landon, D.O., Appl. Optics. 7, 1431 (1968)

4 Engstrom, R.W. and Fisher, E., Rev.Sci.Instr. 28, 525 (1957)

TABLE 2.1

Typical analysis of gases

Contaminant	Content, v.p.m.		
	Helium	Neon	Argon
Argon	1	-	(99.995%)
Carbon dioxide	1	-	1
Helium	(99.995%)	(30%)	-
Hydrogen	1	2	1
Methane	1	-	-
Neon	14	(70%)	-
Nitrogen	14	50	20
Oxygen	1	-	6
Water	12	5	5

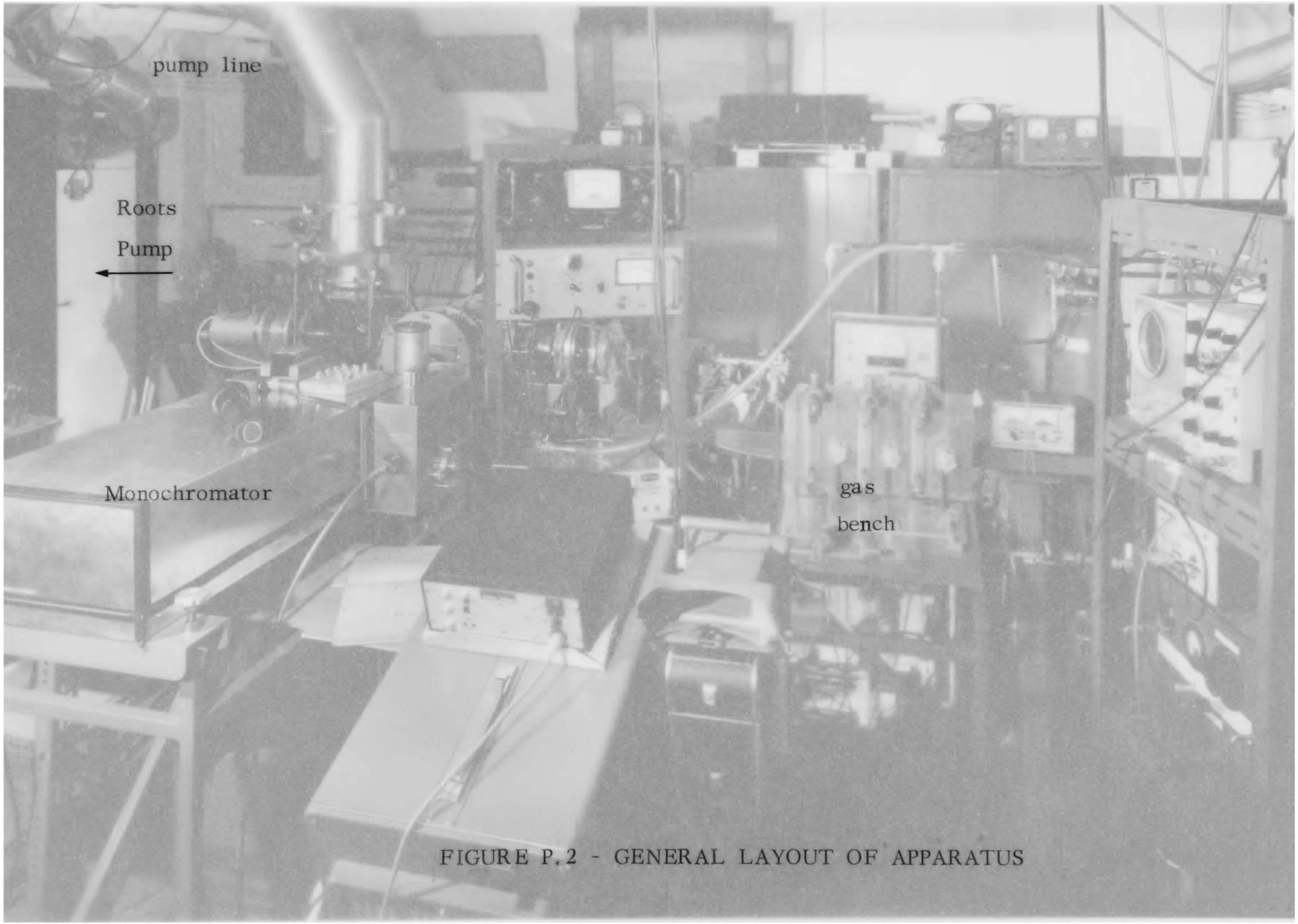

FIGURE P.2 - GENERAL LAYOUT OF APPARATUS

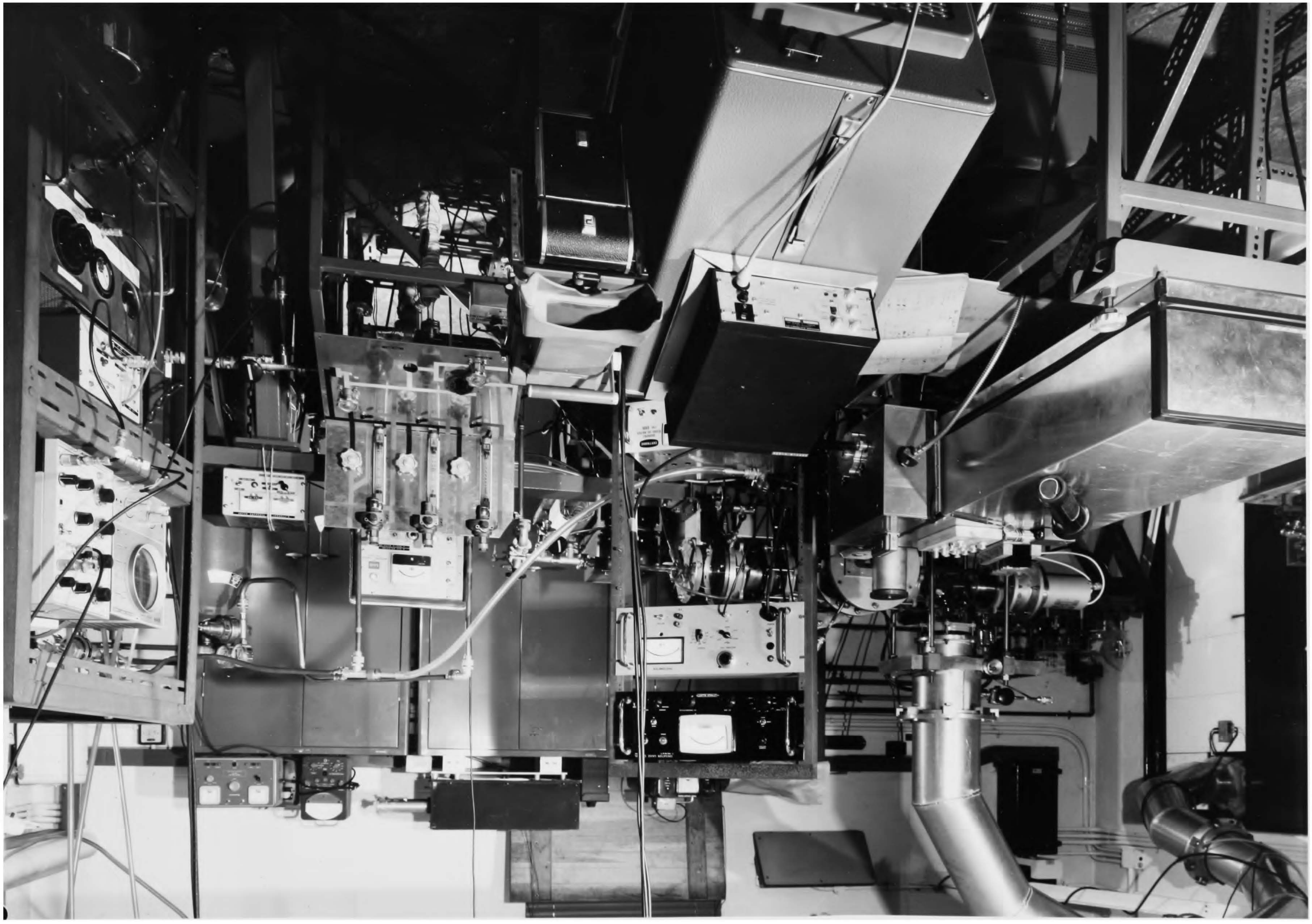

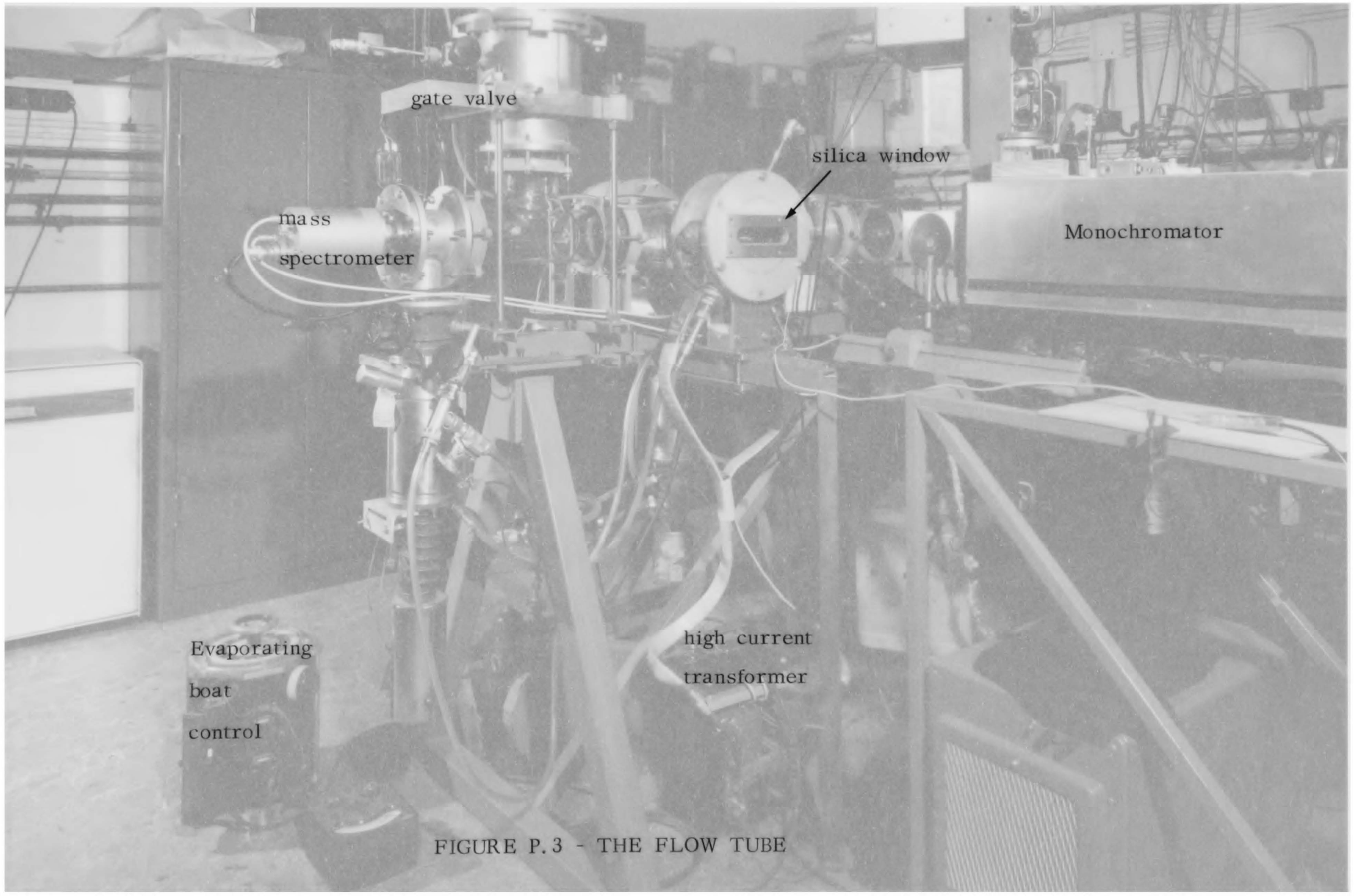

FIGURE P.3 - THE FLOW TUBE

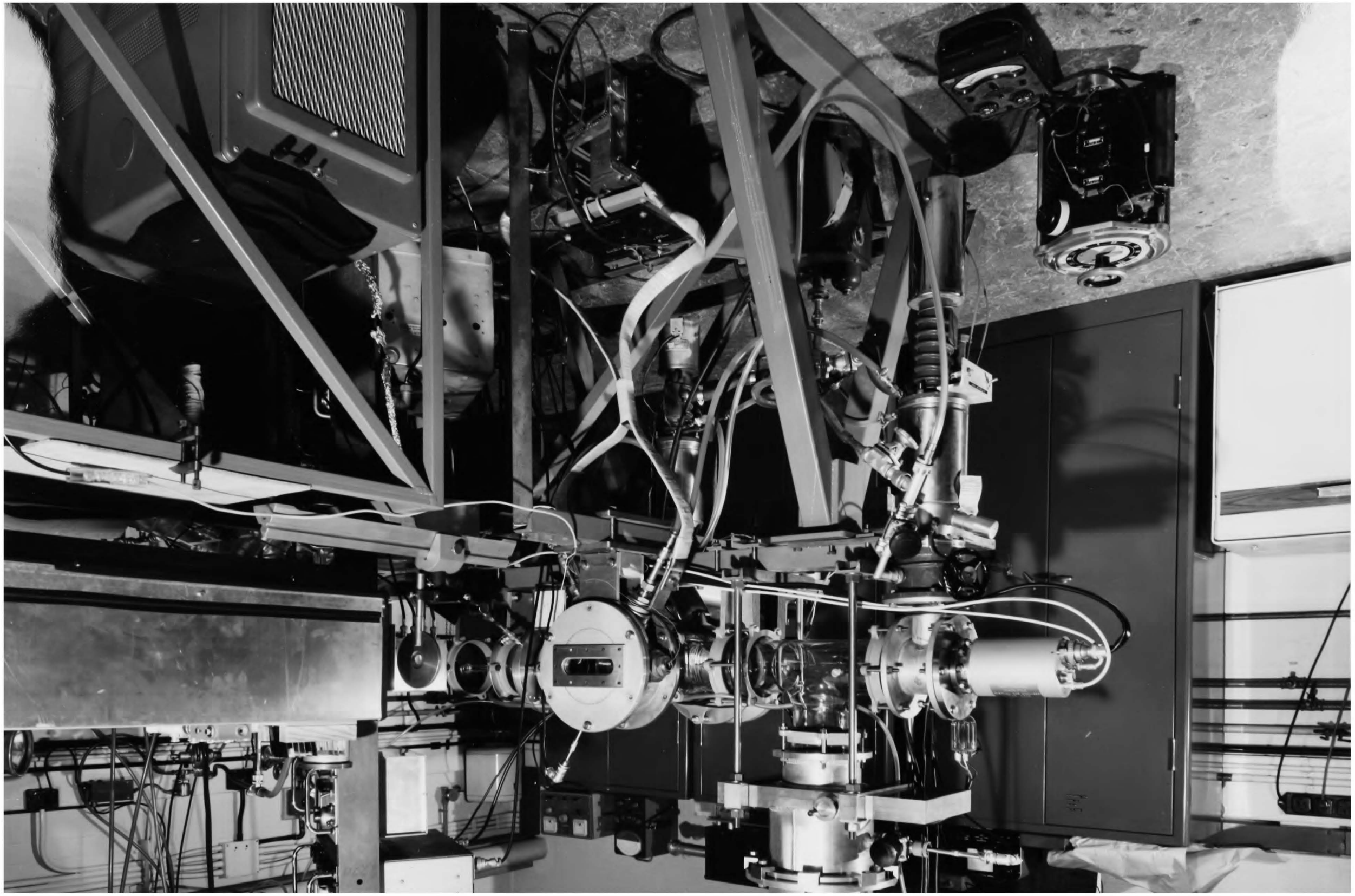

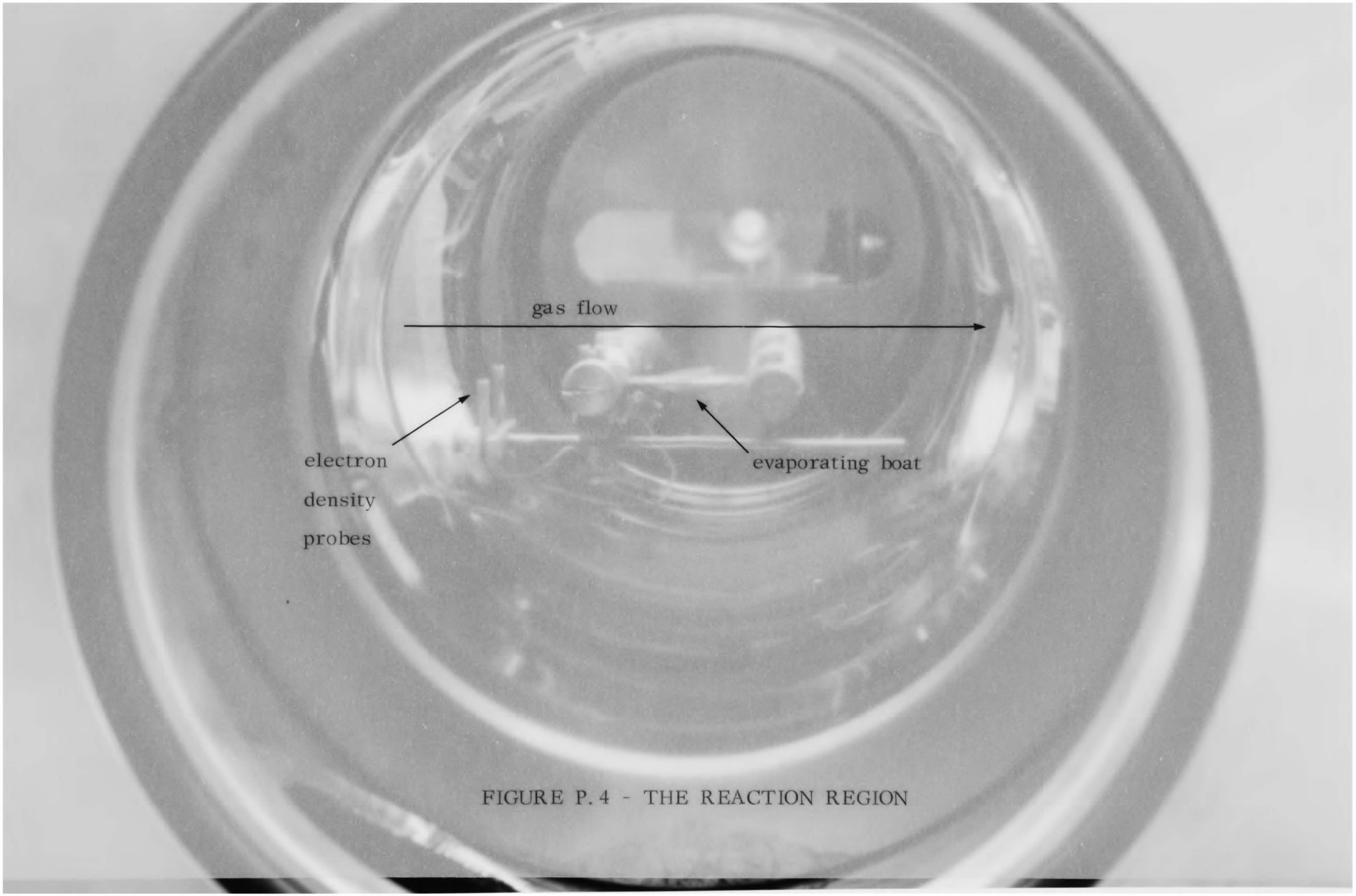

FIGURE P.4 - THE REACTION REGION



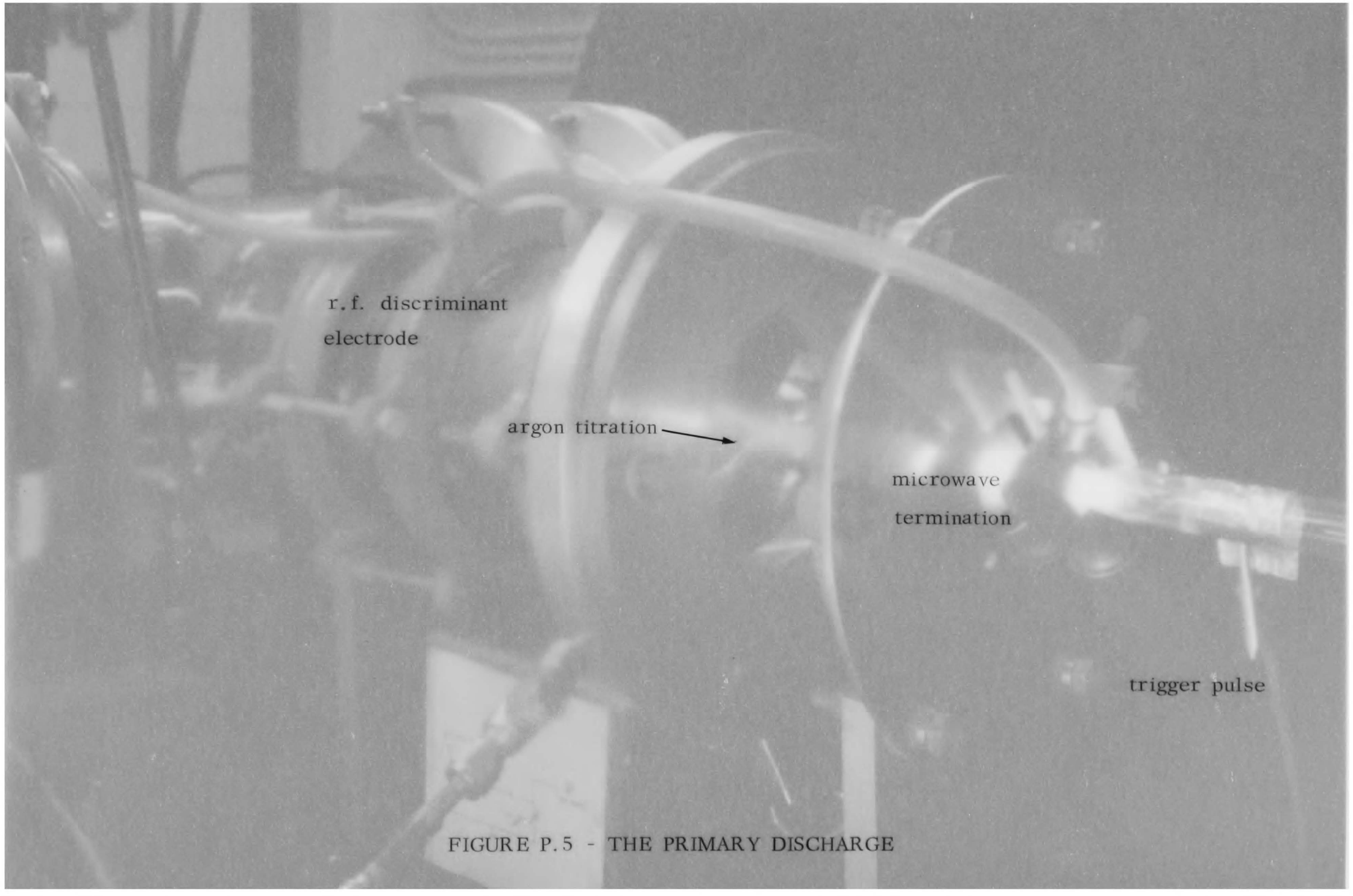

FIGURE P.5 - THE PRIMARY DISCHARGE

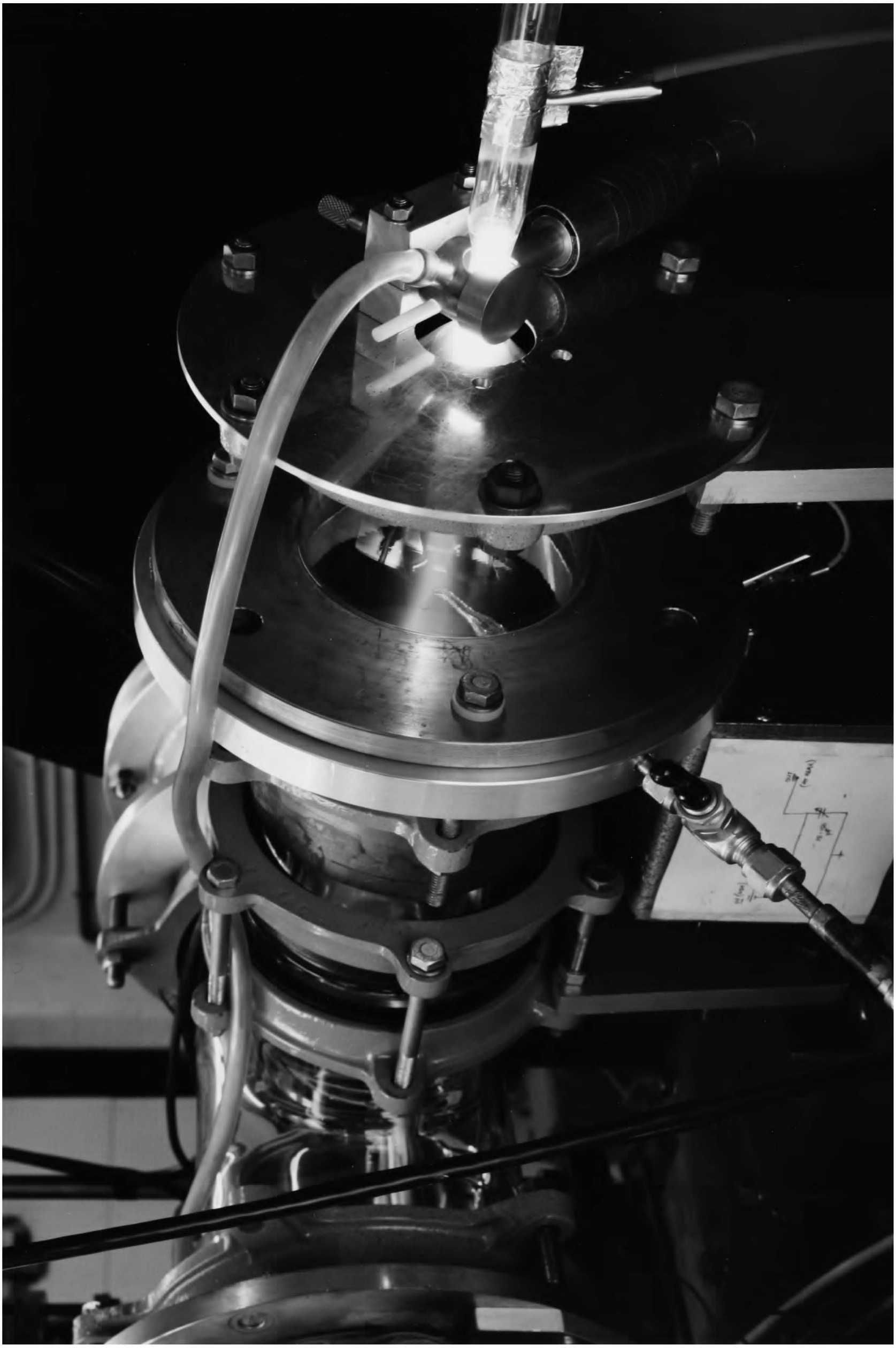

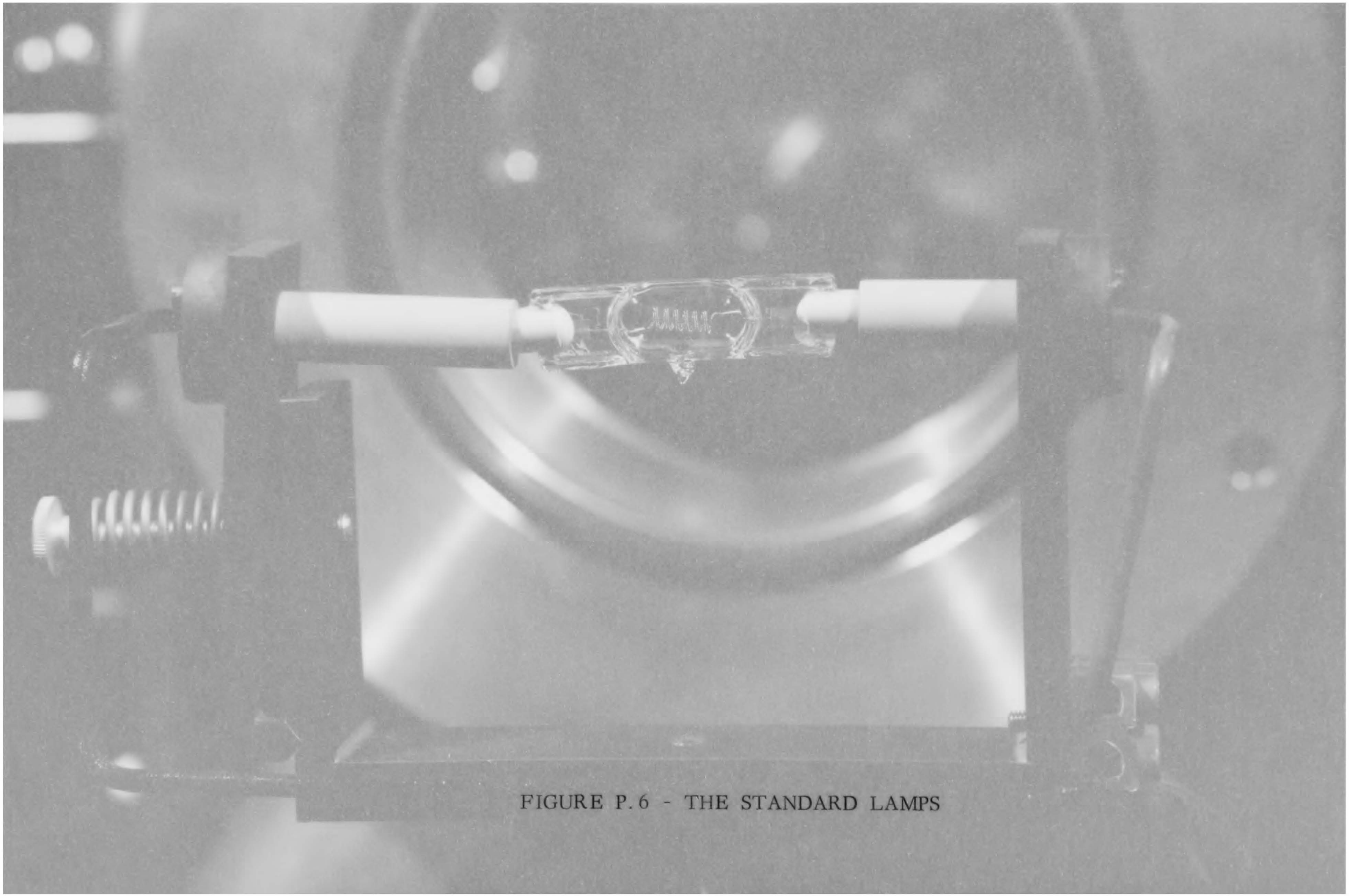

FIGURE P.6 - THE STANDARD LAMPS



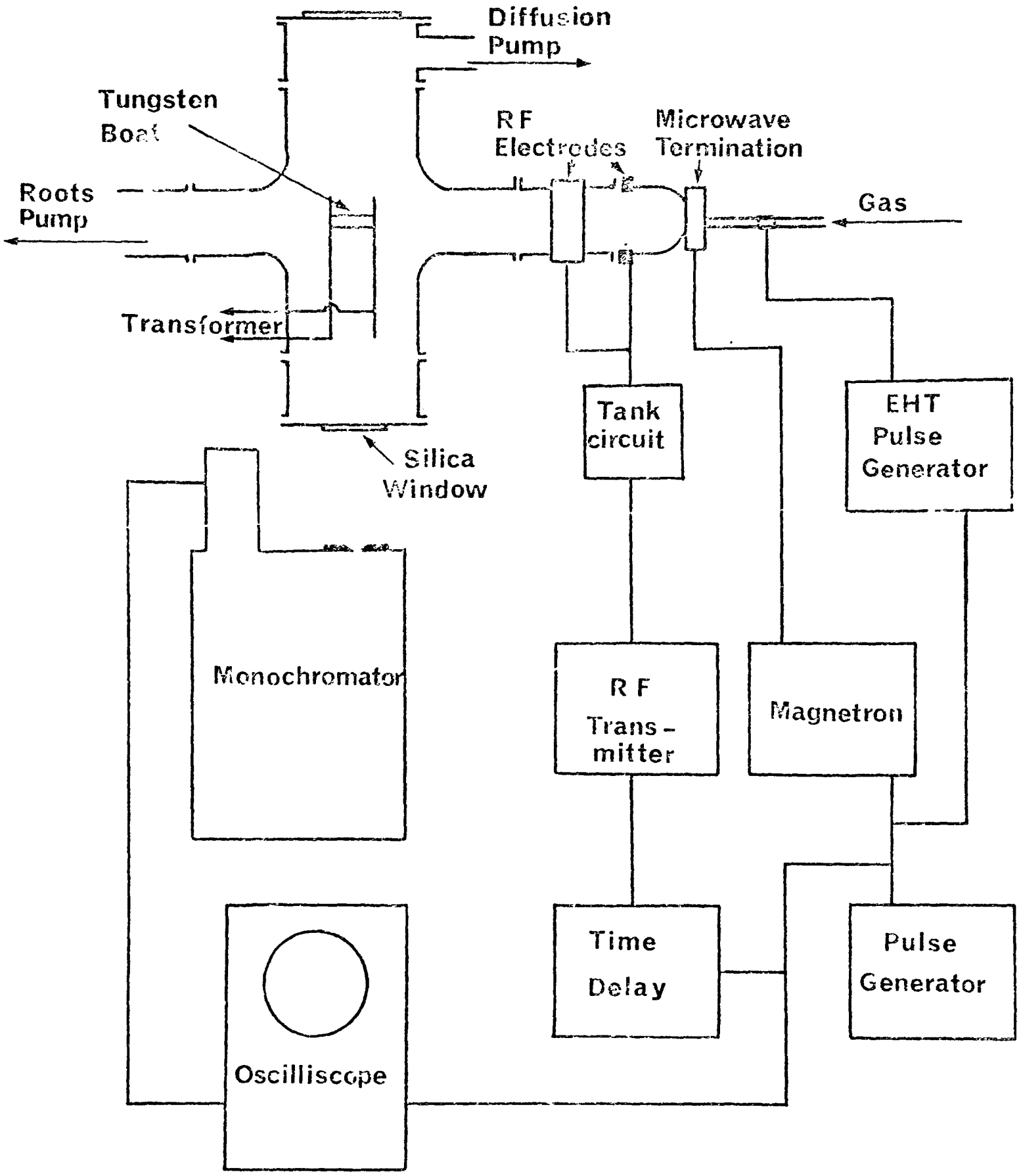

Figure 2.1 - Schematic diagram of apparatus

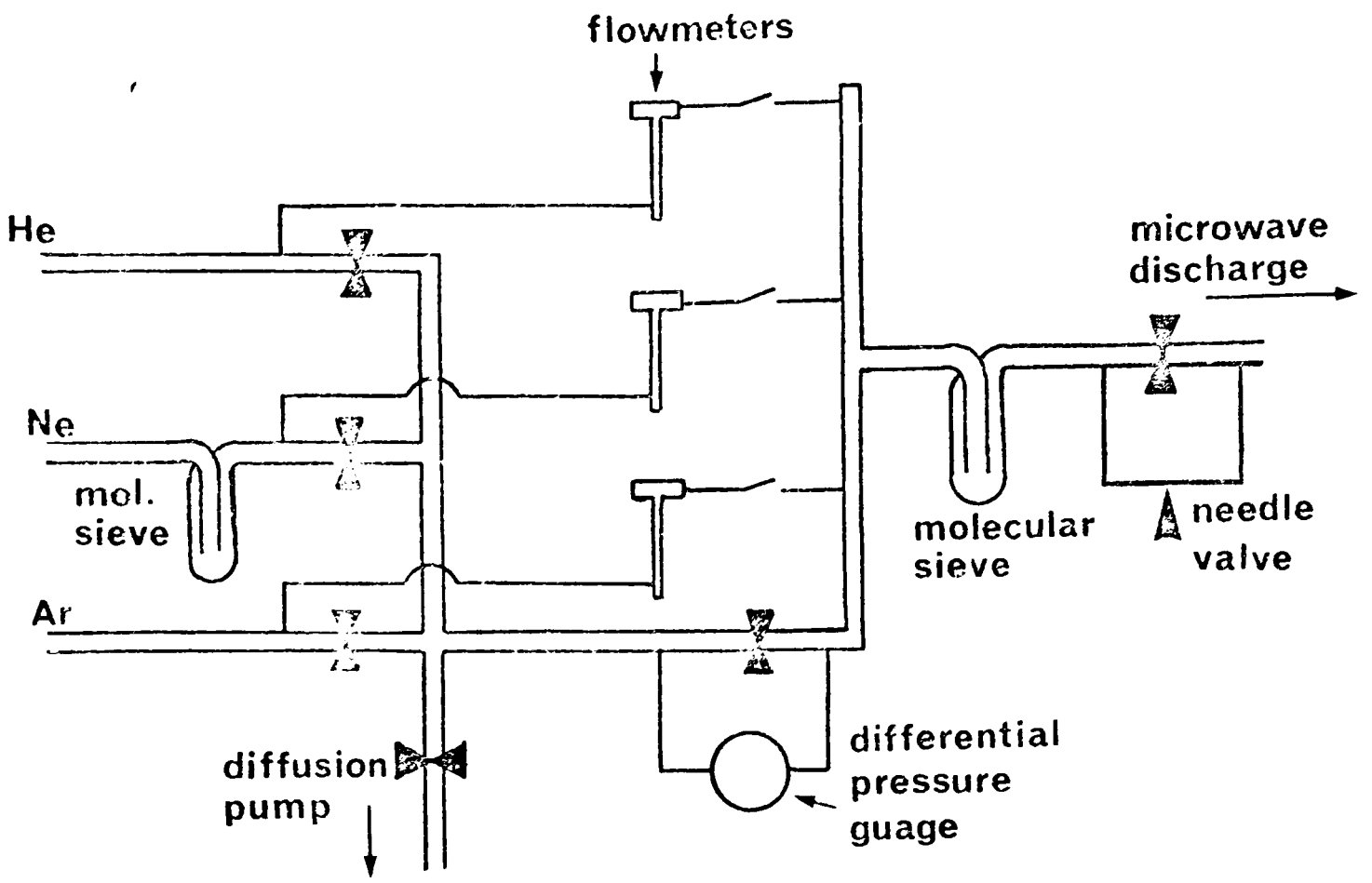

Figure 2.2 - Gas Control Bench

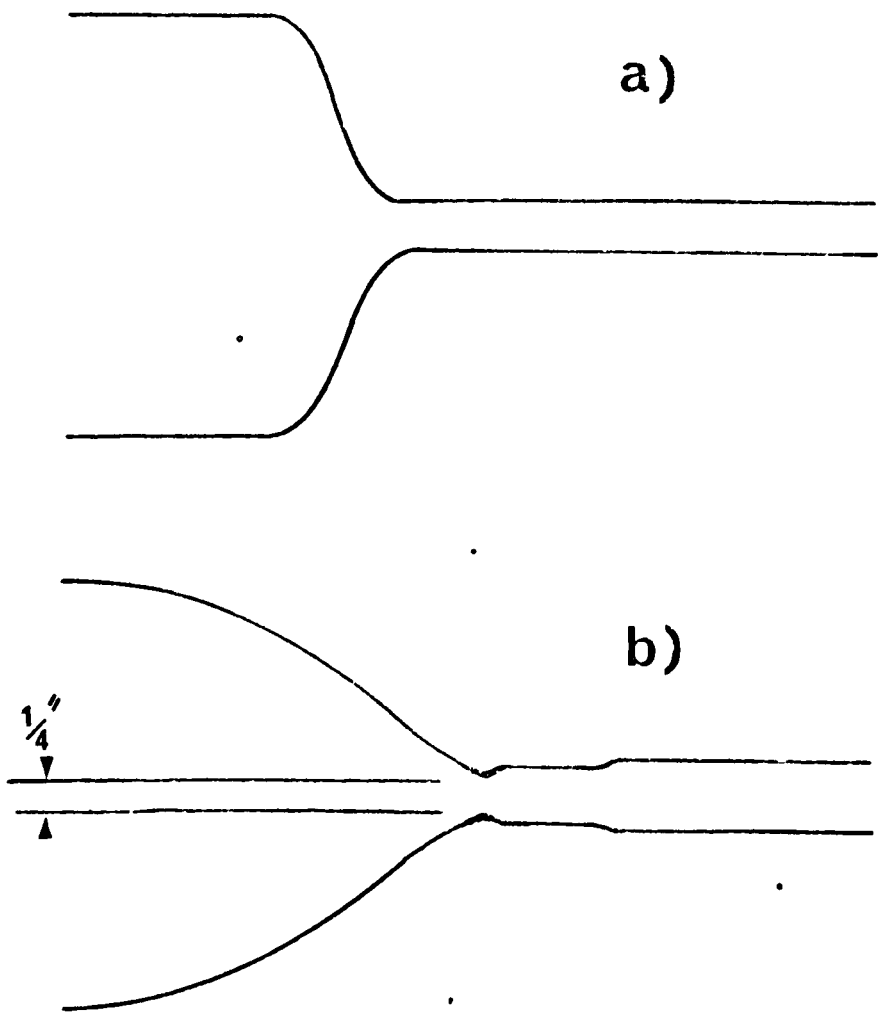

Figure 2.3 - Silica Nozzles
Scale 1:2.54

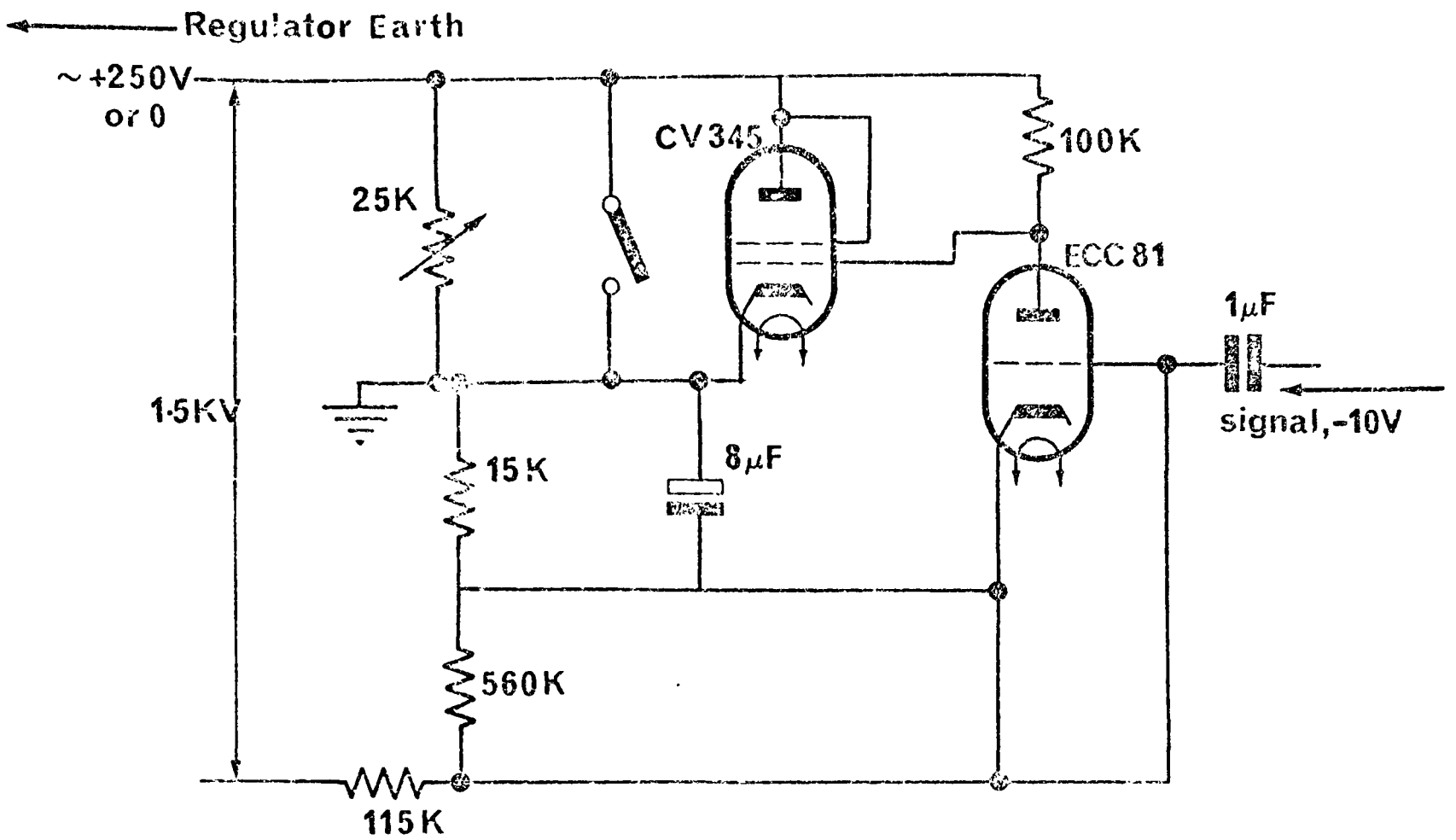

Figure 2.4 - Magnetron modulator

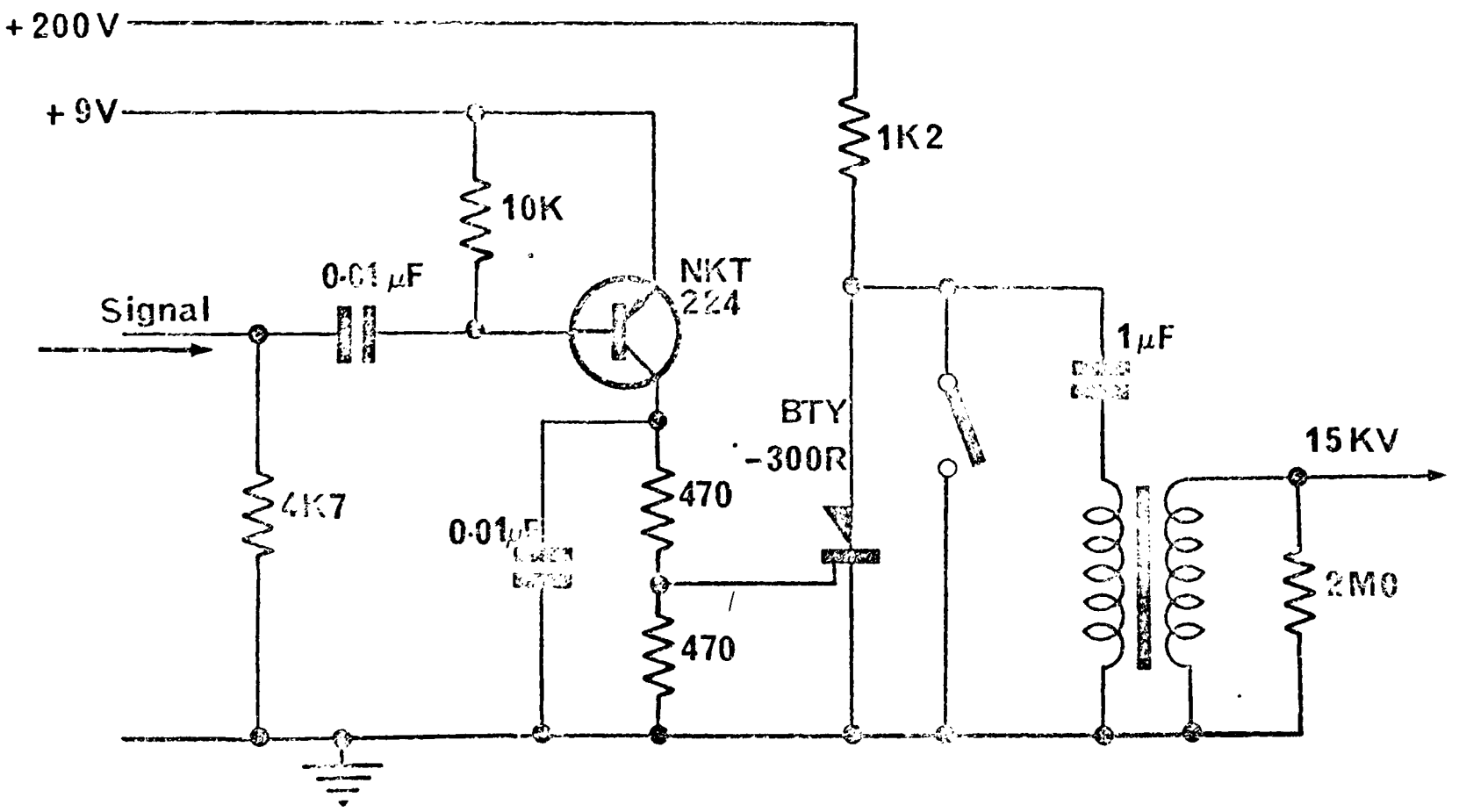

Figure 2.5 - EHT pulser

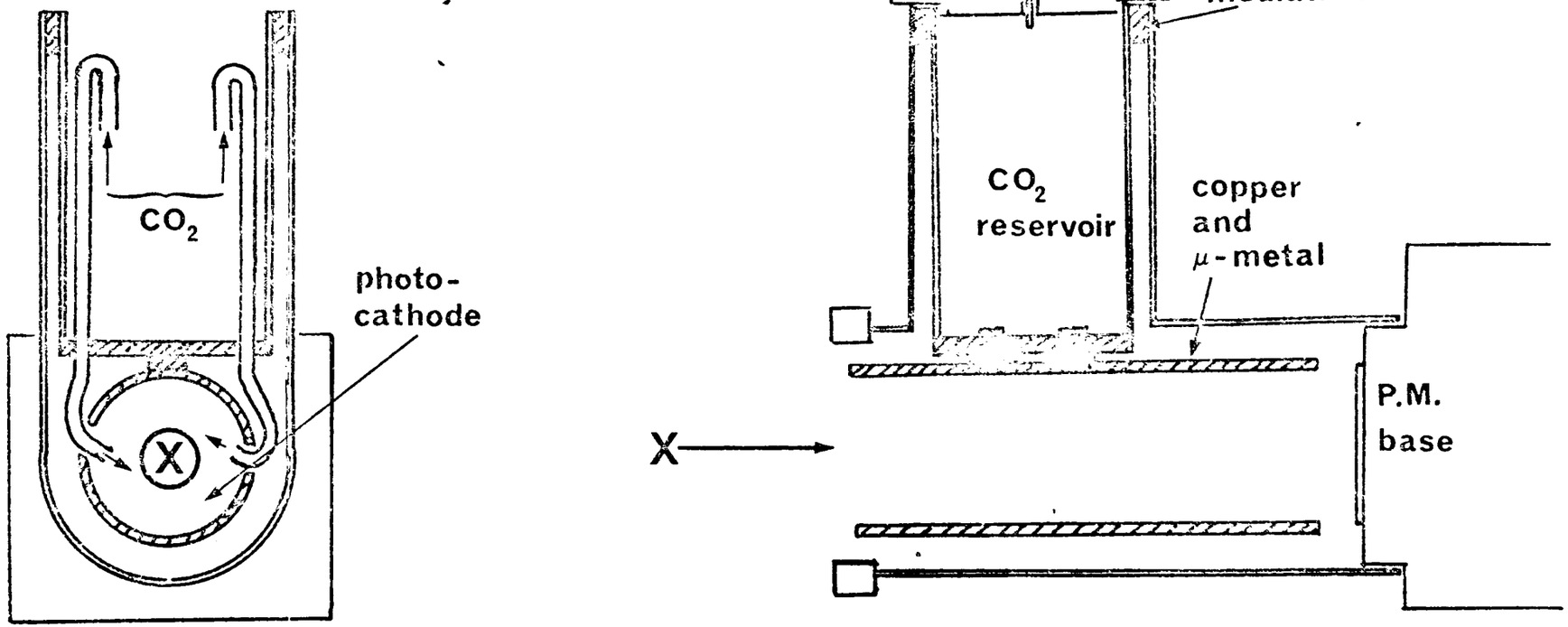

Figure 2.6 - Photomultiplier Mounts

CHAPTER 3

PRELIMINARY EXPERIMENTS

' While man's desires and aspirations stir,
He cannot choose but err. '

Goethe

CHAPTER 3

PRELIMINARY EXPERIMENTS

In this chapter the performance of the apparatus and its initial testing is described. The results of the preliminary experiments are presented and their significance discussed.

3-1 THE FLOWING AFTERGLOW

Under typical operating conditions, with helium as the flow gas, the diffuse blue glow of helium recombination radiation[1] extended along the flow tube from the intense white discharge, concentrated in the entrance nozzle, to a point well downstream of the reaction region. At normal pressures of operation the volume flow rate in the reaction region was typically 450 l/sec. On reducing the pump speed the afterglow contracted to the axis of the flow tube, growing brighter but not decreasing in length until the pressure in the flow tube approached about 2 torr (depending on the mass flow rate). Optical measurements confirmed that the glow consisted only of helium recombination radiation (He I lines and band spectra of He_2) and, at higher pressures, a weak spectrum of some neon lines. The observation of neon lines in the afterglow was considered to be an encouraging confirmation of the cleanliness of the afterglow for, as the abundance of neon in the gas was known to be small (~14 v.p.m., Table 2.1), inability to observe lines from other impurities (excited at least as strongly as neon due to their lower excitation potentials) indicated that they could be present only in insignificant quantities.

The time for the afterglow of the primary discharge to flow from its point of generation in the entrance nozzle to the reaction region was measured by observing emission from a slug of afterglow plasma in the reaction region, noting its delayed time of arrival

after generation by a short pulse of microwave power in the entrance nozzle. It was observed that decreasing the pump speed at a constant mass flow rate did not reduce the flow velocity in the 'jet' of plasma as expected. This effect is illustrated by Figure 3.1, in which the intensity of a transition excited by charge transfer (6102 Å, Zn II) is used to monitor the plasma density. The figure shows an oscilliscope traces of the plasma density against time measured at five different pumping speeds but with the same mass flow rate. By altering the mass flow rates, however, the flow velocity could be varied between 5 x 10^3 cm/sec (4 atmos l/min) to 3 x 10^4 cm/sec (15 atmos l/min).

The axial flow velocities calculated from the observed mass flow rate, pressure and flow tube diameter were considerably smaller than those indicated by the time delay measurement. However, the latter were in good agreement with velocities calculated from the mass flow rate, pressure and the apparent diameter of the jet plasma.

The jet-like behaviour of the gas flow is due to the high velocity of the gas flow, since at velocities of order Mach number 0.3 and higher (velocity of sound in helium is 9.7 x 10^4cm/sec) gases behave as incompressible fluids[2]. The jet is propelled at a speed determined by the nozzle and the mass flow rate alone, for the velocity in the nozzle is independent of the gas pressure in the flow tube.

Similar effects were observed when argon was substituted for helium. In argon, however, marked instability set in when the pressure in the flow tube exceeded 0.6 torr. Turbulent flow[2] must be expected when Reynold's number approaches 1000, which corresponds to a pressure of 1 torr at the observed flow speed and afterglow jet diameter.

Considerable enhancement of the axial ion density in all gases was made available by use of the jet-like flow condition, which was therefore adopted for all the intensity measurements. The enhancement is illustrated in Figure 3.2 which shows the ion density (measured as indicated in Section 3-3) plotted against pressure of helium at a number of mass flow rates.

The spectrum of the argon afterglow consisted entirely of Ar I lines. At a late stage in the experiments a differentially pumped mass spectrometer became available (20th Century Electronics, Centronic Q 806). It was not possible at the early stage in the development of this facility to make an analysis of the afterglow under typical flow conditions in either gas. An analysis of the plasma at the end of the flow tube, made at a high mass flow rate and pressure of argon, showed the afterglow at this point consisted of 70% Ar^+ with 22% mass 41 (HAr^+?), 1% Ar_2^+ and 7% other impurity ions (O^+, CO^+ etc).

3-2 PROBE MEASUREMENTS

In order to establish that the plasma electrons arriving at the reaction region had insufficient energy to cause direct collisional excitation of the reactant metal vapours, it was desirable to make at least some crude measurement of electron temperatures in the reaction region. In addition, in order to optimise the flow conditions it was desirable to have a means of monitoring the relative concentration of electrons in the reaction zone.

The most convenient method available for measurements in the range of plasma densities and temperature anticipated was the floating double probe technique due to Johnson & Malter[3]. Two probes are connected by a circuit whose potential is allowed to float with respect to ground, and the current flowing between the probes is measured as a function of the potential difference between them. The characteristic curve of current versus voltage is of the

general shape of that shown in Figure 3.3, which shows an experimental trace in a helium afterglow under the flow conditions used for intensity measurements. Since high precision values of the electron temperature were not required a simple form of data extraction was used which employed a geometrical construction to derive values of electron temperature and density. The procedure is described in Appendix 1, which extends the normal formulae to the case when the probe areas are unequal or the plasma non-uniform in density. Details of the construction of the probes and the circuit used to obtain the characteristics are given in Figure 3.4.

Similar to the findings of Clements and Skarsgard[4] it was found that unless particular care was taken to ensure cleanliness of the probes the characteristics displayed poor saturation and indicated artificially high electron temperatures. Before making readings, therefore, the probes were subjected to cleaning by ion bombardment for a few minutes by drawing a discharge current of 2mA from them. Reproduceability of the characteristics began to suffer after a period of five minutes when fresh cleaning was required.

Under the flow conditions typically used for intensity measurements the electron densities measured were of order 8×10^{10} cm^{-3} in helium and 2×10^{11} cm^{-3} in argon. The corresponding electron temperatures, which were entirely independent of flow conditions were 50mV and 250mV respectively. Expected departures of the probe traces from an ideal probe characteristic will tend to increase the apparent electron temperature, so that the temperatures quoted represent an upper limit rather than an absolute value.

It was observed that when the voltage applied between the probes was large the current was almost independent of voltage, i.e. the characteristic displayed good saturation. It was possible, therefore, to operate the probes in a region of heavy saturation so that under

all conditions the current between the probes (which depends only on the ion density at the negative probe) would provide a continuous measure of the relative ion density. As the pressure (pumping speed) was altered, the axial alignment of the jet of plasma changed (Section 3-3), so that the ion density at the probes could not be expected to bear an exactly linear relationship with the ion density in the region of evaporated metal. Under a particular set of experimental conditions, however, the jet changed position in a reproduceable manner, so that once its nature had been established a small degree of non-linearity was not of great significance.

3-3 INITIAL EXPERIMENTS WITH ZINC

The metal chosen as the subject of initial investigations was zinc. The choice was made because shortly before the apparatus was ready for testing a publication by Jensen et al[5] presented indirect evidence suggesting that thermal energy charge transfer was responsible for pumping certain Zn II transitions in the He - Zn laser.

Evaporation of zinc into a helium afterglow gave rise to an orange-red plume of excited zinc ions extending downstream from above the evaporating boat. The red colour, arising from the dominant visible emission lines in Zn II, was in contrast with the blue colour characteristic of neutral zinc in a zinc discharge lamp. This single visual observation confirmed that electron excitation, which in normal circumstances would give rise to a strong Zn I spectrum, was not the dominant mechanism in the reaction zone. Analysis of the spectrum established that light from the plume of zinc was entirely dominated by transitions in the Zn II spectrum, none of which had an upper level higher in energy than the ground state helium ion.

In the design stage the possibility of evaporated metal coating the windows of the reaction region had been a cause for some concern. However, it soon became apparent that this would not present a problem in practice. If metal was evaporated at a very high rate the plume of vapour extended upstream of the boat, destroying all the helium ions in a narrow region at the boundary of the metal vapour.

A lower rate of evaporation, using about 500 mgm zinc/hr., provided greatly improved long-term stability and an acceptable rate of metal coating. After evaporation at this rate for a period of two hours the amount of metal deposited on the windows was barely detectable, providing the pressure of helium in the flow tube had not been allowed to fall below 0.05 torr. Calibration of the optical system both with and without a typical thickness of metal deposited on the window confirmed that the relative spectral sensitivity of the optical system remained unaffected.

When the discharge was run in a pulsed mode, at lower pressures of operation in helium, certain initially puzzling features of the shape of the corresponding pulses of emission in ZnII became apparent. An oscilliscope trace of the intensity of the transition at 5894$\mathring{A}$ in Zn II is shown in Figure 3.5a. The intensity of the transition at 6102$\mathring{A}$ in Zn II, shown in Figure 3.5b, however, presents quite a different time dependence. All the lines in the Zn II spectrum were examined and it was found that each line displayed one of these two classes of behaviour, typified by Figure 3.5a or Figure 3.5b. It was noted further that all the lines belonging to the class typified by Figure 3.5a originated from levels energetically accessible to the helium $2\,^3S$ metastables, whereas the class typified by Figure 3.5b consisted of lines originating from levels higher than the helium $2\,^3S$ metastable, but below the helium ground state ion energy. A search was made for transitions from higher levels, but none were found. It is reasonable to conjecture that the difference in behaviour of the lines corresponds to a difference in the excitation mechanisms, and consequently reflects the difference in the time variation of the concentration of the species of particles responsible for their excitation. Specifically, Figure 3.5a represents the time behaviour of the density of helium $2\,^3S$ metastables and Figure 3.5b represents the time behaviour of the density of helium ground state ions.

The explanation of the sharp increase in ion density at the end of the afterglow pulse can be given in the following terms. The oscilliscope trace in Figure 3.5b represents a plot of the helium ion density. While the microwave power is on, a small amount of power may penetrate downstream from the primary discharge into the flowing afterglow, where it reheats the electrons. The dominant loss mechanism for helium ions (Section 1-3) is governed by ambipolar diffusion, the coefficient of which is related to the electron temperature by[6]

$$D_a = D_o \left(1 + \frac{T_e}{T_i}\right)$$

in which D_a and D_o are the ambipolar and normal diffusion coefficients and T_e and T_i are the electron and ion temperatures respectively. The effect of reheating the electrons in the afterglow plasma is thus to enhance the rate of loss of ions to the walls by ambipolar diffusion by decreasing the characteristic diffusion time (Section 1-3). At the same time the metastable density would remain unaffected. The sharp peak at the end of the ion density pulse represents the arrival of plasma which left the discharge momentarily before the microwave power was shut off, and which in consequence was not reheated.

In order to verify this explanation a d.c. excitation source substituted for the microwave entrance nozzle would eliminate plasma reheating due to feed down of power into the afterglow. A variable geometry hollow cathode device was built and in operation no reheating effect was observed. However, the device proved unsatisfactory for general use as it required careful adjustment for each flow condition and was unstable over periods of operation longer than one minute.

For all subsequent experiments a silica nozzle with a microwave discharge excitation was employed. No plasma reheating effect was observed following pulsed microwave excitation of argon. Neither did reheating occur at higher pressures in helium when operating with the jet-like flow adopted as the normal mode of excitation when making intensity measurements. Of the two designs of silica nozzle, that shown in Figure 2.3b provided an enhanced jet effect and in

consequence a higher ion density in the afterglow. A specific disadvantage of using the jet-like flow for experimental observations was the tendency of evaporated metal to creep upstream in the gas eddying between the jet and the flow tube walls, creating a very weak halo of metal ion light around the jet. The only way in which this could have been detrimental to the experiments was by introducing metal vapour to the afterglow before the electrons had had time to thermalise. No evidence for electron excitation was observed under any condition, however, and the effect could in any case be minimised by a suitable choice of flow conditions. Another undesirable feature was that, as a result of very small asymmetries in the shape of the nozzle, the jet of plasma changed its alignment to the axis of the flow tube as the pumping speed was reduced.

3-4 PENNING REACTIONS

The probe measurements described in Section 3-2 indicate that the plasma electrons reaching the reaction zone were indeed insufficiently energetic to cause appreciable optical excitation. In the case of a helium afterglow the particles with sufficient energy to excite metal ions, and which would not have decayed to states of lower energy during the journey of 2 ms from the discharge, are, in order of decreasing energy, helium ground state ions, helium metastables (2^1S and 2^3S), helium molecular ions (He_2^+) and helium molecular metastables, He_2^*. Of these only the helium ground state ion and the helium 2^3S metastables are likely to be present in any quantity as the reaction rates for formation of He_2^+ and He_2^* and the lifetime against conversion of $He(2^1S_1)$ to $He(2^3S_1)$ are small[7]. This conclusion was confirmed by the optical data.

Metastables of helium were detected by measuring the absorption of the appropriate lines from a hollow cathode lamp as they traversed the reaction region. Self absorption of these lines within the lamp itself would reduce the fractional absorption by metastables in the reaction region and lead to erroneous values for the metastable density. The degree of self absorption was checked by measuring the absorption in a second identical lamp placed in series with the first. Self absorption was small in the case of helium ($\sim$1%)*.

Under the same flow conditions used to obtain the results for zinc and cadmium presented in Section 3-6 an absorption of 15% was measured in the 3889Å line in helium. This indicated a metastable density of order 10^{11} cm^{-3} in the plasma jet (7 cm in diameter).

No absorption ($<$1%) of 5016Å was detected, which confirmed that He 2^1S_1 metastables did not survive the journey from the primary discharge in appreciable quantities (density $< 5 \times 10^8$ cm^{-3}).

3-5 CHARGE TRANSFER/PENNING REACTION DISCRIMINANTS

A discriminant was required to distinguish between optical excitation as a result of the two possible reactions remaining: charge transfer from He^+ and Penning ionisation by $He(2^3S_1)$. Reheating of the afterglow by feed-down of microwave power, described in Section 3-3, performed as a discriminant by removing ions but not metastables from the afterglow. However, it was desirable to operate the discriminant over a wide range of pressures and, in particular, under the flow conditions used for the intensity measurements.

It was found that by use of a separate source of r.f. power sufficient energy could be coupled directly to the electrons in the early afterglow plasma (Section 2-6) to remove the ions almost completely[8], without also causing optical excitation of metal ions in the reaction region.

---

* However, when neon and argon were substituted in the same lamps in order to measure the metastable densities in neon or argon afterglows, large self absorption ($\sim$30%) was detected. Although absolute densities could not be inferred, therefore, it was still possible to make relative measurements of neon and argon metastable densities.

Operation of the r.f. discriminant is illustrated in Figure 3.6, which shows oscilliscope traces of transitions resulting from the various reactions observed in a pulsed helium afterglow with cadmium evaporated. Each reaction can be identified by its own distinctive time behaviour and response to the r.f. pulse. Figure 3.6A. shows the effect of an extended r.f. pulse on the transition at 3250Å, originating from a Penning reaction, demonstrating that the pulse neither destroys nor generates metastables. The other oscilliscope traces are self-explanatory. All the traces shown in Figure 3.6 were photographed under the same flow and r.f. conditions and within a few minutes of each other.

The interpretation of the mechanism of the discriminant (Section 3-3) was verified by removal of the 6" section of flow tube between the entrance nozzle and the T piece (Section 2-3). With this arrangement complete discriminant action was not possible because the ions had insufficient time to diffuse to the walls of the flow tube (Sections 1-3 and 3-3).

Under conditions when the afterglow extended fully to the walls of the flow tube (high pumping speed) application of sufficient r.f. power to remove the ions did not affect the metastable density. Under jet-like flow conditions, however, a greater power was necessary to remove the ions and under these circumstances the metastable density was enhanced during the r.f. pulse. The discriminant action thus remained quite unambiguous under all flow conditions.

In order to confirm the interpretation of the discriminant action and in particular to verify that the pressure-dependent behaviour of some lines (Section 3-7) did not involve interactions with metastables, a further discriminant was required which would destroy metastables but leave ions unaffected. The cross-section for destruction of helium metastables by argon in a Penning reaction is about $7 Å^2$, while the cross-section for destruction of helium ions[9] is $< 10^{-2} Å^2$. As

a consequence of the large differential reaction rates the introduction of a small flow of argon into the afterglow would be expected preferentially to destroy helium metastables. In practice the greatest differential effect was obtained by introducing argon through a glass tube 10 cms downstream from the primary discharge (see Figure P4) and adjusting the flow until the helium ion density was reduced by a factor 2. Under this condition the intensity of lines originating from levels excited by Penning reactions was reduced by a factor 10. The classification of the mechanisms for excitation of the observed transitions into Penning ionization and charge transfer by this method agreed in every case with the r.f. discriminant data.

3-6 PRELIMINARY RESULTS, ZINC AND CADMIUM

It would appear from the calculated values of excited state lifetimes (Section 4-2) that the assumption is well justified that the dominant loss rate from excited levels is either radiative decay or collisional deactivation, rather than bulk transport from the experimental volume by the gas flow. The photon production rate for all transitions from a given upper level, fed directly by collisional excitation rather than by cascade, will thus be directly proportional to the reaction rate and, under a given set of experimental conditions, the cross-section for the particular process.

The preliminary results were published[10] in a letter to the Journal of Physics, B. and are summarised in Figures 3.7 and 3.8, in which the photon emission rate derived from the observed line intensities is indicated on a crude logarithmic scale by the width of an arrow connecting initial and final levels on a term diagram. Only the strongest lines are shown. This form of graphic presentation shows most clearly the dominant paths for cascade between excited states.

Several significant conclusions emerged from this study. Firstly, since the concentration of metastables was at least equal to the concentration of ground state ions it would appear from the observed relative excitation rates shown in Figure 3.7 that the charge transfer excitation cross-section is comparable to the Penning cross-section

in the case of zinc. This conclusion has been confirmed by the measurements of Collins[11] who estimates a total charge transfer cross-section for zinc of 21$\mathring{A}^2$. It would appear therefore that cross-sections for charge transfer leading to excited states are indeed sufficiently large to provide the pumping rates required for laser action.

Secondly, the c.w. laser transitions in Cd II at 3250$\mathring{A}$ and 4416$\mathring{A}$ and in Zn II at 7479$\mathring{A}$ and 5894$\mathring{A}$ are pumped by Penning reactions of the ground state atom with He 2^3S_1, metastables populating the upper level directly. The pulsed laser transitions in Zn II at 7758$\mathring{A}$, 7613$\mathring{A}$ and 6102$\mathring{A}$ and the c.w. laser transitions in Zn II at 4924$\mathring{A}$ and 4912$\mathring{A}$ and in Cd II at 7237$\mathring{A}$, 7284$\mathring{A}$, 6360$\mathring{A}$ and 6355$\mathring{A}$ are pumped by charge transfer reactions of the ground state atom He^+ ions populating the upper laser level directly. The c.w. laser transitions in CdII at 8067$\mathring{A}$, 8530$\mathring{A}$, 5378$\mathring{A}$ and 5337$\mathring{A}$ and in Zn II at 7588$\mathring{A}$ are pumped by cascade from a higher level populated by charge transfer from He^+ ions.

Another interesting feature concerning the relative cross-sections for charge transfer excitation is that any simple correlation between cross-section and energy defect is conspicuously absent.

When using argon under the optimum flow conditions for maximum argon ion density it was only just possible to observe the transitions at 2062$\mathring{A}$ and 2026$\mathring{A}$ in Zn II and at 2145$\mathring{A}$ in Cd II, although these and other transitions are energetically accessible to argon ions (see Figures 3.7 and 3.8)

For reasons of economy neon was not used until a later stage in the experiments.

3-7 3-BODY REACTIONS

Assuming that radiative decay is the dominant mechanism for depopulation of excited levels then the relative intensity of all lines excited by charge transfer should be independent of the pressure

of neutral helium in the afterglow, and should display identical (linear) behaviour with change of ion density.

In order to confirm this plots of the intensities against pressure were compared at a constant mass flow rate. In the case of cadmium all the charge transfer excited lines displayed an identical pressure dependence, closely following the ion density as measured by the probes. In the case of zinc, however, lines originating from the 4f levels in Zn II displayed distinctive behaviour, as shown in Figure 3.9, indicating that the charge transfer reaction to the 4f levels favoured high pressure and that the intensity of the lines involved might be proportional to pressure as well as ion density.

The most sensitive test of the pressure dependence was to plot the intensity against ion density by altering the pumping speed, and the greatest pressure differential could be achieved by operating on the high pressure side of the curves shown in Figure 3.9. Such a plot is shown in Figure 3.10, in which the pressure is highest when the ion density is lowest. In plots of this type the pressure dependence of the intensities of transitions always fell into one of three classes, corresponding to the excitation mechanism of their upper levels:

i) Charge transfer excited, proportional to ion density alone,

ii) Charge transfer excited, proportional to ion density and proportional to pressure.

iii) Penning reaction excited, proportional to metastable density.

The interpretation of classes i) and iii) presents no difficulty as they show the pressure-independent behaviour expected of 2-body charge transfer and Penning reactions. However, although curves of class ii) and class iii) present a superficial similarity the discriminant techniques established unambiguously that the reactions involve different species.

In seeking an explanation of the pressure dependence shown by lines

of class ii) several possible mechanisms for the excitation of the upper level were considered.

1) The reaction involves a metastable helium atom as a third body. This explanation is rejected as the discriminants would have modified such a reaction had it taken place.

2) The reaction involves an ion or plasma electron acting as a third body. The explanation is rejected as the intensity of the lines concerned would have shown a quadratic rather than a sub-linear dependence on ion density.

3) The reaction involves collisional excitation by a plasma electron, which would be strongly influenced by a variation in electron temperature. This explanation is rejected as no such variation in electron temperature with pressure was detected.

4) The reaction involves excitation by a helium molecular ion. This explanation is rejected as the energetics of the reaction would require the helium molecular ion to be in a very high vibrational state, in which case the distinction between this and a 3-body reaction involving the atomic ion and a neutral helium atom is tenuous.

5) The reaction involves a neutral helium atom as a third body. This explanation would lead to the behaviour observed.

Further evidence concerning the possible 3-body reactions lies in the cross-sections involved. The cross-section for a third body to take part in a reaction is $\frac{1}{n v \tau}$ where n is the number density of the third body, v is its velocity and τ is the time deemed to be available for the third body to take part in the reaction. If τ is taken to be $< 10^{-8}$ sec substitution of the appropriate values for n and v leads

to the cro ss-section for interference as a third body in the reaction: $\sigma > 10^{3}$ Å^{2} for helium metastables or ions, $\sigma > 2\times10^{3}$ Å^{2} for electrons and $\sigma > 300$Å^{2} for neutral helium atoms. It is clear that it is a neutral helium atom which is most likely to be the 'third body' particle.

The helium can be involved either a) during the charge transfer or b) soon after, while the zinc ion is still in its initial excited state. Only an experiment which involved modulation of the population of the higher states in Zn II would determine with certainty which of these processes was occurring. However, although the time available for interference by a third body is greater in case b) (and equal to the lifetime of the 4f level) it seems unlikely that this is the explanation, for in the anomalous intensity ratio of the lines from the 6p, levels it is the level of higher energy that gives rise to a transition of greater intensity. Any disturbance of excited zinc ions would tend to reverse the intensity ratio, so its existence would tend to imply that such disturbances do not occur. Further, in case b), the lines of type ii) can grow in intensity only at the expense of a reduction in intensity of other lines. In the case of zinc a reduction in the intensity of transitions from the 5d level would not be noticeable. Measurements on selenium, however, established two classes of pressure-dependent behaviour in a similar fashion, and in this case no reduction in the intensity of the 2-body lines (much weaker than the 3-body lines) was observed. In addition the behaviour of every line followed one of the two patterns of behaviour very precisely, which would be most unlikely in the case of reactions of type b). In the case of magnesium all the lines indicated a 3-body reaction, which entirely eliminates reactions of type b).

In summary, the weight of evidence implies that when pressure-dependent intensities are measured with charge transfer reaction leading to excitation of the upper level involved is of the type

$$He^{+} + He + M \longrightarrow 2He + M^{+*}$$

REFERENCES

CHAPTER 3

1 Schmeltekopf A.L., and Broida, H.P., J. Chem. Phys., 39, 1261 (1963)

2 Dushman, S., 'Scientific Foundations of Vacuum Technique', New York: Wiley, (1962)

3 Johnson, E.O., and Malter, L., Phys. Rev., 80, 58 (1950)

4 Clements, R.M. and Skarsgard, H.M., Can. J. Phys., 45, 3199 (1967)

5 Jensen, R.C., Collins, G.J., and Bennet Jr., W.R., Phys. Rev. Lett., 23, 363 (1969)

6 Hasted, J.B., 'Physics of Atomic Collisions', London: Butterworths (1964)

7 Fehsenfeld, F.C., Schmeltekopf, A.L., Goldan, P.D., Schiff, H.I., and Ferguson, E.E. J. Chem. Phys. 44, 4087 (1966)

8 Huggins, R.W., and Cahn, J.H., J. Appl. Phys., 38, 180 (1967)

9 Sinda, T., Phys. Lett. 33A, 225 (1970)

10 Webb, C.E., Turner-Smith, A.R. and Green, J.M., J. Phys. B, 3, L135(1970

11 Collins, G.J., Thesis, Yale University (1970)

12 Mitchell, A.C.G., and Zemansky, M.W., 'Resonance Radiation and Excited Atoms', Cambridge University Press (1961)

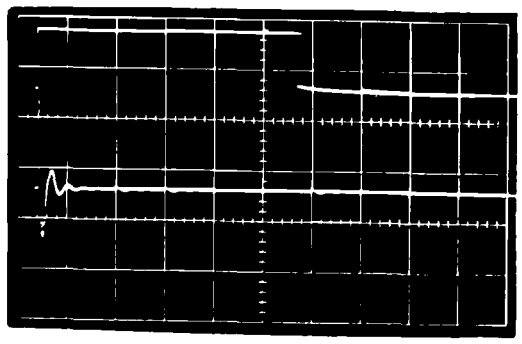

on
off

Microwave Power

Trigger Pulse

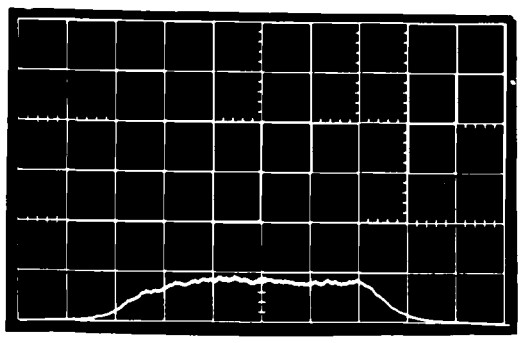

Pressure:

2·0torr

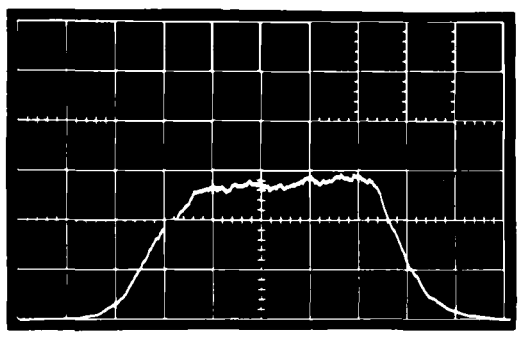

1·3torr

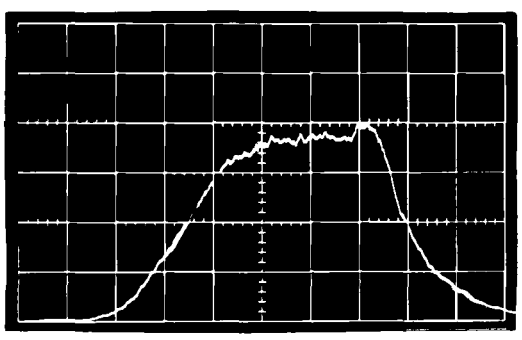

0·8torr

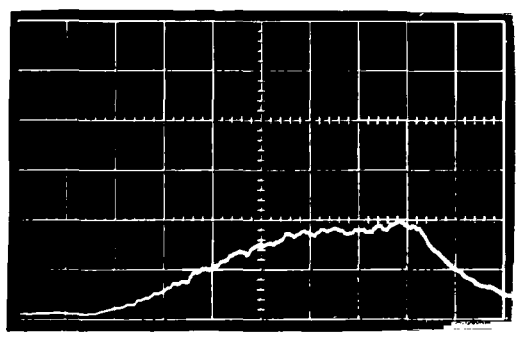

0·5torr

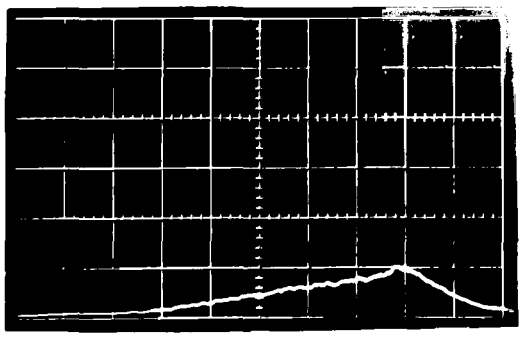

0·3torr

10ms

Figure 3.1 Pressure dependence of the pulsed afterglow

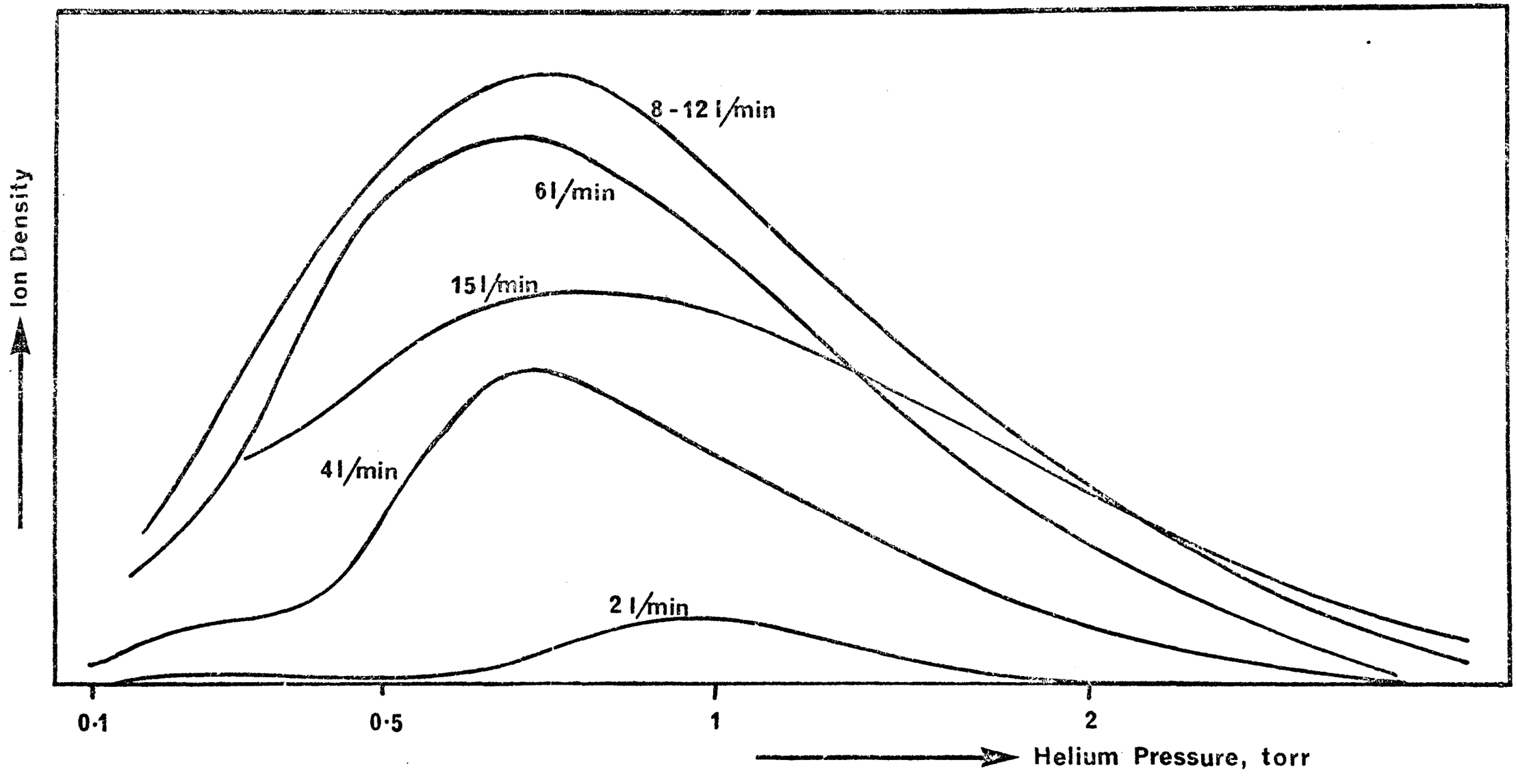

Figure 3.2 - Plasma density under various flow conditions
(tracing from original XY recording)

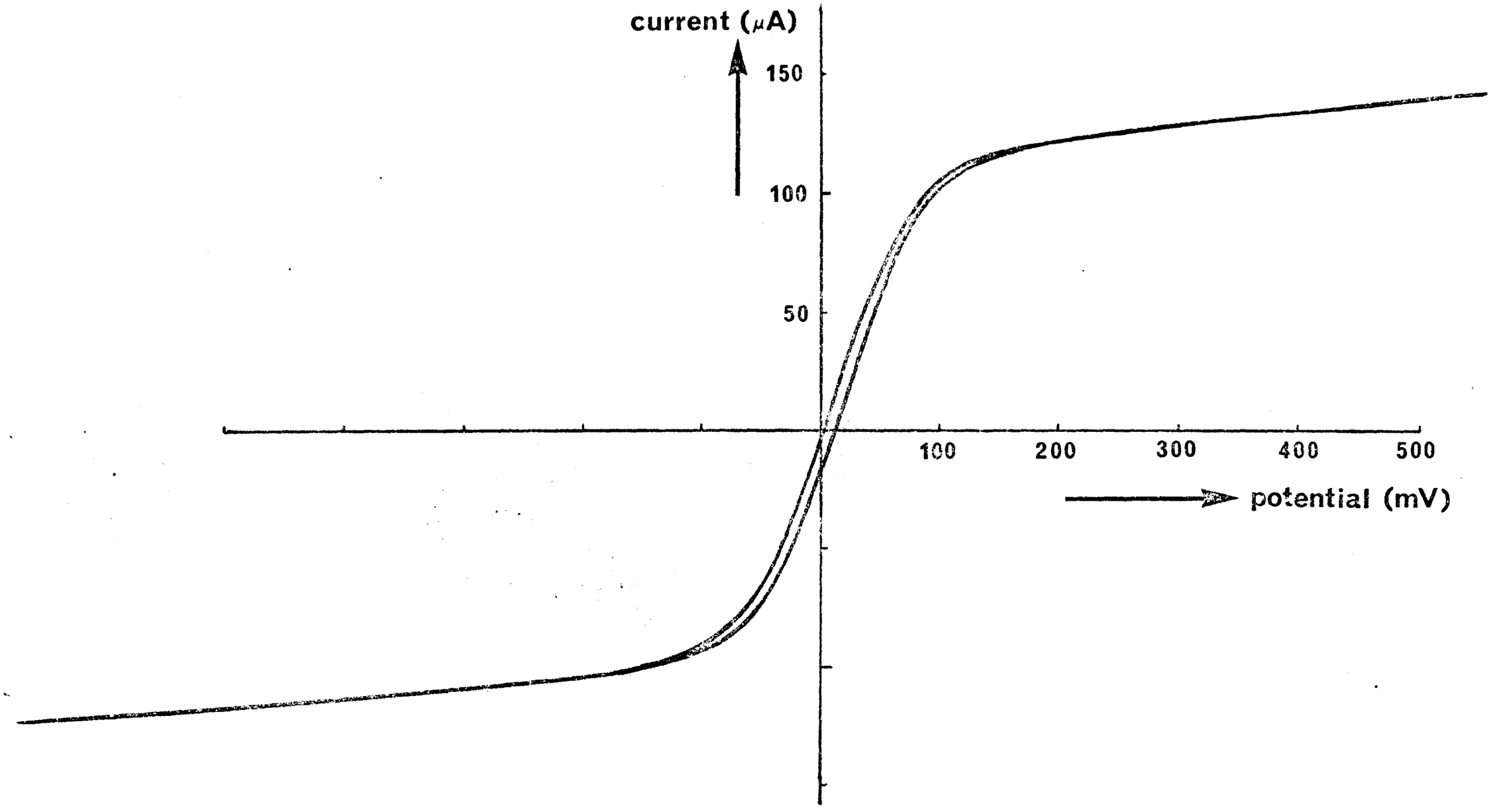

Figure 3.3 Typical Double Probe Characteristic
(tracing from original XY recording)

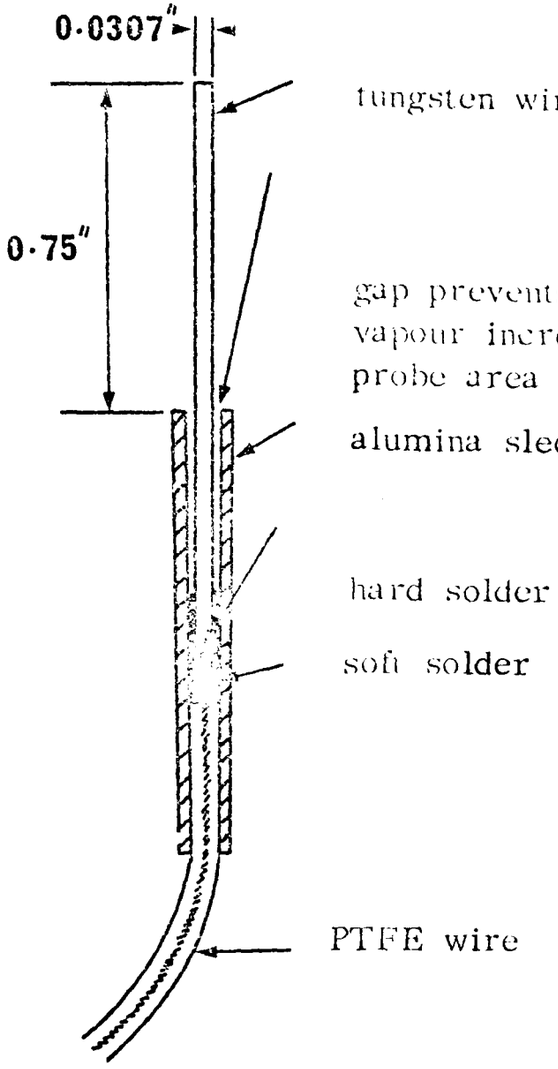

Figure 3.4(a) - Probe Dimensions

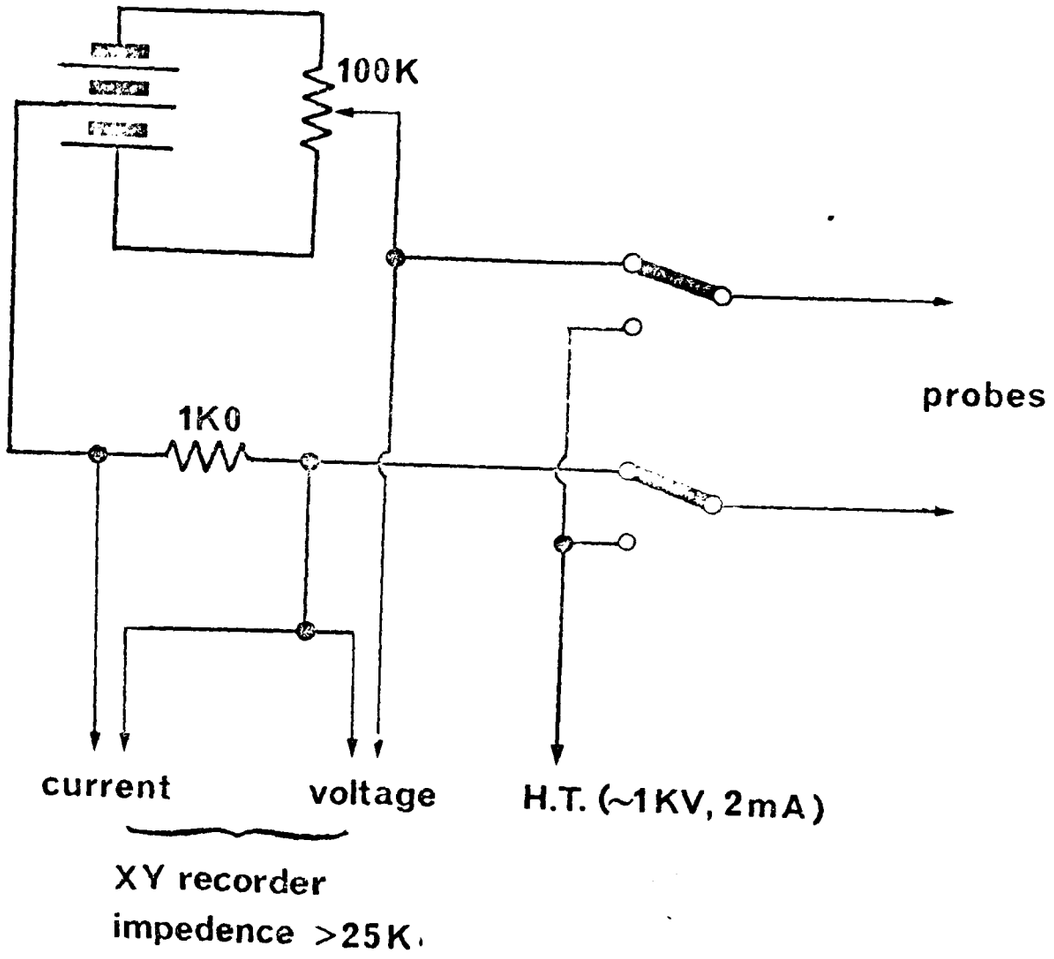

Figure 3.4(b) - Probe Circuit

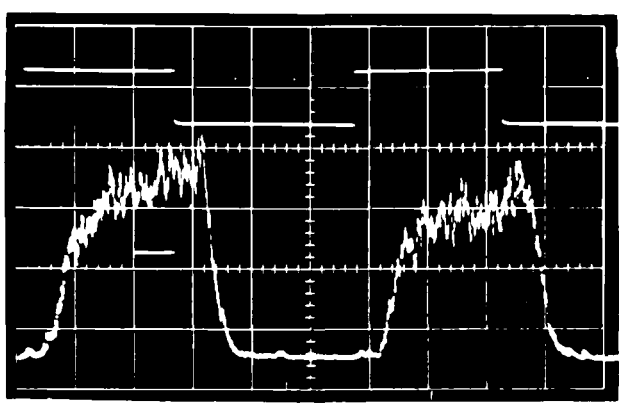

a) 5894 Å ZnII

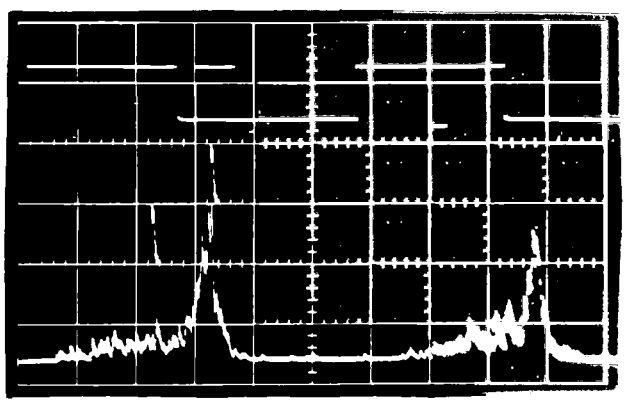

b) 6102 Å Zn II

Figure 3.5 Pulse behavior at low pressure

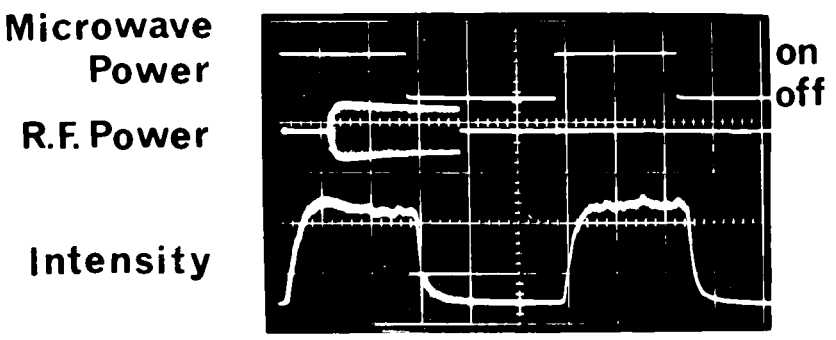

a) Penning Reaction

3250 Å Cd II

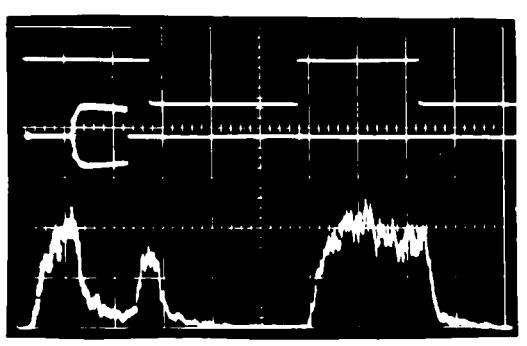

b) Charge Transfer

3417 Å Cd II

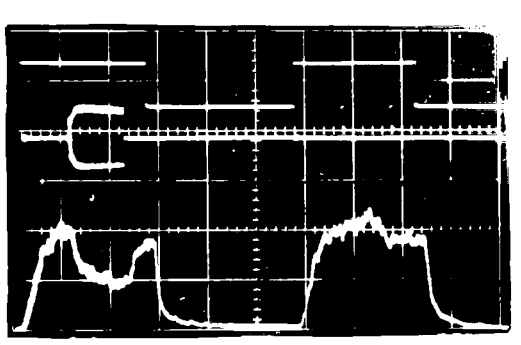

c) Charge Transfer and Penning Reaction

2749 Å Cd II

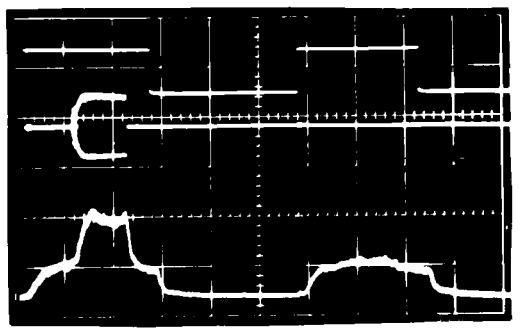

d) Neutral Cadmium

3261 Å Cd I

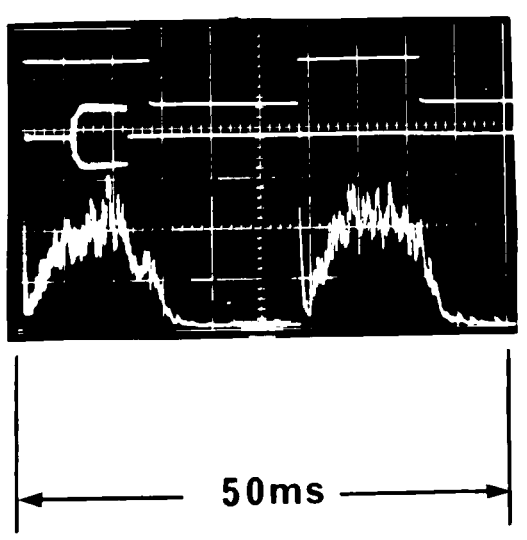

e) Neutral Helium

3888 Å He I

Figure 3.6 R.F. Discriminant

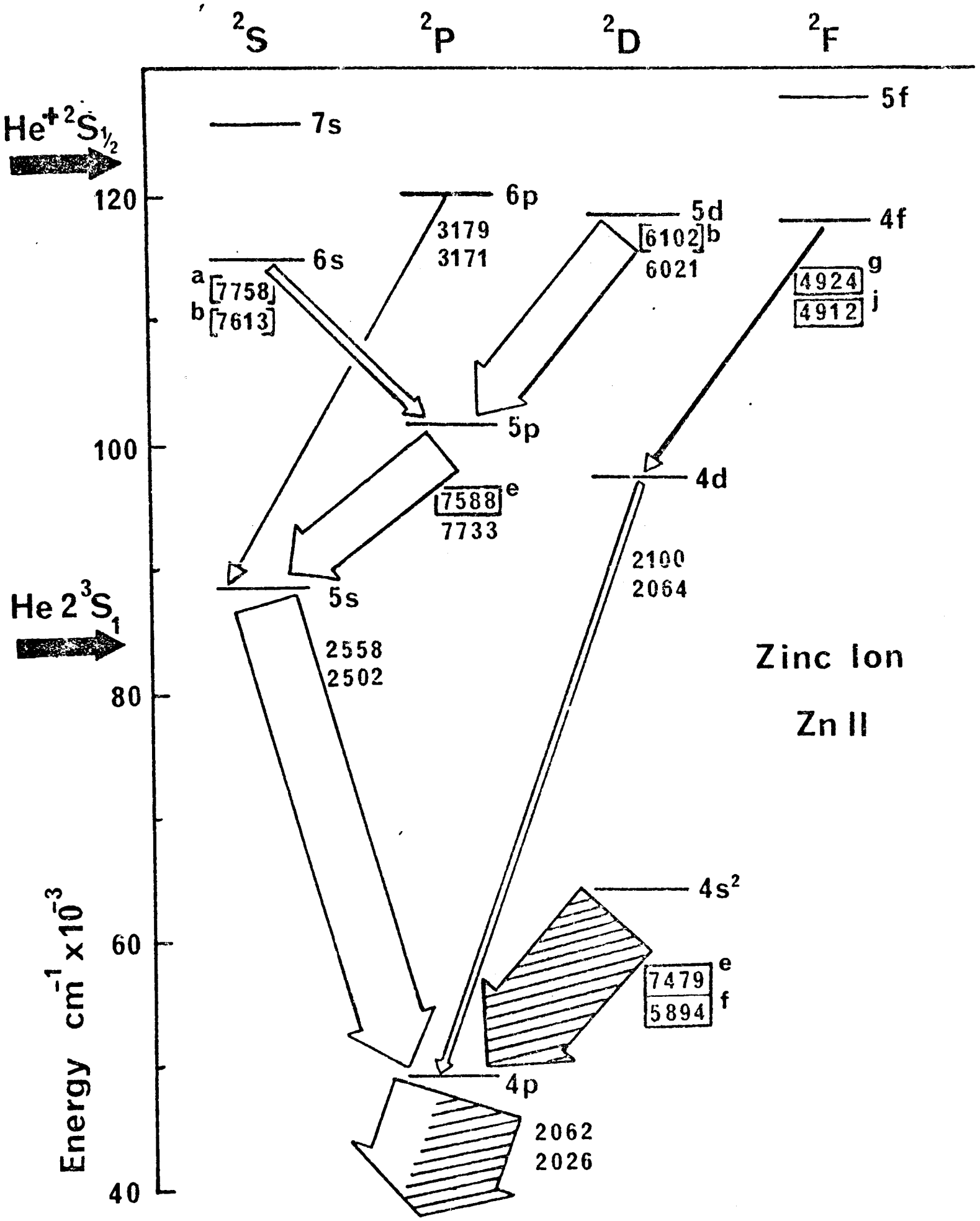

Figure 3.7 Energy levels of the zinc ion ZnII. Transitions excited by charge exchange reactions are indicated by open arrows, transitions excited by Penning reactions are indicated by cross-hatched arrows. Known c.w. laser transitions are indicated by boxed wavelengths; known pulsed laser transitions are indicated by bracketted wavelengths. References a) to i) appear after the tables in Chapter 4.

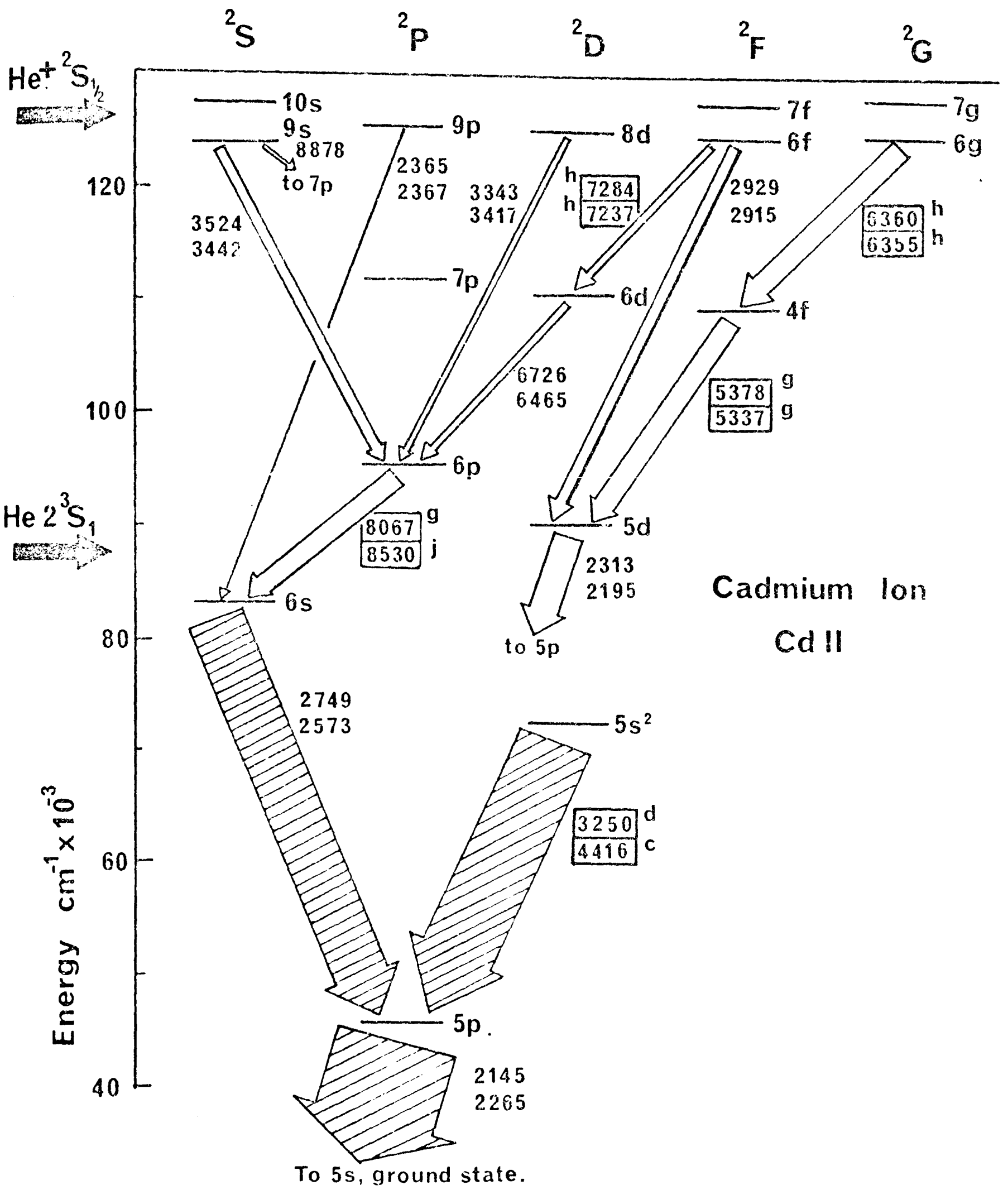

Figure 3.8 Energy levels of the cadmium ion CdII. Arrows and wavelengths are coded as in Figure 3.7.

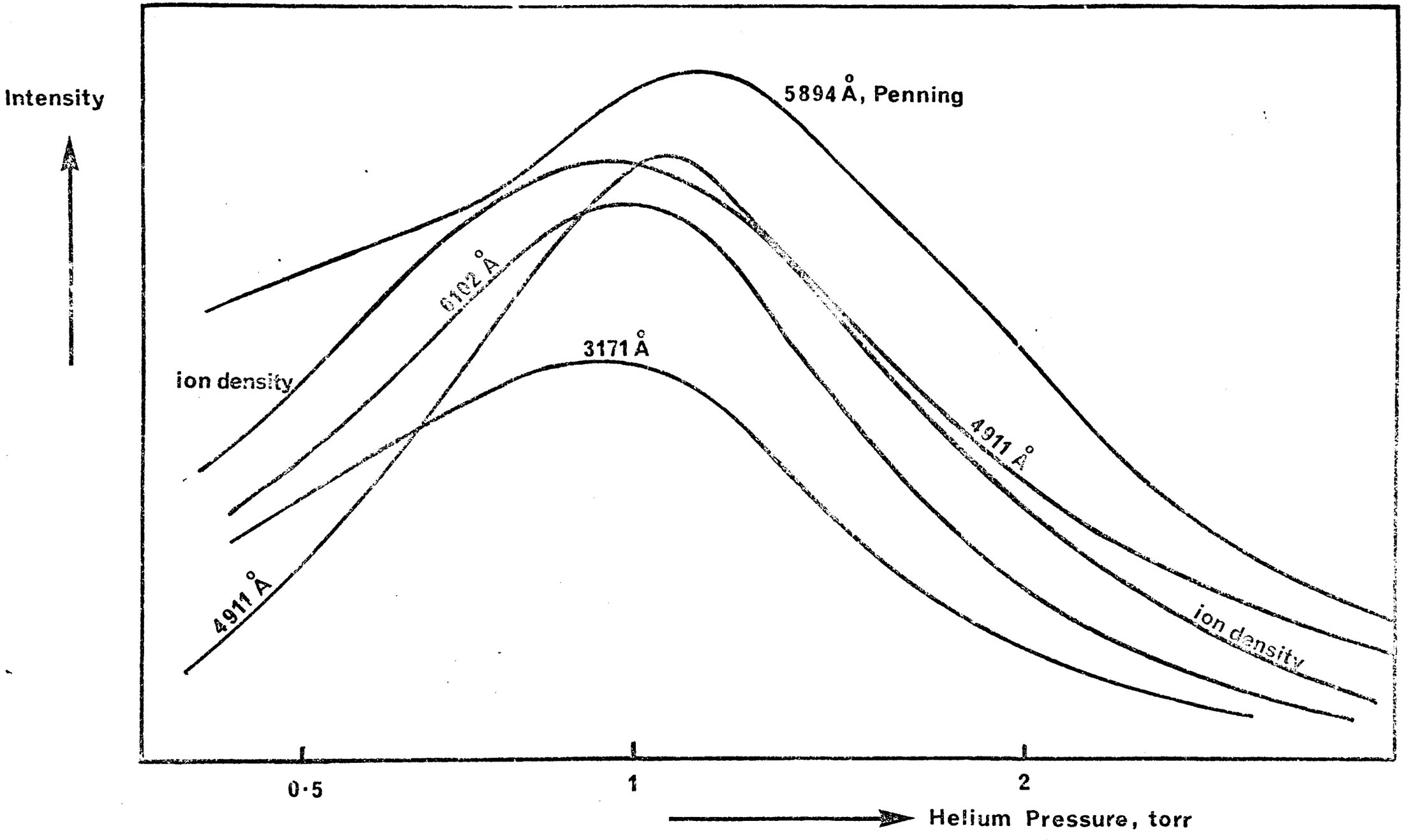

Figure 3.9 - Pressure dependence of some lines of Zn II, at a constant mass flow of 9l/min (tracing from original XY recording)

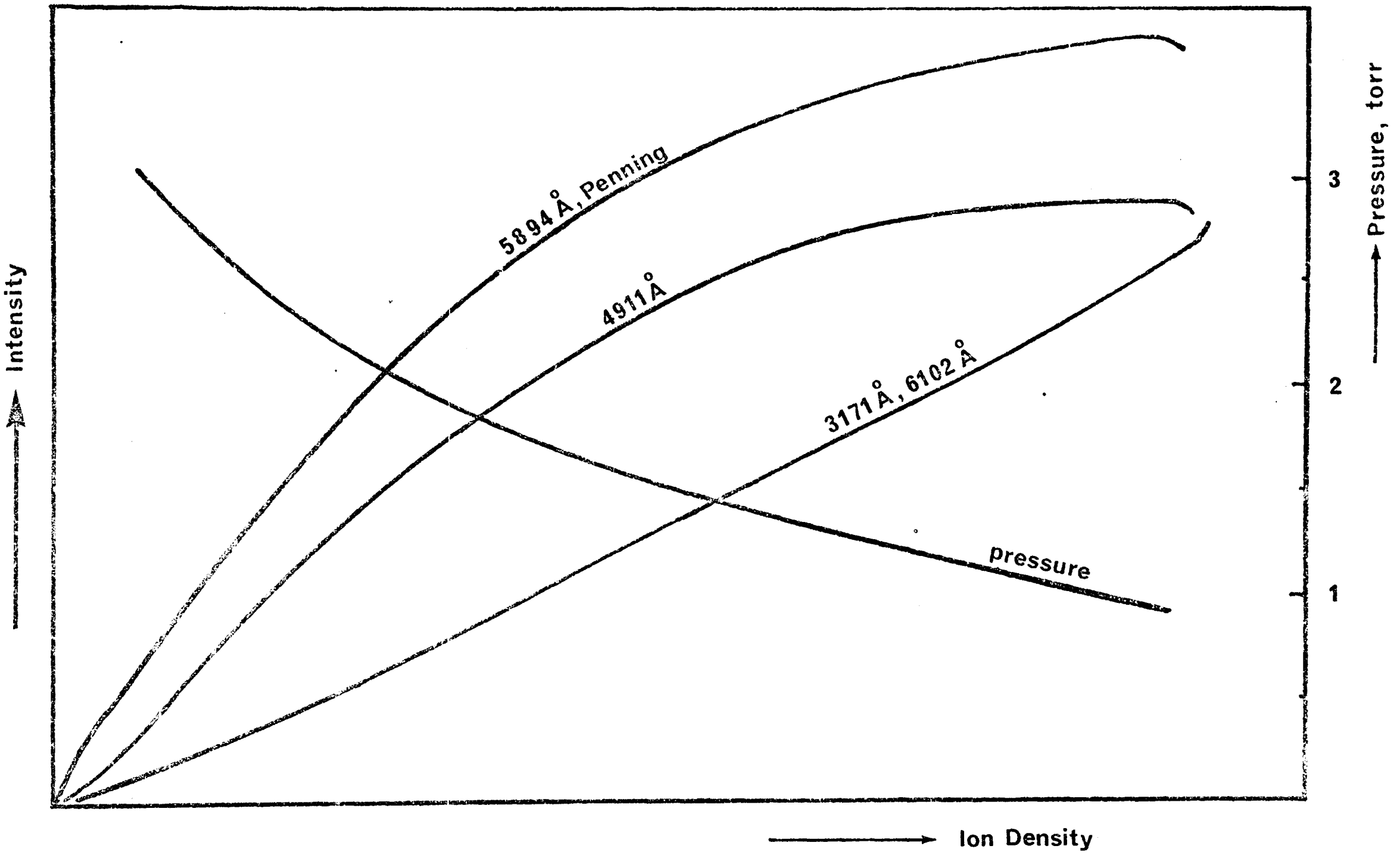

Figure 3.10 - 2-body/3-body discriminant
(tracing from original XY recording)

CHAPTER 4

RESULTS

'What we call results are beginnings'

Emerson

CHAPTER 4

RESULTS

In this chapter the intensity measurement data for the various reactions are tabulated, together with the excitation mechanism assigned to the upper level of each transition on the basis of the discriminant techniques described in Chapter 3. The five systems studied in detail were helium-zinc, neon-zinc, helium-cadmium, neon-magnesium and helium-selenium. The tables include an estimate of the relative reaction rates for charge transfer into most of the directly excited levels of these systems. The interpretation of this data is deferred to Chapter 6 in which a comparison is made with the available theories.

In addition to the detailed studies of the five systems listed above a cursory examination was made of reactions involving lead, aluminium and manganese, the prominant features of which are described in Section 4-7.

In this chapter the symbols He^+, Ne^+ and Ar^+ will be used specifically to denote the ground state energy of singly ionised helium, neon and argon respectively.

4-1 FURTHER EXPERIMENTAL DETAILS

A flow of pure neon could not be used for reasons of economy. Helium was therefore employed as a buffer gas, mixing the gases in a ratio by volume of 11 parts helium to 1 part crude neon (70% neon, 30% helium). Ion densities recorded by the probes in an afterglow of this mixture were of order 0.75 of the helium ion density under the same flow conditions with pure helium. With this mixture, helium ions, present as an 'impurity' in the afterglow, contributed no more than 1% to the measured intensity

in transitions excited by neon ions. This result was established by measuring the intensity of transitions originating from levels energetically inaccessible to neon ions but accessible to helium ions.

No evidence was found for the existence of helium metastables in the mixed afterglow, either by absorption measurements or by the r.f. discriminant. Absorption of 6402 Å in Ne I, however, established the density of the neon metastable Ne 3s $\left[1\frac{1}{2}\right]^{o}$ to be $> 10^{9}$ cm^{-3}, but no reliable estimate of the absolute metastable density could be inferred due to the large self-absorption in the line from the source lamp (Section 3-4).

Operation of the r.f. discriminant with neon was inconclusive, for no lines were seen to display behaviour characteristic of Penning excitation by neon metastables.

During the period of each experimental run (about 90 minutes) drifts of up to 30% were recorded in the intensity measurements. The drifts arose from fluctuations in the rate of evaporation of metal and, to a lesser extent, small changes in flow conditions and deposition of metal on the observation windows. The effect of such drifts on the accuracy of the data was minimised by averaging several readings of the intensity of each line during the period of observation.

4-2 CALCULATIONS ON THE DATA

4-2.1 Theoretical branching ratios

Lifetimes and branching ratios were calculated by use of the coulomb approximation method of Bates and Damgaard[1], extending their tables where necessary by use of the computational method of Friedrich, Katterbach and Trefftz[2]. The values quoted in the table were calculated using computer programmes developed by J.M. Green of this laboratory.

4-2.2 Extended calibration

An extrapolation to the spectral sensitivity calibration of the optical system was calculated by comparing photon rates down various cascade paths and by using the theoretical branching ratios to relate the intensity of transitions beyond the range of calibration to transitions between 3,000 Å and 8,000 Å. This method yielded only a few points on which to base the extrapolation, consequently the photon rates in lines outside the range 3,000 Å to 8,000 Å are likely to contain sizeable errors (of order 30%).

4-2.3 Accuracy

Calibration of the optical system between 3,000Å and 8,000Å is accurate to about 5% (Section 2-10), to which must be added the uncertainty in the calibrated colour temperature of the standard lamps (equivalent to about 5% in the calibration) and their relative spectral response (about 5%). Drifts, noise and other random observational errors add a further uncertainty of about 10% to the relative intensity of the stronger lines. In the case of the weaker lines the error is considerably greater. Thus the error in the final relative photon rates of the strongest transitions only is of order 15%.

An internal consistency check was provided by calculating the rate of population of a single level, as measured by the photon rates in two or more decay routes, through use of the theoretical branching ratios. The mean deviation of all such comparisons was 12%.

4-3 ZINC

4-3.1 Helium-Zinc

The helium ground state ion lies sufficiently low on the term diagram of Zn II (see Figure 3.7) to make analysis of the spectrum given in

Table 4.1(a) particularly simple. The only uncertainty lies in the classification of the line at 2265·51 Å. The most recent evaluation of the Zn II spectrum[3] does not include this line, whereas earlier work[4] has classified the transition as originating from a level too high to be excited by a Penning reaction, which is contrary to these observations.

The significance of the results to the proposed mechanisms for the Zn II laser lines has been mentioned in Section 3-6. The lifetime ratios given in Table 4.1(b) indicate that the pulse laser transitions at 6102Å, 7758Å and 7713Å are unlikely to be made to lase continuously. The transitions at 3171Å and 3179Å, however, appear to be promising candidates for c.w. laser action in that they posses a favourable lifetime ratio and their lower level is known to be the lower laser level of the transition at 7588Å.

Although 3-body reaction ratios listed in Table 4.1(b) are not directly comparable with 2-body cross-sections, the reaction rate into the 4f levels has been expressed as an equivalent 2-body cross-section evaluated for a pressure of 1 torr. The 3-body reactions were not included in the normalisation of the fractional cross-sections.

Within the accuracy of the measurements there is no evidence for direct excitation by charge transfer to levels with an energy defect greater than $10,000 cm^{-1}$. For levels of a smaller energy defect a systematic trend of reaction rate with energy defect is conspicuous by its absence. Moreoever there is no immediately obvious cause for the anomalously high ratio between the photon rates from $J = \frac{1}{2}$ and $J = 1\frac{1}{2}$ levels of the 6p doublet. Excitation of other levels appears to be proportional to the statistical weight of the level within each multiplet.

4-3.2 Neon -Zinc, Argon-Zinc

Data in Tables 4.2(a) and 4.2(b) has been normalised to enable a rough comparison to be made with the helium results. Normalisation included

factors for the ratio of intensity of the neon-excited spectrum and the helium-excited spectrum under similar flow conditions, and also the ratio of ion densities in the two cases. The reaction rates in neon appear to be of comparable magnitude with those in helium, but the pressure-dependence test implies that the 4d levels are populated by a 3-body reaction.

The distinction between 2-body and 3-body reactions in a neon afterglow depends entirely on the observation of 2-body behaviour in the lines at 2502Å and 2558Å originating from the 5s $^2S_{\frac{1}{2}}$ level in Zn II. In the case of magnesium (Section 4-5) all lines are observed to have a 3-body type of pressure dependence. Although the distinction of two types of behaviour with zinc would appear to verify the interpretation, the evidence for reaction types in neon cannot be considered conclusive until the two contrasting pressure dependences have been established as clearly as in the numerous helium results (Section 3-7).

On the basis of the helium and neon results a relatively fast charge transfer reaction rate would be expected from Ar^+ to Zn II ($4p\ ^2P_{1\frac{1}{2}}$) and Zn II ($4p\ ^2P_{\frac{1}{2}}$) at 1,989 cm^{-1} and 2,863 cm^{-1} respectively below Ar^+.

Specific attempts were made to observe the excitation of these levels in the argon afterglow. However, only extemely weak excitation of transitions from these levels (2026Å and 2062Å) was observed, insufficient for reliable intensity measurements.

4-4 CADMIUM

4-4.1 Helium-Cadmium

The term diagram of singly ionised cadmium is shown in Figure 3.8 and the data is given in Table 4.3(a) and 4.3(b). Particular features of the Cd II term diagram are the grouping of nine levels within 2,015 cm^{-1} of He^+ and the absence of anomolous pressure-dependence in any transition,

indicating that all levels were excited by 2-body reactions. These two features lend particular interest to the results presented in Table 4.3(b). Unlike the case of zinc no anomolous intensity ratios exist within the components of the doublets and, with the exception of the 9s level, the excitation rate bears a fairly smooth relationship with energy defect. The high excitation rate of the 5g levels may possibly be in error due to inaccurate calibration at wavelengths longer than 9,000Å. There is a strong likelihood, however, that the 5g levels are excited primarily by cascade from 6h levels, close in energy to the 5g and 6f levels. Transitions from the 6h levels do not appear classified in any spectroscopic literature so that their precise energy is therefore not known.

In addition to the conclusions concerning the pumping mechanism of lines in the cadmium laser, listed in Section 3-6, the analysis unambiguously assigns the pumping mechanism of the c.w. laser lines at 4881.7Å and 5025.5Å to charge transfer. The cascade contribution to the excitation rate of levels of the doublet system with energy defect greater than 7,500 cm^{-1} entirely masks the direct charge transfer excitation rate. No obvious decay paths from accessible higher levels in the quartet system exist, however, which might excite the upper levels of these intercombination transitions ($5p'\ ^4F_{5/2}$ and $5p'\ ^4F_{7/2}$, 15,598 cm^{-1} and 16,029 cm^{-1} below He^+ respectively). The possibility of direct charge transfer to these levels, therefore, cannot be ruled out.

Transitions were also observed in the doublet spectrum of the same core, from the levels of $5p\ ^2F_{5/2}$ and $5p\ ^2F_{7/2}$ which lie within 8,900 cm^{-1} of He^+. Although theoretical values for intercombination lines cannot be calculated, the four $5p'$ levels have been included in Table 4.1(b) by use of very crude values for the branching ratios derived from intensities quoted in the literature[6].

The lifetime ratios listed in Table 4.3(b) indicate that there may be many further laser transitions in the helium-cadmium system. In

particular the transitions to 2914.7Å and 2929.3Å from the 6f levels to the 5d levels would appear to be particularly promising candidates as both their upper and lower levels are associated with known laser transitions.

Although it is likely that the 8p levels are directly populated by charge transfer the oscillator strengths of transitions from these levels which lie in the range of detection capability are very low. No transitions from the 8p levels were observed.

4-4.2 Neon-Cadmium and argon-cadmium

The closest level in Cd II ($6p\ ^2P_{1\frac{1}{2}}$) lies 6,009 cm^{-1} below Ne^+. No transitions resulting from excitation of this level were observed. The line at 2265Å from the $5p\ ^2P_{\frac{1}{2}}$ level, however, was excited in the neon afterglow. As this was the only line observed it is likely that it originated from a Penning reaction from Ne ($3s\ [1\frac{1}{2}]_2$), 17,369 cm^{-1} above Cd II ($5p\ ^2P_{\frac{1}{2}}$).

The only levels accessible to Ar^+ give rise to transitions at 2265Å and 2145Å, neither of which were observed. The closest level ($5p\ ^2P_{1\frac{1}{2}}$) lies 7,953 cm^{-1} below Ar^+, however, so no strong excitation would be expected.

4-5 MAGNESIUM

He^+ lies 15,368 cm^{-1} above the second ionisation limit of magnesium. The spectrum of Mg II was nevertheless strongly excited in a helium afterglow, with intensities determined largely by the particular oscillator strengths involved in the cascade paths in the Mg II energy level system. In contrast, Ar^+ lies 29,680 cm^{-1} above the closest magnesium level, Mg II ($3p\ ^2P_{1\frac{1}{2}}$). It is not surprising, therefore, that no transitions were observed from Mg II in an argon afterglow.

The Mg II spectrum in a neon afterglow was bright, the glow presenting the blue colour characteristic of Mg II, rather than the green colour

characteristic of Mg I (Figure P1). A partial term diagram of Mg II is given in Figure 4.1 , which shows that 20 levels lie within 3,478 cm^{-1} of Ne^{+}. The data in Tables 4.4a, analysed in Table 4.4b, reveals that charge transfer takes place directly to each of these levels. Table 4.4b has been extended to include levels with large energy defects. In the case of these lower levels the contribution by cascades, derived from observed and computed photon rates from higher levels, can account completely for their rate of population, within the accuracy of the data.

The doublet splittings of the levels of interest in Mg II are small and in consequence in many cases it was not possible to resolve the doublets. In these cases the excitation rate to the doublet as a whole has been estimated.

Although no transitions from the 6h and 7h levels were available in the range of detection, the photon rate in the transition at 10,092.2Å from the 5g levels probably represents the entire excitation rate of the 6h and 7h levels (assuming, as seems likely from levels of similar energy defect, that there is no appreciable direct excitation of the 5g level). It follows from this assumption and the trends of the other results that the figures for the excitation rates listed in column (11) of Table 4.4b would be 21 (into 6h) and 14 (into 7h).

The pressure dependence of all lines was the same and indicated that the charge transfer processes involved a third body (a neutral helium atom). The evidence cannot be considered conclusive, however, because the two characteristic pressure dependences have not been fully established (see Section 4-3.2).

4-6 SELENIUM

The investigation of selenium in a helium afterglow was prompted by the discovery by Silfvast and Klein[5] of 24 c.w. laser transitions in

Se II. The energy level structure of selenium is too complicated to enable theoretical branching ratios to be calculated and Tables 4.5a and 4.5b have been set out in an appropriately modified form. The term diagram of Se II contains a gap of about 60,000 cm^{-1} between levels near the ground state and levels grouped about Ne^+ and He^+. In consequence no levels are available for excitation by helium metastables or argon ions. Excitation by charge transfer from Ne^+ could only give rise to transitions in the deep ultra violet, beyond the detection capability of the optical system.

The most striking systematic feature of the data is the division of the pressure behaviour of emission intensities into that typical of 2-body reactions for the higher levels and that typical of 3-body reactions for the lower levels, when the greater energy defect can more easily be accommodated due to availability of the third particle to take up the surplus energy.

Selenium was the only material to emit radiation originating from levels significantly higher in energy than He^+. A possible explanation for this feature lies in the existence of two metastable levels in the neutral atom, close to the ground state, from which charge transfer could have taken place. An attempt was made to measure the population of the metastable levels of Se I in the flow tube by optical absorption. This failed, however, because no sufficiently intense source emitting the required lines could be obtained. Although a high temperature (of order 2,000 K) would be necessary to yield a significant population in the metastable Se I levels by thermal collisional excitation, it is possible that during the process of molecular dissociation of the selenium vapour (consisting of Se_2, Se_4, Se_6 and Se_8), which takes place before the charge transfer reactions can occur, Se I is formed in an excited state. The process responsible for the dissociation in the (cold) afterglow plasma is a

matter for conjecture.

Two laser lines are omitted from Table 4.4b because it is uncertain on which upper level they originate. The line at 5253.6Å displayed pressure-dependent behaviour typical of a 3-body reaction. All other transitions from its assigned upper level, 5p $^2D_{5/2}$, displayed 2-body reaction behaviour, which indicated that the assignment of the line was incorrect. Similarly, the line at 5096.5Å, assigned to 5p $^4D_{7/2}$ as an upper level, displayed 2-body rather than the 3-body behaviour shown by the line at 5227.5Å from the same level.

In Table 4.5b, 2-body and 3-body reaction rates have been normalised to a pressure of 1 torr. The analysis presented by this table is of necessity incomplete, due to lack of knowledge of the branching ratios. However the reaction rate per unit statistical follows a fairly smooth trend with the energy defect.

4-7 OTHER METALS

4-7.1 Aluminium

He^+ lies near the ionisation limit of Al II and in consequence there are many levels which may be populated by charge transfer from the helium ion. Only measurements in the far infra-red spectrum, however, would yield useful data on the charge transfer processes. The spectrum in Al II was strongly excited by the helium afterglow, with the relative intensities of the lines similar to those listed in the literature for the spark-excited aluminium spectrum.

Some lines whose upper levels were accessible to He($2\,^3S_1$), displayed behaviour characteristic of Penning excitation (eg 4663Å from Al II ($4p\,^1P_1$) 4,653 cm below He ($2\,^3S_1$)).

The spectrum with neon was weaker, with lines in the singlet spectrum

particularly feeble. No transitions were observed from the 5p (^3P_o) level, 50 cm^{-1} above Ne^+ although lines from the triplet levels, 4d ^3D ($\sim$4,170 cm^{-1} below Ne^+) were among the strongest in the spectrum. Although Al II in a neon afterglow provides a fairly simple spectrum to analyse, the practical problem of evaporating the metal at a sufficient rate over an extended period of time proved severe.

No Al II spectrum was observed in the argon afterglow as the closest level (Al II ($3p\ ^1P_1$)) lies 18,981 cm^{-1} below Ar^+.

4-7.2 Lead

He^+ lies 36,22 cm^{-1} above the second ionisation limit of lead, but nevertheless the helium afterglow excited the entire Pb II spectrum quite strongly. Some transitions, all from levels below the He ($2\ ^3S_1$) energy, were excited by Penning reactions.

The spectrum in neon is much weaker, although there are many levels in close coincidence with Ne^+. The only level close enough for charge transfer from Ar^+ is Pb II ($6p^2\ ^3P_{1\frac{1}{2}}$), 1,165 cm^{-1} below Ar^+. Transitions from this level lie at wavelengths shorter than 2,000A where the detection sensitivity was very low. No transition in Pb II was observed in an argon afterglow.

4-7.3 Manganese

Although a detailed analysis of results in manganese is not possible, due to the complexity of its energy level structure, interest lay in the numerous close coincidences of Ar^+ with levels in Mn II in the quintet system (8 levels within 608 cm^{-1}). However, the only lines observed in the argon afterglow originated from the septet system. No transitions were observed from the levels in close energy coincidence with Ar^+. Further complication in the spectrum arose from the excitation of lines originating from levels above Ar^+ (which may be due to excitation from metastable levels in Mn I, See Section 4-6).

The Mn I spectrum was strongly excited by helium, neon and argon afterglows, but only a few lines in Mn II were observed in helium and neon afterglows.

REFERENCES

1 Bates D.R., and Damgaard, A., Phil.Trans., 242, 101 (1949)

2 Friedrich, H., Katterbach, K. and Trefftz, E., J. Quant.Rad.Trans., 10, 11 (1970)

3 Crooker, A.M. and Dick, K.A., Can.J.Phys., 46, 1241 (1968)

4 Takahashi, Y., Ann.der Phys., 3, 27 (1929)

5 Silfvast, W.T. and Klein, M.B., Unpublished.

6 Shenstone, A.G. and Pittenger, J.T., J.Opt.Soc.Am., 39, 220 (1949)

NOTES ON THE TABLES

Column 1 — Wavelengths are quoted from the literature. In cases of uncertainty special calibration of the monochromator permitted lines to be identified to $\pm$ 0.05Å.

Column 3 — In the case of levels from which transitions occur which involve more than one electron jump the lifetime quoted, although a good approximation, strictly represents an upper limit. Values are rounded to two significant figures.

Column 4 — Branching ratios are based on calculations which ignore transitions involving more than one electron jump. Values are rounded to two significant figures.

Column 5 — The scale of relative photon rates is not comparable between the various tables.

Column 6 — 'Character' refers to the behaviour of the line with respect to the r.f. and argon titration discriminants:

- I signifies a line from a level excited by charge transfer (directly or by cascade from a higher level).
- P signifies a line from a level excited by a Penning reaction (directly or by cascade).
- I/P (ratio) signifies a line displaying both characters, with a very crude estimate of the ratio of ion excitation to metastable excitation.

Numbers 2 and 3 refer to pressure behaviour typical of a 2-body or a 3-body excitation process.

Column 10 — Relative total rate of photons out of a level.

Column 11 — Relative rate of direct excitation of the level by charge transfer, calculated from a mean of the values in column 10, with appropriate weighting for values of low probable accuracy. Tables are discontinued at the levels at which calculated cascade contributions into the level become comparable to the rate of photons out of the level (illustrated by the extension to Table 4.4b).

Column 12 — Relative excitation rate per unit statistical weight of the level.

Column 13 — Relative excitation rate normalised to a total into all levels by charge transfer of unity.

Column 14 — Upper level lifetime divided by the lower level lifetime.

The letters a) to m) are references to literature on laser lines and other information, listed at the end of the tables.

TABLE 4.1(a)

HELIUM-ZINC DATA
measured at 1.0 torr

(1) Air Wavelength Å	(2) Classification	(3) Upper level lifetime, ns	(4) Branching ratio, R	(5) Relative photon rate, $\dot{N}$	(6) Character
2025.45	$4p\ ^2P_{3/2} \rightarrow 4s\ ^2S_{1/2}$	2.0	1.0	1330	I/P (2.7)
2062.02	$4p\ ^2P_{1/2} \rightarrow 4s\ ^2S_{1/2}$	2.2	1.0	640	I/P (2.6)
2064.23	$4d\ ^2D_{3/2} \rightarrow 4p\ ^2P_{1/2}$	1.3	0.84	16	I
2099.90	$4d\ ^2D_{5/2} \rightarrow 4p\ ^2P_{3/2}$	1.3	1.0	280	I
2102.17	$4d\ ^2D_{3/2} \rightarrow 4p\ ^2P_{3/2}$	1.3	0.16	8.5	I
2210.18	$4p'\ ^2F_{5/2} \rightarrow 4s^2\ ^2D_{3/2}$	-	-	2.3	I
2265.51	Classification uncertain		-	13	I/P (1.4)
2501.99	$5s\ ^2S_{1/2} \rightarrow 4p\ ^2P_{1/2}$	2.5	0.34	130	I
2557.95	$5s\ ^2S_{1/2} \rightarrow 4p\ ^2P_{3/2}$	2.5	0.66	320	I
2570.65	$5p\ ^2P_{3/2} \rightarrow 4s^2\ ^2D_{5/2}$	18	-	6.7	I
2763.96	$5p\ ^2P_{3/2} \rightarrow 4s^2\ ^2D_{3/2}$	18	-	0.39	I
2782.81	$5p\ ^2P_{1/2} \rightarrow 4s^2\ ^2D_{3/2}$	18	-	2.2	I
3171.45	$6p\ ^2P_{3/2} \rightarrow 5s\ ^2S_{1/2}$	68	0.093	14	I 2
3178.59	$6p\ ^2P_{1/2} \rightarrow 5s\ ^2S_{1/2}$	73	0.080	1.6	I 2
3988.96	$4p'\ ^2P_{3/2} \rightarrow 5s\ ^2S_{1/2}$	3.7	-	0.19	I
3989.96	$4p'\ ^2P_{1/2} \rightarrow 5s\ ^2S_{1/2}$	3.7			
4911.62[j]	$4f\ ^2F_{5/2} \rightarrow 4d\ ^2D_{3/2}$	4.8	0.93	21	I 3
4923.9	$4f\ ^2F_{5/2} \rightarrow 4d\ ^2D_{5/2}$	4.8	0.066	41	I 3
4924.03[g]	$4f\ ^2F_{7/2} \rightarrow 4d\ ^2D_{5/2}$	4.8	1.0		
5894.33[f]	$4s^2\ ^2D_{3/2} \rightarrow 4p\ ^2P_{1/2}$	-	-	150	P
6021.18	$5d\ ^2D_{3/2} \rightarrow 5p\ ^2P_{1/2}$	3.2	0.28	150	I 2
6102.49[b]	$5d\ ^2D_{5/2} \rightarrow 5p\ ^2P_{3/2}$	3.3	0.34	340	I 2

Table 4.1(a) Contd..

(1)	(2)	(3)	(4)	(5)	(6)
6111.53	$5d\ ^2D_{\frac{3}{2}} \rightarrow 5p\ ^2P_{\frac{3}{2}}$	3.2	0.055	30	I 2
6214.61	$4s^2\ ^2D_{\frac{3}{2}} \rightarrow 4p\ ^2P_{\frac{3}{2}}$	-	-	25	P
7478.8[e]	$4s^2\ ^2D_{\frac{5}{2}} \rightarrow 4p\ ^2P_{\frac{3}{2}}$	-	1.0	490	I/P (0.5)
7588.5[g]	$5p\ ^2P_{\frac{3}{2}} \rightarrow 5s\ ^2S_{\frac{1}{2}}$	18	0.85	310	I
7613.02[b]	$6s\ ^2S_{\frac{1}{2}} \rightarrow 5p\ ^2P_{\frac{1}{2}}$	4.7	0.14	25	I 2
7732.63	$5p\ ^2P_{\frac{1}{2}} \rightarrow 5s\ ^2S_{\frac{1}{2}}$	18	0.89	120	I
7757.97[a]	$6s\ ^2S_{\frac{1}{2}} \rightarrow 5p\ ^2P_{\frac{3}{2}}$	4.7	0.27	53	I 2

TABLE 4.1(b)

HELIUM-ZINC CHARGE TRANSFER

(7) Upper Level	(8) Energy Defect cm^{-1}	(9) Air wavelength Å	(10) Relative $\dot{N}/R$	(11) Average $\dot{N}/R$ less cascades	(12) Reaction rate per unit st. wt.	(13) Fractional cross-section at 1 torr	(14) Lifetime ratio
$6p\,^2P_{\frac{3}{2}}$	2,579	3171.5	150	150	38	0.083	27
$6p\,^2P_{\frac{1}{2}}$	2,650	3178.6	20	20	10	0.011	29
$5d\,^2D_{\frac{5}{2}}$	4,545	6102.5	1,000	1,000	170	0.55	0.2[b]
$5d\,^2D_{\frac{3}{2}}$	4,570	6021.2 6111.5	540 540	540	135	0.30	0.2 0.2
$4f\,^2F_{\frac{5}{2}}$	5,275	4911.6	22	22	3.7	0.012 (3 body)	3.7[j]
$4f\,^2F_{\frac{7}{2}}$	5,276	4924.0	40	40	5	0.022 (3 body)	3.7[g]
$6s\,^2S_{\frac{1}{2}}$	8,040	7613.0 7758.0	180 200	190-94 = 96	48	0.053	0.26[b] 0.26[a]

TABLE 4.2(a)

NEON-ZINC DATA
measured at 1.1 torr helium + 0.1 torr crude neon

(1) Air wavelength, Å	(2) Classification	(3) Upper level lifetime, ns	(4) Branching ratio, R	(5) Relative photon rate, $\dot{N}$	(6) Character
2025.45	$4p^2\,^2P_{3/2} \rightarrow 4s\,^2S_{1/2}$	2.0	1.0	360	I 3
2062.02	$4p\,^2P_{1/2} \rightarrow 4s\,^2S_{1/2}$	2.2	1.0	150	I 3
2064.23	$4d\,^2D_{3/2} \rightarrow 4p\,^2P_{1/2}$	1.3	0.84	140	I 3
2099.90	$4d\,^2D_{5/2} \rightarrow 4p\,^2P_{3/2}$	1.3	1.0	280	I 3
2102.17	$4d\,^2D_{3/2} \rightarrow 4p\,^2P_{3/2}$	1.3	0.16	24	I 3
2265.51	Classification uncertain		-	0.94	I 3
2501.99	$5s\,^2S_{1/2} \rightarrow 4p\,^2P_{1/2}$	2.5	0.34	1.9	I 2
2557.95	$5s\,^2S_{1/2} \rightarrow 4p\,^2P_{3/2}$	2.5	0.67	5.1	I 2

TABLE 4.2(b)

NEON-ZINC CHARGE TRANSFER

(7) Upper level	(8) Energy defect cm^{-1}	(9) Air wavelength Å	(10) Relative $\dot{N}/R$	(11) Average $\dot{N}/R$ less cascades	(12) Reaction rate per unit st. wt.	(13) Fractional reaction rate at 1.2 torr	(14) Lifetime ratio
$4d\,^2D_{5/2}$	1,205	2099.9	280	280	45 (3-body)	0.51	0.65
$4d\,^2D_{3/2}$	1,256	2064.2 2102.2	170 150	160	40 (3-body)	0.45	0.59 0.65
$5s\,^2S_{1/2}$	9,728	2502.0 2558.0	5.7 7.7	6.7	3.3	0.04	1.1 1.3

TABLE 4.3(a)

HELIUM-CADMIUM DATA

Measured at 1.4 torr

(1) Air Wavelength $\overset{o}{A}$	(2) Classification	(3) Upper level lifetime, ns.	(4) Branching ratio, R	(5) Relative photon Rate, $\dot{N}$	(6) Character
2144.41	$5p\ ^2P_{3/2} \rightarrow 5s\ ^2S_{1/2}$	2.2[k]	1.0	1,500	I/P (0.5)
2194.56	$5d\ ^2D_{3/2} \rightarrow 5p\ P_{1/2}$	6.5[k]	0.84	150	I
2265.02	$5p\ ^2P_{1/2} \rightarrow 5s\ ^2S_{1/2}$	5.1[k]	1.0	700	I/P (1.3)
2312.77	$5d\ ^2D_{5/2} \rightarrow 5p\ ^2P_{3/2}$	6.1[k]	1.0	240	I
2321.07	$5d\ ^2D_{3/2} \rightarrow 6p\ ^2P_{3/2}$	6.5[k]	0.16	22	I
2365.36	$9p\ ^2P_{3/2} \rightarrow 6s\ ^2S_{1/2}$	320	0.0067	0.26	I
2367.13	$9p\ ^2P_{1/2} \rightarrow 6s\ ^2S_{1/2}$	390	0.0044	0.16	I
2572.93	$6s\ ^2S_{1/2} \rightarrow 5p\ ^2P_{1/2}$	2.2[k]	0.34	120	I/P (2.9)
2748.55	$6s\ ^2S_{1/2} \rightarrow 5p\ ^2P_{3/2}$	2.2[k]	0.66	350	I/P (2.9)
2813.39	$9p\ ^2P_{1/2} \rightarrow 5d\ ^2D_{3/2}$	390	0.014	0.30	I
2823.19	$9p\ ^2P_{3/2} \rightarrow 5d\ ^2D_{5/2}$	320	0.013	0.44	I
2914.67	$6f\ ^2F_{5/2} \rightarrow 5d\ ^2D_{3/2}$	24	0.34	48	I
2929.27	$6f\ ^2F_{7/2} \rightarrow 5d\ ^2D_{5/2}$	25	0.35	57	I
3250.33[d]	$5s^2\ ^2D_{3/2} \rightarrow 5p\ ^2P_{1/2}$	260[k]	-	560	P
3343.21	$8d\ ^2D_{3/2} \rightarrow 6p\ ^2P_{1/2}$	16	0.24	20	I
3385.49	$5p'\ ^2F_{7/2} \rightarrow 5d\ ^2D_{5/2}$	-	0.11[m]	4.8	I
3388.88	$7p\ ^2P_{3/2} \rightarrow 6s\ ^2S_{1/2}$	50	0.095	2.6	I
3417.49	$8d\ ^2D_{5/2} \rightarrow 6p\ ^2P_{3/2}$	17	0.28	41	I
3420.19	$8d\ ^2D_{3/2} \rightarrow 6p\ ^2P_{3/2}$	16	0.042	3.7	I
3442.42	$9s\ ^2S_{1/2} \rightarrow 6p\ ^2P_{1/2}$	15	0.083	43	I
3464.43	$5f\ ^2F_{5/2} \rightarrow 5d\ ^2D_{3/2}$	12	0.47	40	I
3495.44	$5f\ ^2F_{7/2} \rightarrow 5d\ ^2D_{5/2}$	13	0.47	53	I

Table 4.3(a) Contd..

(1)	(2)	(3)	(4)	(5)	(6)
3524.11	$9s\ ^2S_{\frac{1}{2}} \rightarrow 6p\ ^2P_{\frac{3}{2}}$	15	0.16	75	I
3535.69	$5s^2\ ^2D_{\frac{3}{2}} \rightarrow 5p\ ^2P_{\frac{3}{2}}$	260[k]	-	96	P
3666.76	$5p'\ ^2F_{\frac{5}{2}} \rightarrow 5d\ ^2D_{\frac{3}{2}}$	-	0.58[m]	0.7	I
4029.12	$7d\ ^2D_{\frac{3}{2}} \rightarrow 6p\ ^2P_{\frac{1}{2}}$	7.2	0.21	12	I
4134.77	$7d\ ^2D_{\frac{5}{2}} \rightarrow 6p\ ^2P_{\frac{3}{2}}$	7.8	0.25	23	I
4415.63[c]	$5s^2\ ^2D_{\frac{5}{2}} \rightarrow 5p\ ^2P_{\frac{3}{2}}$	783[k]	1.0	1,000	P
4881.73[i]	$5p'\ ^4F_{\frac{5}{2}} \rightarrow 5d\ ^2D_{\frac{3}{2}}$	-	0.45[m]	4.1	I
5025.50[i]	$5p'\ ^4F_{\frac{7}{2}} \rightarrow 5d\ ^2D_{\frac{5}{2}}$	-	0.33[m]	1.5	I
5337.48[g]	$4f\ ^2F_{\frac{5}{2}} \rightarrow 5d\ ^2D_{\frac{3}{2}}$	5.4	0.93	28	I
5378.13[g]	$4f\ ^2F_{\frac{7}{2}} \rightarrow 5d\ ^2D_{\frac{5}{2}}$	5.4	1.0	40	I
6354.72[h]	$6g\ ^2G_{\frac{7}{2}} \rightarrow 4f\ ^2F_{\frac{5}{2}}$	23	0.57	84	I
6359.98[h]	$6g\ ^2G_{\frac{9}{2}} \rightarrow 4f\ ^2F_{\frac{7}{2}}$	23	0.59	120	I
6464.94	$6d\ ^2D_{\frac{3}{2}} \rightarrow 6p\ ^2P_{\frac{1}{2}}$	3.6	0.28	37	I
6725.78	$6d\ ^2D_{\frac{5}{2}} \rightarrow 6p\ ^2P_{\frac{3}{2}}$	3.8	0.34	69	I
7237.01[h]	$6f\ ^2F_{\frac{5}{2}} \rightarrow 6d\ ^2D_{\frac{3}{2}}$	24	0.31	51	I
7284.38[h]	$6f\ ^2F_{\frac{7}{2}} \rightarrow 6d\ ^2D_{\frac{5}{2}}$	25	0.34	77	I
8066.96[g]	$6p\ ^2P_{\frac{3}{2}} \rightarrow 6s\ ^2S_{\frac{1}{2}}$	13	0.65	190	I
8230.8	$8d\ ^2D_{\frac{5}{2}} \rightarrow 7p\ ^2P_{\frac{3}{2}}$	17	0.18	25	I
8530.30[j]	$6p\ ^2P_{\frac{1}{2}} \rightarrow 6s\ ^2S_{\frac{1}{2}}$	18	0.77	81	I
8877.70	$9s\ ^2S_{\frac{1}{2}} \rightarrow 7p\ P_{\frac{3}{2}}$	15	0.10	48	I
9658.75	$5g\ ^2G_{\frac{7}{2}} \rightarrow 4f\ ^2F_{\frac{5}{2}}$	-	1.0	110	I
9670.84	$5g\ ^2G_{\frac{9}{2}} \rightarrow 4f\ ^2F_{\frac{7}{2}}$	-	1.0	150	I

TABLE 4.3(b)

HELIUM-CADMIUM CHARGE TRANSFER

(7) Upper level	(8) Energy defect cm^{-1}	(9) Air wavelength Å	(10) Relative $\dot{N}/R$	(11) Average $\dot{N}/R$ less cascades	(12) Reaction rate per unit st. wt.	(13) Fractional cross-section	(14) Lifetime ratio
9p $^2P_{3/2}$	512	2365.4 2823.2	39 33	35	8.8	0.019	110 52
9p $^2P_{1/2}$	543	2367.1 2813.4	36 21	26	13	0.014	140 60
8d $^2D_{5/2}$	1,130	3417.5 8230.8	150 140	145	24	0.078	1.3 0.36
8d $^2D_{3/2}$	1,153	3343.2 3420.2	83 88	85	21	0.046	0.88 1.2
6g $^2G_{7/2}$	1,615	6354.7	150	150	19	0.081	4.3 h
6g $^2G_{9/2}$	1,615	6360.0	200	200	20	0.108	4.3 h
6f $^2F_{5/2}$	1,778	2914.7 7237.0	140 160	150	25	0.081	16 h 6.7 h
6f $^2F_{7/2}$	1,794	2929.3 7284.4	160 230	200	25	0.108	16 h 6.5 h
9s $^2S_{1/2}$	2,015	3442.4 3524.1 8877.7	520 470 480	490 - 47 = 440	220	0.119	0.80 1.1 0.30
7d $^2D_{5/2}$	6,204	4134.8	90	90 - 65 = 25	4.2	0.013	0.58
7d $^2D_{3/2}$	6,243	4029.1	59	59 - 43 = 16	4.0	0.0086	0.40
8p	no strong transitions available to detectors.						
5p' $^2F_{7/2}$	6,393	3385.5	43	43	5.4	0.023	-
5g $^2G_{7/2}$ (possibly cascade from 6h $^2H_{9/2}$)	6,996	9658.8	110	110-2 = 110	14	0.059	-

Table 4.3(b) Contd..

(7)	(8)	(9)	(10)	(11)	(12)	(13)	(14)
5g $^2G_{\frac{9}{2}}$ (possibly cascade from 6h $^2H_{11/2}$)	6,996	9670.9	150	150 - 2 = 150	15	0.081	-
5f $^2F_{\frac{5}{2}}$	7,220	3464.4	85	85 - 60 = 25	4.2	0.013	2.1
5f $^2F_{\frac{7}{2}}$	7,322	3495.4	113	113 - 83 = 30	3.8	0.016	1.8
5p′ $^2F_{\frac{5}{2}}$	8,813	3666.7	12	12	2	0.0065	-
5p′ $^4F_{\frac{5}{2}}$	15,598	4881.7	9.2	9.2	1.5	0.0050	-
5p′ $^4F_{\frac{7}{2}}$	16,029	5025.5	4.6	4.6	0.57	0.0025	-

TABLE 4.4(a)

NEON-MAGNESIUM DATA

Measured at 1.1 torr Helium + 0.1 torr Neon

(1) Air Wavelength Å	(2) Classification	(3) Upper level lifetime, ns.	(4) Branching ratio, R	(5) Relative photon Rate, $\dot{N}$
2449.59	$7f\ ^2F \rightarrow 3d\ ^2D$	22	0.49	4.4
2660.82	$6f\ ^2F \rightarrow 3d\ ^2D$	14	0.54	49
2790.78	$3d\ ^2D_{3/2} \rightarrow 3p\ ^2P_{1/2}$	2.1	0.83	85
2795.53	$3p\ ^2P_{3/2} \rightarrow 3s\ ^2S_{1/2}$	4.0	1.0	580
2798.00	$3d\ ^2D_{5/2} \rightarrow 3p\ ^2P_{3/2}$	2.1	1.0	170
2802.70	$3p\ ^2P_{1/2} \rightarrow 3s\ ^2S_{1/2}$	4.0	1.0	320
2929.0	$6p\ ^2P_{1/2} \rightarrow 3d\ ^2D_{3/2}$	-	-	20
2928.63	$4s\ ^2S_{1/2} \rightarrow 3p\ ^2P_{1/2}$	3.1	0.33	
2928.2	$6p\ ^2P_{3/2} \rightarrow 3d\ ^2D$	-	-	
2936.51	$4s\ ^2S_{1/2} \rightarrow 3p\ ^2P_{3/2}$	3.1	0.67	36
3104.8	$5f\ ^2F \rightarrow 3d\ ^2D$	8.3	0.66	30
3165.88	$7d\ ^2D_{3/2} \rightarrow 4p\ ^2P_{1/2}$	70	0.19	0.77
3168.95	$7d\ ^2D_{5/2} \rightarrow 4p\ ^2P_{3/2}$	70	0.22	1.6
3172.71	$8s\ ^2S_{1/2} \rightarrow 4p\ ^2P_{1/2}$	25	0.066	1.0
3175.78	$8s\ ^2S_{1/2} \rightarrow 4p\ ^2P_{3/2}$	25	0.13	2.1
3534.97	$6d\ ^2D_{3/2} \rightarrow 4p\ ^2P_{1/2}$	42	0.20	3.2
3538.82	$6d\ ^2D_{5/2} \rightarrow 4p\ ^2P_{3/2}$	42	0.24	8.5
3549.52	$7s\ ^2S_{1/2} \rightarrow 4p\ ^2P_{1/2}$	15	0.082	1.9
3553.37	$7s\ ^2S_{1/2} \rightarrow 4p\ ^2P_{3/2}$	15	0.16	3.8
3848.21	$5p\ ^2P_{3/2} \rightarrow 3d\ ^2D_{5/2}$	56	-	2.7
3850.39	$5p\ ^2P_{1/2} \rightarrow 3d\ ^2D_{3/2}$	56	-	1.3
4384.64	$5d\ ^2D_{3/2} \rightarrow 4p\ ^2P_{1/2}$	21	0.28	3.0

Table 4.4(a) Contd..

(1)	(2)	(3)	(4)	(5)
4390.56	5d $^2D_{\frac{3}{2}} \rightarrow$ 4p $^2P_{\frac{3}{2}}$	21	0.055	5.8
4390.56	5d $^2D_{\frac{5}{2}} \rightarrow$ 4p $^2P_{\frac{3}{2}}$	21	0.33	
4427.99	6s $^2S_{\frac{1}{2}} \rightarrow$ 4p $^2P_{\frac{1}{2}}$	9.4	0.094	0.67
4433.99	6s $^2S_{\frac{1}{2}} \rightarrow$ 4p $^2P_{\frac{3}{2}}$	9.4	0.19	1.5
4481.2	4f $^2F \rightarrow$ 3d ^2D	4.3	1.0	94
5264.3	7f $^2F \rightarrow$ 4d ^2D	22	0.49	5.4
5401.54	7g $^2G \rightarrow$ 4f ^2F	40	0.41	5.9
5434.04	7d $^2D \rightarrow$ 4f ^2F	70	0.018	0.25
5916.43	7p $^2P_{\frac{3}{2}} \rightarrow$ 4d $^2D_{\frac{5}{2}}$	187	0.14	5.1
5918.16	7p $^2P_{\frac{1}{2}} \rightarrow$ 4d $^2D_{\frac{3}{2}}$	190	0.14	2.7
6346.8	6f $^2F \rightarrow$ 4d ^2D	14	0.31	29
6545.97	6g $^2G \rightarrow$ 4f ^2F	25	0.556	40
6620.5	6d $^2D \rightarrow$ 4f ^2F	42	0.021	1.1
6781.45	7d $^2D_{\frac{3}{2}} \rightarrow$ 5p $^2P_{\frac{1}{2}}$	70	0.12	0.5
6787.85	7d $^2D_{\frac{5}{2}} \rightarrow$ 5p $^2P_{\frac{3}{2}}$	70	0.14	1.7
6812.86	8s $^2S_{\frac{1}{2}} \rightarrow$ 5p $^2P_{\frac{1}{2}}$	25	0.052	1.1
6819.27	8s $^2S_{\frac{1}{2}} \rightarrow$ 5p $^2P_{\frac{3}{2}}$	25	0.010	1.9
7877.05	4d $^2D_{\frac{3}{2}} \rightarrow$ 4p $^2P_{\frac{1}{2}}$	8.1	0.43	17
7896.37	4d $^2D_{\frac{5}{2}} \rightarrow$ 4p $^2P_{\frac{3}{2}}$	8.1	0.64	3.5
8115.22	6p $^2P_{\frac{3}{2}} \rightarrow$ 4d $^2D_{\frac{5}{2}}$	130	0.18	1.5
8120.43	6p $^2P_{\frac{1}{2}} \rightarrow$ 4d $^2D_{\frac{3}{2}}$	130	0.18	0.5
8734.99	6d $^2D_{\frac{3}{2}} \rightarrow$ 5p $^2P_{\frac{1}{2}}$	42	0.20	3.9
8745.66	6d $^2D_{\frac{5}{2}} \rightarrow$ 5p $^2P_{\frac{3}{2}}$	42	0.24	7.1

Table 4.4(a) Contd

(1)	(2)		(3)	(4)	(5)
8824.32	$7s\ ^2S_{\frac{1}{2}}$	$5p\ ^2P_{\frac{1}{2}}$	15	0.054	1.5
8835.08	$7s\ ^2S_{\frac{1}{2}}$	$5p\ ^2P_{\frac{3}{2}}$	15	0.11	2.7
9218.25	$4p\ ^2P_{\frac{3}{2}}$	$4s\ ^2S_{\frac{1}{2}}$	28	0.99	37
9244.27	$4p\ ^2P_{\frac{1}{2}}$	$4s\ ^2S_{\frac{1}{2}}$	28	0.99	18
9631.89	$5f\ ^2F_{\frac{7}{2}}$	$4d\ ^2D_{\frac{5}{2}}$	8.3	0.34	15
9632.44	$5f\ ^2F_{\frac{5}{2}}$	$4d\ ^2D_{\frac{3}{2}}$			
10092.2	$5g\ ^2G$	$4f\ ^2F$	-	1.0	35

TABLE 4.4(b)

NEON-MAGNESIUM CHARGE TRANSFER

(7) Upper level	(8) Energy defect cm^{-1}	(9) Air wavelength Å	(10) Relative $\dot{N}/R$	(11) Average $\dot{N}/R$ less cascades	(12) Reaction rate per unit st. wt.	(13) Fractional reaction rate	(14) Lifetime ratio
7g ^2G	-48	5401.5	14	14	0.80	0.044	9.3
7h ^2H	-47	no transitions available to detectors					-
7f ^2F	-39	2449.6 5264.3	9 10	9.7	0.70	0.030	10 2.7
7d $^2D_{5/2}$	65	6787.9 3169.0	13 7.1	9.8	1.6	0.031	1.7 3.7
7d $^2D_{3/2}$	65	6781.5 3165.9	4.2 4.2	4.2	1.0	0.013	1.7 3.7
7d ^2D	65	5434.0	14.0				16
8s $^2S_{1/2}$	133	3172.7 3175.8 6812.9 6819.3	9.1 9.1 12 11	10	5.0	0.031	1.3 1.3 1.7 1.7
7p $^2P_{3/2}$	2,053	5916.4	36	36	8.9	0.113	23
7p $^2P_{1/2}$	2,058	5918.2	19	19	9.3	0.060	23
6h ^2H	3,188	no transitions available to detectors					
6g ^2G	3,189	6546.0	72	72-7.0 = 65	3.6	0.20	5.8
6f ^2F	3,200	6346.8 2660.8	96 90	93-3.9 = 89	6.4	0.30	1.8 6.7
6d $^2D_{5/2}$	3,362	3538.8 8745.7	35 29	32-8 = 24	4.0	0.75	2.2 0.25
6d $^2D_{3/2}$	3,362	3535.0 6620.5 8735.0	15.9 54 19	23-6 = 17	4.3	0.053	2.2 9.7 0.25
7s $^2S_{1/2}$	3,478	3549.5 3553.4 8824.3 8835.1	22.8 23.2 28.1 25.5	24-12 = 12	6	0.038	0.79 0.79 0.27 0.27
5g ^2G	8,557	10092.2	35	Cascade from 6h & 7h		0.11	-
5f ^2F	8,572	3104.8 9632.4	46 45	45-37 = 7	-	-	4.0 0.97
5d $^2D_{3/2}$	8,841	4384.6	11	11-12.5 = -1.5	-	-	1.1
5d $^2D_{5/2}$	8,841	4390.5	18	18-15.4 = 2.6	-	-	1.1
6s $^2S_{1/2}$	9,064	4428.0 4434.0	7.2 7.8	7.5-7.8 = 0.3	-	-	0.49 0.49

TABLE 4.5(a)

HELIUM-SELENIUM DATA

measured at 0.66 torr helium

(1) Air Wavelength Å	(2) Classification	Laser Strength[1] w = weak m = medium s = strong	(5) Relative photon rate, N	(6) Character
4604.34	$5p\ ^2D_{5/2} \rightarrow 5s\ ^4P_{5/2}$	m	6.3	I 2
4648.44	$5p\ ^4P_{3/2} \rightarrow 5s\ ^4P_{1/2}$	w	8.2	I 3
4763.65	$5p\ ^2D_{3/2} \rightarrow 5s\ ^4P_{3/2}$	w	3.9	I 3
4840.63	$5p\ ^2S_{1/2} \rightarrow 5s\ ^4P_{3/2}$	w	6.2	I 3
4844.96	$5p\ ^4S \rightarrow 5s\ ^4P_{5/2}$	m	13	I 2
4975.66	$5p\ ^2D_{5/2} \rightarrow 4p^4\ ^2P_{3/2}$	s	8.5	I 2
4992.75	$5p\ ^4P_{3/2} \rightarrow 5s\ ^4P_{3/2}$	s	18	I 3
5068.65	$5p\ ^4P_{5/2} \rightarrow 5s\ ^4P_{5/2}$	s	17	I 3
5093.26	$21^0 \rightarrow 5s\ ^2D_{3/2}$	-	1.5	I 2
5096.50	$5p\ ^4D_{7/2} \rightarrow 4d\ ^4F_{9/2}$	w	2.3	I 2
5142.14	$5p\ ^4D_{3/2} \rightarrow 5s\ ^4P_{1/2}$	m	10	I 3
5175.98	$5p\ ^4D_{5/2} \rightarrow 5s\ ^4P_{3/2}$	s	34	I 3
5227.51	$5p\ ^4D_{7/2} \rightarrow 5s\ ^4P_{5/2}$	s	31	I 3
5253.07	$5p\ ^2D_{5/2} \rightarrow 5s\ ^2P_{3/2}$	m	7.2	I 2
5253.63	$5p\ ^4D_{1/2} \rightarrow 5s\ ^4P_{1/2}$	m	5.4	I 3
5271.22	$5p\ ^4D_{5/2} \rightarrow 4d\ ^4F_{7/2}$	w	2.8	I 2
5305.35	$5p\ ^2D_{3/2} \rightarrow 5s\ ^2P_{1/2}$	s	11	I 3
5522.42	$5p\ ^4P_{3/2} \rightarrow 5s\ ^4P_{5/2}$	m	3.0	I 3
5591.16	$5p\ ^4P_{3/2} \rightarrow 5s\ ^2P_{1/2}$	w	3.9	I 3
5697.88	$5p\ ^4D_{1/2} \rightarrow 5s\ ^4P_{3/2}$	w	2.8	I 3

Table 4.5(a) Contd.

(1)	(2)		(5)	(6)
5747.62	$5p\ ^4D_{\frac{5}{2}} \rightarrow 5s\ ^4P_{\frac{5}{2}}$	w	2.3	I 3
6055.96	$5p\ ^2P_{\frac{3}{2}} \rightarrow 7$	m	2.4	I 2
6444.25	$5p\ ^2D_{\frac{5}{2}} \rightarrow 7$	m	1.2	I 2
6490.48	$5p\ ^4D_{\frac{1}{2}} \rightarrow 5s\ ^2P_{\frac{1}{2}}$	m	1.6	I 3
6534.95	$5p\ ^2P_{\frac{1}{2}} \rightarrow 9$	w	1.5	I 2

TABLE 4.5(b)

HELIUM-SELENIUM CHARGE TRANSFER

(normalised to 1 torr)

(7) Upper Level	(8) Energy defect, cm^{-1}	(9) Air wavelength Å	Total observed photon rate, $\sum \dot{N}$	$\frac{\sum \dot{N}}{2J+1}$	(13) Fractional reaction rate at 1 torr
21	1,239**	5093.3	1.5	-	0.0055
$5p\,^2P^o_{3/2}$	254*	6056.0	2.4	0.60	0.0087
$5p\,^2P^o_{1/2}$	363*	6535.0	1.5	0.75	0.0055
$5p\,^2D^o_{5/2}$	1,249* - 740	4604.3 4975.7 5253.1 5271.2 6444.3	24	4.0	0.087
$5p\,^4S^o_{3/2}$	338	4845.0	13	3.2	0.047
$5p\,^4P_{5/2}$	1,249	5068.7	17 (3-body)	2.8	0.062
$5p\,^4D_{7/2}$	1,848	5227.5	47 (3-body)	5.9	0.17
$5p\,^2D^o_{3/2}$	1,907	4763.7 5305.4	21 (3-body)	5.3	0.076
$5p\,^2S_{1/2}$	2,241	4840.6	9.4 (3-body)	4.7	0.034
$5p\,^4P^o_{3/2}$	2,870	4648.4 4992.8 5522.4 5591.2	50 (3-body)	13	0.18
$5p\,^4D^o_{5/2}$	3,579	5176.0 5747.6	55 (3-body)	9.2	0.20
$5p\,^4D^o_{3/2}$	4,935	5142.1	15 (3-body)	3.8	0.055
$5p\,^4D^o_{1/2}$	5,348	5253.6 5697.9 6490.5	18 (3-body)	9.0	0.066

** From Se I $4p^4\ ^1D_2$

* From Se I $4p^4\ ^3P_1$

REFERENCES TO TABLES IN CHAPTER 4

a) Fowles, G.R., and Silfvast, W.T., IEEE J.Quant. Electron. QE-1, 131 (1965)

b) Silfvast, W.T., Fowles, G.R., and Hopkins, B.D., Appl. Phys. Lett., 8, 313 (1966)

c) Fowles, G.R., and Hopkins, B.D., IEEE J.Quant. Electron., QE-3, 419 (1967).
See also Silfvast, W.T., Appl.Phys.Lett. 13, 169 (1968)

d) Goldsborough, J.P., IEEE J.Quant. Electron., QE-5, 133 (1969)

e) Silfvast, W.T., Appl.Phys.Lett. 15, 23 (1969)

f) Jensen, R.C., Collins, G.J. and Bennett, Jr., W.R., Phys.Rev. Lett., 23, 363 (1969)

g) Karabut, E.K., Mikhalevskii, V.S., Papakin, V.F. and Sém, M.F., Sov.Phys.Tech.Phys., 14, 1447 (1970)

h) Schuebel, W.K., Appl. Phys.Lett., 16, 470 (1970)

i) Bloom, A.L. and Goldsborough, J.P., IEEE J.Quant. Electron., QE-6, 164 (1970)

j) Schuebel, W.K., IEEE J. Quant. Electron., QE-6, 655 (1970)

k) Hodges, D.T., Appl. Phys. Lett., 17, 11 (1970)

l) Silfvast, W.T., and Klein, M.B., Unpublished

m) See Section 4-4.1 and Reference 6.

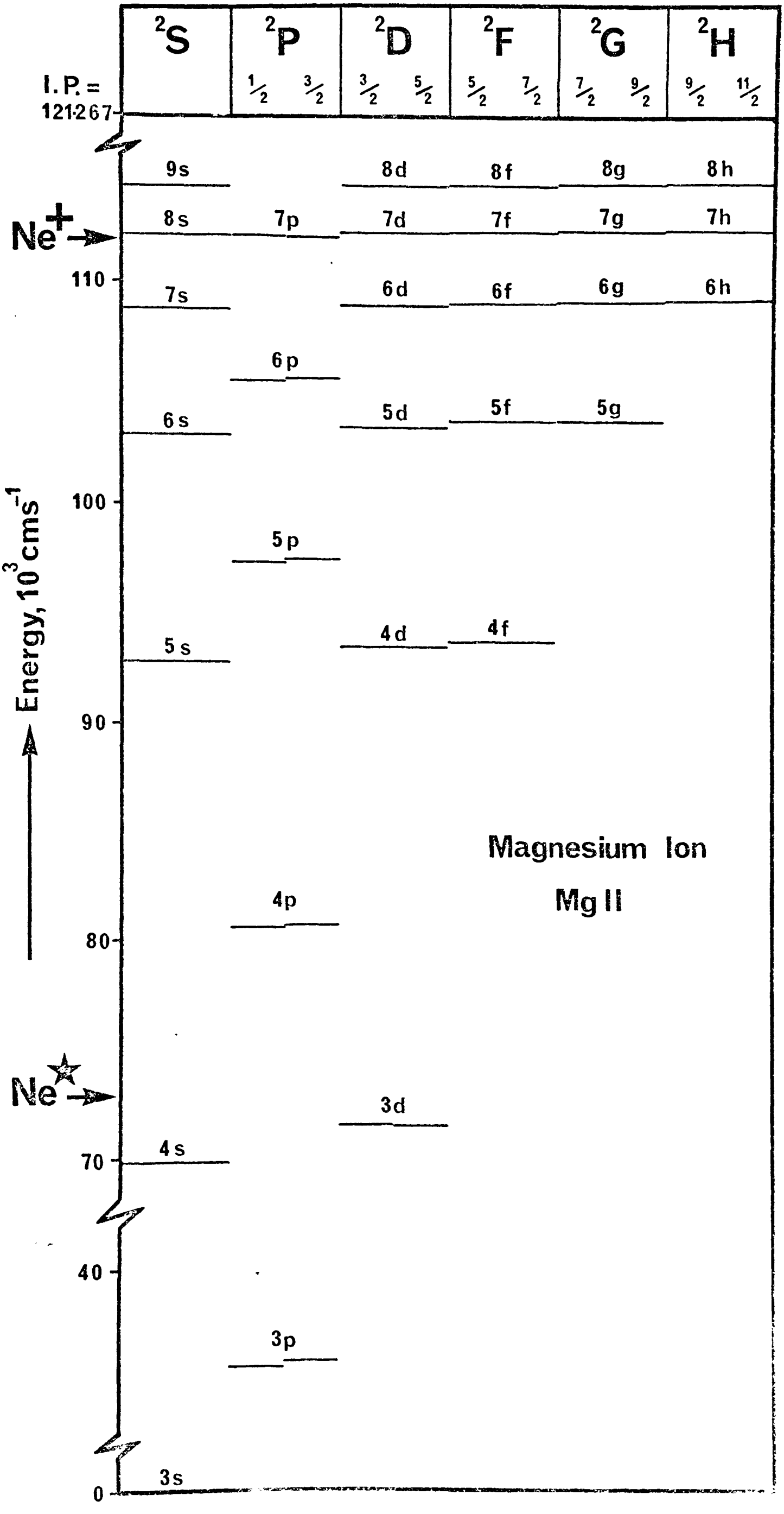

Figure 4.1 - Term Diagram of singly ionised magnesium Mg II

CHAPTER 5

THEORY OF NEAR-RESONANT LOW VELOCITY CHARGE TRANSFER A REVIEW

Ant. S: Shall I tell you why?

Dro. S: Ay, sir, and wherefore; for they say every why hath a wherefore.

Shakespeare, Comedy of Errors

KEY TO SYMBOLS used frequently in CHAPTER 5

A	Adiabatic parameter
a_0	Bohr radius
α_1, α_2	Polarizability of the neutral atom
$\delta\alpha = \lvert\alpha_1 - \alpha_2\rvert$	
b	Impact paramater
b_L	Maximum b for Langevin orbiting
b_x	Maximum b for R_x to be reached
$\Delta = I_1 - I_2$,	Energy defect at infinite separation
E_k	Relative kinetic energy at infinite separation
e	Electronic charge
$\epsilon_1(R), \epsilon_2(R)$	Eigenenergies of quasi-molecule
η	Characteristic velocity at R_x (defined by Equation (5.21))
$\gamma = \sqrt{\frac{2Ia_0}{e^2}}$	
$\hat{\tilde{H}}$	Hamiltonian operator with elements H_{11}, H_{12}, H_{21} and H_{22}
H_x	Common value of H_{11} and H_{22} at R_x
h	Plank's constant
$I = \sqrt{I_1 I_2} \approx \frac{1}{2}(I_1 + I_2)$	
I_1, I_2	$H_{11}(\infty)$, $H_{22}(\infty)$, ionisation energies of initial and final states.
μ	Reduced mass of system
P	Probability for transition between molecular states
ϕ_1, ϕ_2	Atomic wave functions
Ψ_1, Ψ_2	Molecular wave functions
R	Inter-nuclear separation
R_x	R at a crossing
R_z	R at a zone
σ	Total charge transfer cross-section
u	Radial velocity at R_x
v	Relative velocity at infinite separation
$V_1(R), V_2(R)$	Energies of ion-atom system (neglecting interaction).
$W(R)$	$H_{11} - H_{22}$
W_z	$\lvert W(R_z)\rvert$

CHAPTER 5

THEORY OF NEAR-RESONANT LOW VELOCITY CHARGE TRANSFER

A REVIEW

5-1 INTRODUCTION

Until quite recently theoretical treatment of ion-atom charge transfer interactions has been chiefly concerned with reactions at high relative velocities ($v \gtrsim 5\times10^5$ cm/sec), particular attention being paid to collisions between ions and atoms of the same element (symmetrical resonance charge transfer). This has come about for two reasons. Firstly, at higher velocities approximation methods are available (such as the Borm approximation at very high velocities, or the WKB method at intermediate velocities) which break down at low velocities, when orbits are not linear, energies are small and the exact form of the interaction potential becomes critical. Secondly the most straightforward check on the velocity-dependence of charge transfer cross-sections is made in atomic beam experiments. Such experiments do not lend themselves easily to the study of reactions at energies below 100 eV.

The present chapter outlines four principle approaches to the problem of calculating charge transfer cross-sections at low energies.

i The Adiabatic Hypothesis, which provides a semi-classical criterion for determining the velocity at the maximum cross-section which is surprisingly accurate in its predictions, but limited in its range of validity.

ii The Langevin Orbiting model, a classical orbit model which predicts the correct temperature dependence and order of magnitude of many ion-molecule reactions.

iii The Zone formulation, a quantum mechanical calculation valid in the intermediate velocity region, which has been successful in predicting the velocity behaviour of many charge transfer reactions even at lower velocities.

iv The Crossing formulation, a quantum mechanical calculation, valid at intermediate or low velocities, which can be applied to reactions involving specific excited states.

The experimental work described in this thesis leads to the evaluation of relative cross-sections in a thermal energy distribution of velocities for charge transfer to the several possible excited final states of some rare gas ion/metal atom systems. Although not giving absolute cross-sections, the experiments provide data concerning the influence on the cross-section of

a) the angular momentum of the final state
b) the participation of a third body in the reaction
c) the reduced mass of the colliding system
d) the energy defect between the initial and final states.

It is the particular concern of this chapter to discuss the predictions of the available theories with regard to these features.

5-2 SEMI-CLASSICAL THEORIES

5-2.1 The Adiabatic Hypothesis

Massey has introduced a criterion[1] which provides an estimate of the relative velocity of reactants at which the maximum charge transfer cross-section should occur. His argument runs as follows. In slow collisions, in which the relative velocity of the reactants is small compared with the velocity of the atomic electrons, these electrons will be able to adjust themselves to the changing conditions without undergoing any transition, that is, the reaction will be 'adiabatic'.

Suppose the system of two atoms can exist in two states separated in energy by Δ, then quantum theory predicts that under a purturbation of frequency $\nu = \frac{\Delta}{h}$ the system will oscillate between the states. So if the disturbance caused by the collision is characterised by some function of time $\mathcal{F}(t)$ then it is only those components of the Fourier expansions of $\mathcal{F}(t)$ at a frequency $\nu \pm \delta\nu$ which will cause a transition to take place. If the velocity of impact is v, and the region over which the transition is deemed to be possible is A, then these Fourier components will be large when $\nu \approx \frac{A}{v}$. This yields the condition for the maximum transition probability:

$$V_{max} = \frac{A\Delta}{h} \qquad (5.1)$$

which implies that when $V \ll \frac{A\Delta}{h}$ the reaction will be adiabatic. A large number of reactions obey this adiabatic maximum rule with good accuracy[2], yielding a value of $A \sim 7\text{Å}$. If the rule is applied to collisions involving helium at thermal energies it predicts that reactions such as charge transfer will have a very small cross-section when $\Delta > 10\ cm^{-1}$. The resonance condition for reactions involving heavier gases would be correspondingly more stringent.

A modification to the rule has recently been suggested by Perel and Daley[3]. They have plotted v_{max} against a parameter $\Delta I_i^{-\frac{1}{2}}$, in which I_i is the ionisation potential of the incident atom. A broad range of data fits such an empirically determined curve with remarkably little scatter, despite its non-linear behaviour at higher values of $\Delta I_i^{-\frac{1}{2}}$.

An empirical formula due to Hasted[4] and based on the adiabatic criterion, fits experimental charge transfer data reasonably well. The cross-section σ is given as

$$\sigma = B \exp\left\{ - \frac{k A|\Delta|}{h\nu} \right\}, \qquad (5.2)$$

in which B and k are constants and A is the adiabatic parameter determined empirically.

5.2-2 Langevin Orbiting

Another very simple picture of very low velocity collisions has been described by Gioumonsis and Stevenson[5]. They note that as Langevin[6] had pointed out, under an inverse fourth power law of potential, orbits fall into two classes, as illustrated in Figure 5.1. Those with an impact parameter b, less than some value b_L are closed, producing an inward spiralling orbit and impact, while those with $b > b_L$ result in a grazing encounter only. At large distances the dominant interaction between an ion and a neutral atom is likely to be polarizability-induced dipole attraction, which does indeed give such a potential:

$$V(R) = -\frac{\alpha e^2}{2R^4} ,$$

in which α is the polarizability of the neutral atom and R is the internuclear separation. Under such a potential b_L is given by

$$b_L^4 = \frac{4\alpha e^2}{\mu v^2} ,$$

in which μ is the reduced mass, which yields a cross-section for impact:

$$\sigma = \pi b_L^2 = \frac{2\pi}{v}\sqrt{\frac{\alpha e^2}{\mu}} \qquad (5.3)$$

In most circumstances it cannot be assumed that collisions lead to charge transfer with a probability of 0.5. The probability might be critically dependent on velocity so that Equation (5.3) would not be expected to give a very satisfactory value for σ. However, Langevin orbiting gives a reaction rate (proportional to $\sigma.v$) independent of velocity, and exactly such behaviour has been observed by Dunkin et al.[7] for a wide range of ion-molecule reactions. In addition the absolute reaction rates predicted by the Langevin orbiting model are close to the observed values in these reactions.

Bohme, Hasted and Ong[8] have equated Equations (5.3) and (5.2) by assuming that Equation (5.3) gives the value of the maximum cross-section σ_{max}, for some empirically determined velocity v_{max} (See Appendix 2).

This leads to the result:

$$\sigma = \sigma_{max}(v_{max}) \exp\left\{ k\left(1 - \frac{A|\Delta|}{h\nu}\right)\right\}, \qquad (5.4)$$

which they use to estimate the temperature dependence of thermal energy reaction rates for several molecular charge transfer processes. They find the most suitable parameters to be A = 100Å and k = 2 for ion-atom interchange. They suggest that this very large value of A may be due to inward spiralling of the orbits under induced dipole attraction.

5-2.3 Limitations of the Adiabatic Hypothesis

The region of applicability of the adiabatic hypothesis is strictly limited. Implicit among its assumptions is that Δ is a constant, independent of inter-nuclear distance. In general, however, this will not be so and the energies $V_1(R)$ and $V_2(R)$ of the two possible states of the system may be functions of the inter-nuclear separation and diverge or converge with decreasing R (See Figure (5.2), so that $|V_1 - V_2|$ may pass through zero, or become very small over some region of R at R_x.

It does not follow, therefore, that two different atoms having a very close energy coincidence of ground ionic and excited atomic states, when infinitely separated, will necessarily have an interaction cross-section increasing monatonically as their impact velocity decreases. Nor, consequently, does the adiabatic criterion impose such stringent limits on the size of $\Delta = V_1(\infty) - V_2(\infty)$ as might at first be expected. This dependence of $|V_1 - V_2|$ on R will be particularly marked in the case with which we are concerned, that of charge transfer between a rare gas ion and a metal atom, for in this case the polarization in the initial state of the metallic atom induced by the ion will invariably

be much larger than that induced in the neutral rare gas atom of the final state by the excited metal ion.

5-3 QUANTUM MECHANICAL THEORIES

5-3.1 Starting Equations

A rigorous treatment of charge transfer requires the solution of the wave equation

$$i\hbar \frac{\partial \underset{\sim}{\Psi}}{\partial t} = \underset{\sim}{\hat{H}} . \underset{\sim}{\Psi} \; , \qquad (5.5)$$

in which $\underset{\sim}{\Psi}_i$ are the molecular wave functions of the total system. Three initial assumptions are necessary

i the translational motion of the electron can be ignored,

ii the transfer may be treated as a one electron problem involving two states only, and

iii the molecular wave functions may be written as a linear combination of atomic orbitals.

Assumption i) allows the problem to be written in terms of electronic wave functions alone. Assumption ii) says that only two (orthogonal) molecular electronic wave functions are involved, $\underset{\sim}{\Psi}_1$ and $\underset{\sim}{\Psi}_2$. Assumption iii), however, enables the molecular wave functions $\underset{\sim}{\Psi}_1$, and $\underset{\sim}{\Psi}_2$ to be written in terms of atomic wave functions ϕ_1 and ϕ_2. The two possible states of the molecular system may therefore be represented by

$$\underset{\sim}{\Psi}_i = a_1(R)\,\phi_1 + a_2(R)\,\phi_2 \; , \qquad (5.6)$$

in which the coefficients a_1 and a_2 can each take on one of two values, corresponding to $\underset{\sim}{\Psi}_1$ and $\underset{\sim}{\Psi}_2$ and $|a_1|^2$ and $|a_2|^2$ are the probabilities that the electron will be near atom A or near atom B in the definite atomic states ϕ_1 and ϕ_2. The values of a_1 and a_2 are found by substituting Equation (5.6) into (5.5), multiplying by ϕ_1 and ϕ_2 and integrating, giving the simultaneous equations

$$i\hbar\dot{a}_1 = H_{11}a_1 + H_{12}a_2 ,$$
$$i\hbar\dot{a}_2 = H_{21}a_1 + H_{22}a_2 , \qquad (5.7)$$

in which H_{11} and H_{22}, equivalent to V_1 and V_2 used in Section 5-2, are the energies of the two possible states of the system ϕ_1 and ϕ_2. Obviously $|a_1|^2 + |a_2|^2 = 1$ so H_{12} must be Hermitian and we can write $H_{21} = H_{12}$.

It is more convenient to consider the system to vary with time rather than with internuclear distance. However, although ϕ_1 and ϕ_2 are not steady states neither are they functions of time. It is therefore necessary to introduce new variables $c_1(t)$ and $c_2(t)$ so that Equation (5.6) may be written

$$\Psi_i = c_1(t)\,\phi_1 \exp\left\{-\frac{iH_{11}t}{\hbar}\right\} + c_2(t)\,\phi_2 \exp\left\{-\frac{iH_{22}t}{\hbar}\right\}. \qquad (5.8)$$

Now the wave functions Ψ_1 and Ψ_2 describe two stationary orthogonal states of the total system, the "quasi-molecule", the energies ϵ_1 and ϵ_2 of which might be as shown in Figure 5.3. The crossing in Figure 5.2 occurred only because the possibility of charge transfer had been ignored. The energies of the true molecular states will approach each other with a minimum separation of order H_{12}, so that if the atoms approach each other infinitely slowly no transfer would take place.

The coefficients c_1 and c_2 are solutions of the equations

$$(H_{11} - \epsilon)c_1 + H_{22}c_2 = 0 ,$$
$$H_{12}c_1 + (H_{22} - \epsilon)c_2 = 0 , \qquad (5.9)$$

in which ϵ assumes the values of the eigenenergies of the possible stationary states of the quasi-molecule. The solution depends on knowledge of H_{11}, H_{22} and H_{12} and it is in the choice of these that the various approximations and models employed differ.

When W(R) is defined by $W(R) = H_{11} - H_{22}$ then when $|H_{12}| \ll |W|$ then $c_1 \approx 1$, $c_2 \approx 0$ and $\epsilon_1 \approx H_{11}$, or $c \simeq 0$, $c \approx 1$ and $\epsilon_2 \approx H$, that is, the molecular wave function is well approximated by one of the atomic wave functions ϕ_1 or ϕ_2, and a transition will not take place. If, however, $|H_{12}| \gg |W|$ then $\epsilon_{1,2} \approx (H_{11} + H_{22}) \pm |H_{12}|$ and $c_1 = \pm \frac{1}{\sqrt{2}} = \mp c_2$. In this case the two molecular states are described by a combination of the strongly interacting atomic states ϕ_1 and ϕ_2. The condition for strong interaction can be written

$$2\,|H_{12}(R)| \geqslant |W(R)| \qquad (5.10)$$

Two possible approaches to the solution are currently in use. The first assumes there is no actual crossing of the potentials (in the classical sense), but that nevertheless there is a fairly extended "critical region" over which a strong interaction, as defined by Equation (5.10) can occur. This will be termed the "zone formulation". The second approach assumes a crossing or rather a pseudo-crossing, does occur and that a critical region, as defined by Equation (5.10) exists only over a very small distance about R_x. This approach will be termed the "crossing formulation".

5-3.2 Zone Formulation - Stueckelberg Method

The initial calculations, under the first approach, when an extended critical region is deemed to exist about some $R=R_z$, were carried out by Stueckelberg[9]. He showed that when in the critical region $H_{12}(R)$ could be expressed in the form

$$H_{12}(R) = -\frac{C_s}{R^s},$$

then

$$\sigma = \pi \left(\frac{C_s}{W_z}\right)^{\frac{2}{s}} F\left(\frac{W_z^{1-\frac{1}{s}} C_s^{\frac{1}{s}}}{\hbar v}\right), \qquad (5.11)$$

in which $W_z = |W(R_z)|$ is the constant difference in the atomic potentials and

$$F(x) = 8 M_s \frac{x}{s} \quad , \quad x \ll 1,$$

$$F(x) = 32 N_s x^{s-1} e^{-2x} \quad , \quad x \gg 1,$$

with M_s and N_s constants of order unity depending on s . This formula is illustrated in Table 5.1 for the case of s = 3 and s = 4.

The gross failure of Stueckelberg's equations to predict satisfactory results for excitation transfer cross-sections[10] has led to doubt about their general usefulness. But this failure, which is due to the sensitivity to detailed features of H_{11}, H_{22} and H_{12}, should not invalidate their use in the case of low velocity collisions under ion-atom attractive forces, for in this case H_{11}, H_{22} and H_{12} may be fairly accurately defined. The most satisfactory models for H_{12}, however, are exponential in R rather than simple polynomials.

5-3.3 Zone Formulation - Demkov Method

Demkov[11], in his derivation of a transfer probability, P, postulates an interaction energy H_{12} expressed as an exponential decay with respect to time in a region about R_z. His analysis leads to the result

$$P = \operatorname{sech}^2\left\{\frac{\pi}{2} \frac{W_z}{\gamma u} \frac{a_c}{\hbar}\right\} \sin^2\left\{\frac{1}{\hbar}\int_{-\infty}^{\infty} H_{12}\, dt\right\}, \qquad (5.12)$$

in which $\gamma^2 = \frac{2I a_c}{e^2}$ with I the average ionisation potential of the particular states of the reactants involved. The value of $u = \left|\frac{\partial R}{\partial t}\right|_{R_z}$ may be obtained from geometrical considerations concerning the impact parameter, and by assuming a rectilinear orbit. When this is done, and at low velocity the $\sin^2$ term is replaced by its average value, $\frac{1}{2}$, an asymptotic value for the cross-section may be calculated:

$$\sigma = 4 \frac{\gamma \hbar}{a_c} R_z^2 \frac{v}{W_z} \exp\left\{-\frac{\pi a_c}{\gamma \hbar} \frac{W_z}{v}\right\}. \qquad (5.13)$$

Demkov points out, however, that the real difficulty in this case is the problem of deciding the constant value of W_z in the critical region. If polarisation attraction is ignored then $W_z = |\Delta|$ might be taken as a suitable value. This however is seldom justified and if polarisation attraction is admitted a suitable value of W_z would be given by

$$W_z = \left| \Delta - \frac{(\alpha_1 - \alpha_2) e^2}{R_z^2} \right| = \left| H_{12}(R_z) \right| \qquad (5.14)$$

in which $\Delta = H_{11}(\infty) - H_{22}(\infty) = I_1 - I_2$.

5-3.4 Zone Formulation - Rapp and Francis Method

The calculations of Rapp and Francis[12], as another particular case of the critical region approach, have, despite the comments in the previous section, proved most successful in describing the velocity and energy defect dependence of many collisions investigated in atomic beam and drift tube experiments[13, 14, 15, 16]. For these calculations it has seemed sufficient to take $W_z = |\Delta|$, ignoring the polarization forces, which cancel to a greater or lesser extent ($\alpha_1 \approx \alpha_2$) in most of the experimental systems to which the theory has been applied.

In their calculation Rapp and Francis follow a procedure due to Dalgarno[17] and similar to that of Demkov, but adopting the semi-empirical one-electron wave function due to Popescu Iovitsu and Ionescu-Pallas[18]:

$$\Psi_i(R) = \left(\pi a_0^3\right)^{-\frac{1}{2}} \gamma^{\frac{3}{2}} \exp\left\{ - \gamma \frac{R}{a_0} \right\} , \qquad (5.14)$$

which roughly correlates the size of an orbital with its ionization energy. When $R \gg a_0$ this wave function leads to an interaction energy

$$H_{12} = \frac{\gamma R}{a_0} \exp\left\{ - \gamma \frac{R}{a_0} \right\} . \qquad (5.15)$$

From this wave function they calculate a charge transfer probability:

$$P = f \operatorname{sech}^2\left\{ \frac{a_0}{h} \sqrt{\frac{\pi b}{\gamma a_0}} \frac{W_z}{v} \right\} P_{sym}(b, v) , \qquad (5.16)$$

in which f is a statistical weight factor and

$$P_{sym}(b,v) = \sin^2\left\{\left(\frac{2\pi}{\gamma a_0}\right)^{\frac{1}{2}}\left(\frac{I}{\hbar v}\right)b^{\frac{3}{2}}\left(1+\frac{a_0}{\gamma b}\right)\exp\left[-\frac{\gamma b}{a_0}\right]\right\} \quad (5.17)$$

$$= \sin^2 D(b,v),$$

is the probability associated with symmetrical charge transfer, which is a function of the impact velocity v and the impact parameter b. The similarity between Equation (5.12) and Equation (5.16) is obvious.

Once more $\sin^2 D$ is taken to be $\frac{1}{2}$, this time over a region between $b = 0$ and b_1 given by the solution of $D(b_1, v) = \pi/6$, where Psym = $\frac{1}{4}$. At high velocities the sech^2 function is approximately unity, enabling the charge transfer cross-section to be expressed in the form for symmetrical charge transfer

$$\sigma^{\frac{1}{2}} = k_1 - k_2 \ln v$$

in which k_1 and k_2 are almost constant. At lower velocities the cross-section falls until it reaches the approximate asymptotic value, given by setting the maximum impact parameter equal to infinity:

$$\sigma \simeq \frac{9(1.202)}{\pi}\,\frac{\gamma^2 v^4 \hbar^4}{a_0^2 W_\Sigma^4} \quad (5.18)$$

These results are illustrated for the case of helium in Figure 5.4.

Lee and Hasted[19] have produced tables enabling the Rapp and Francis cross-sections to be calculated easily. They have also derived an expression for v_{max} at which σ is at a maximum which does not depend on an empirical adiabatic parameter.

Recent work by Storm and Rapp[20] has confirmed the general outline of these results, despite the crude assumptions made in the original work. In particular they have been able to show that asymmetrical charge transfer does behave like symmetrical charge transfer at velocities greater than v_{max}.

5-3.5 Curve Crossing Formulation - The Stueckelberg-Landau-Zener (SLZ) Formula

In the previous section it was assumed that while W(R) remained constant over a region, H_{12} varied rapidly. Calculation proceeded by proposing a suitable form for $H_{12}(R)$ and integrating over the region. In this section we wili consider the formula derived independently by Stueckelberg[6], Landau[21] and Zener[22]. The formulation is based on a curve crossing model in which the opposite view is taken in that in a narrow region about the crossing H_{12} (R) remains constant, while W(R), which to first order has a linear dependence on R, is changing rapidly.

The solution to the wave equation under the condition of a pseudo-crossing follows the previous argument as far as Equation(5.9). At this point two further assumptions are added to the first three:

iv the energy of relative motion at the crossing is much greater than $(\epsilon_1 - \epsilon_2)_R \approx W(R_x)$,*

v transitions only occur in a very narrow region around the crossing, so that we can expand H_{11} and H_{22} as a series of powers of $Z = R - R_x$, writing in the first order approximation

$$H_{11} = H_x + H'_{11}(R_x).R \,,$$
$$H_{22} = H_x + H'_{22}(R_x)\,R \,, \qquad (5.19)$$

where H_x is the common value of H_{11} and H_{22} at R_x and the primes refer to differentiation with respect to R.

Changing the differentiation in Equation (5.7) to one with respect to Z such that $\frac{d}{dt} = u\frac{d}{dZ}$, where $u = \left|\frac{\partial R}{\partial t}\right|_{R_x}$ is the radial velocity, and using the variables c_1 and c_2 Equation (5.7) may be written:

$$i\hbar u \frac{dc_1}{dZ} = H'_{11}(R_x) Z c_1 + H_{21}(R_x) c_2 \,, \qquad (5.20)$$
$$i\hbar u \frac{dc_2}{dZ} = H_{12}(R_x) c_1 + H'_{22}(R_x) Z c_2 \,.$$

---

*The results have, however, been shown[23] to remain unaffected by the occurrance of the turning point of the orbit close to the crossing point.

If Equation (5.20) is solved with the boundary conditions $c_1=1$, $c_2=0$ and $Z\to\infty$ then $|c_1(-\infty)|^2$ determines the probability that as the nuclei pass through the crossing the quasi-molecule remains in the electronic state ϕ_1, indicating a transition between the two molecular states shown in Figure 5.2:

$$P = |c_1(-\infty)|^2 .$$

In general, however, a collision involves a double passage through the crossing, so that charge transfer may take place either while the nuclei are approaching, or while they are receding, or both. The total charge transfer probability is then 2P(1-P).

Equations (5.20) have been solved by Zener[21] and others[6,20] by Laplace's method to give the result

$$P_\ell = e^{-\frac{\eta}{u}}$$

in which

$$\eta = \frac{2\pi |H_{12}(R_x)|^2}{\hbar |H_{11}' - H_{22}'|_{R_x}} \qquad (5.21)$$

is a characteristic velocity and u is the radial velocity at the crossing given by:

$$u = \frac{1}{\mu}\left[k^2 + \frac{2\mu(I_1 - H_{xx})}{\hbar^2} - \frac{\ell(\ell+1)}{R_x^2} \right]^{\frac{1}{2}} \qquad (5.22)$$

In this equation $I_1=H_{11}(\infty)$ is the energy of the initial state at infinite nuclear separation (this energy does not include the kinetic energy of relative motion, $E_k=\frac{1}{2}\mu v^2$), $k\hbar$ is the relative linear momentum and $\sqrt{\ell(\ell+1)}\,\hbar$ is the relative angular momentum of the two atoms. The behaviour of the total transfer probability 2P(1-P) is shown in Figure 5.5 as a function of u/η. This figure shows the total transfer probability rising to a maximum of 0.5 when P =0.5 at each crossing. Beyond this point, when P>0.5, the total probability drops again corresponding to a likelihood that a transfer will take place first forward, then backward as the reactants travel through the crossing twice.

Associated with the angular momentum $\sqrt{\ell(\ell+1)}\,\hbar$ is a classical cross-section $\frac{(2\ell+1)\pi}{k^2}$. The total cross-section is therefore

$$\sigma = \frac{2\pi}{k^2} \sum (2\ell+1) P(1-P).$$

The summation has to be taken over all ℓ for which u given by Equation (5.22) is real. The value ℓ_{max} for which u vanishes is large for all low velocity collisions so that the cross-section may be written:

$$\sigma = \frac{2\pi}{k^2} \int_0^{\ell_{max}} 2P(1-P)\,\ell\,d\ell. \qquad (5.23)$$

If we assume a linear trajectory Equation (5.23) may be written more conveniently in terms of the classical impact parameter $b = \frac{(\ell+\frac{1}{2})\hbar}{k}$:

$$\sigma = \pi R_x^2 \int_0^{R_x} 2P(1-P)\,b\,db \qquad (5.24)$$

with $$u^2 = \frac{2}{\mu}\left[I_1 - H_x + \left(1 - \frac{b^2}{R_x^2}\right) E_k \right].$$

Unfortunately the integrals in these expressions cannot be performed analytically. The results in any case depend rather critically on the values of H_{11}, H_{22}, H_{12}, H_x, I_1 and E_k and so each collision has to be treated individually. The cross-section can be reduced further to a tabulated integral, however, by writing

$$\sigma = 4\pi^2 R_x^2 \left(1 - \frac{H_x}{I+E_k}\right) \int_1^{\infty} e^{-\eta x}\left(1 - e^{-\eta}\right) x^{-3}\,dx.$$

Bates[24], in his critical examination of the approximations made in the derivation of these formulae, proposed a strong restriction on the validity of the formulae at higher velocities. This objection has been modified to some extent by Heinriches[25], who has demonstrated a procedure to be adopted to estimate higher order effects. Other features of experimental results, such as oscillations of the total charge transfer cross-section with impact velocity, have also been successfully explained by the SLZ formulation[26,27].

The neglect of the time derivative of the wave functions at the crossing, however, has serious consequences when non-spherically symmetric states are involved in a crossing.[28] A formulation for non-s states has not been made, but it is not too difficult to see how the results would be affected qualitatively. Figure (5.6) illustrates the case for an s state crossing a p state, showing the energy levels associated with each molecular state. The alignment of the angular momentum vector with respect to the inter-nuclear axis splits the p atomic state into two parts; that associated with the $p_{\pm 1}$ molecular state ($\hat{\underset{\sim}{L}}$ parallel to $\hat{\underset{\sim}{R}}$) and that associated with the p_o molecular state ($\hat{\underset{\sim}{L}}$ perpendicular to $\hat{\underset{\sim}{R}}$). It can be seen from the diagram that although the collision may be sufficiently slow that a transition from curve 1 to curve 2 is unlikely, nevertheless because of the strong coupling between the $p_{\pm 1}$ and p_o levels there may well still be a transition from curve 1 to curve 3. It may well be that at low velocities, therefore, the formulae may seriously under-estimate the probability of transition between levels of differing angular momentum. This is significant to the results presented in this thesis in that the majority of reactions studied were charge transfer from $He^+(^2S_{\frac{1}{2}})$ to a state of non-zero angular momentum.

5-3.6 SLZ Formula - Applications

An advantage of the SLZ formula is that it does not make any assumptions about the orbit of the colliding partners. As an example of the application of the formula a method due to Smith and Olson[29] is presented. Unlike most calculations, this takes full account of the limits to orbits under the forces of attraction normally encountered. Smith and Olson employ a potential of the form

$$H_{ii} = I_i - \frac{\alpha_i e^2}{2R^4} - \frac{\beta_i e^2}{R^3} \qquad (5.25)$$

in which α_i and β_i are the dipole polarizability and quadrupole susceptability respectively of the neutral atom. This is a very simplified model for H_{ii} as it includes no repulsion term, but it has the advantage that the effect of attraction is taken into account. This is accomplished by suitable choice of the upper limit to the integral in Equation (5.24) and by writing this equation in the form

$$\sigma = 4\pi b_x^2 \int_0^{\beta} P(1-P)\left(\frac{b}{b_x}\right) d\left(\frac{b}{b_x}\right) , \qquad (5.26)$$

in which b_x is the maximum impact parameter just allowing the crossing R_x to be reached:

$$b_x^2 = R_x^2 \frac{(I_i - H_x + E_k)}{E_k} \qquad (5.27)$$

In the case of a rare gas ion and a metal atom the quadrupole interaction term may generally be ignored, also $\alpha_2 \approx 0$ and $\delta\alpha = \alpha_1 - \alpha_2 \simeq \alpha_1$. This is the case when one of the atomic eigenenergies is constant from $R = \infty$ to $R < R_x$, which is illustrated in Figure (5.7). This approximation simplifies the expressions for the limits to orbiting (Appendix 2.) and reduces Equation (5.27) to

$$b_x^2 = R_x^2 \frac{(\Delta + E_k)}{E_k} \qquad (5.28)$$

in which R_x is given by Equation (5.25) with $I_1 - H_x = \Delta$.

In Equation (5.26) β is an upper limit on b/b_x determined under different conditions by either

a) the angular momentum limitation in which case $\beta = 1$, or

b) the possible existence of a 'centrifugal barrier' outside R_x.

The barrier occurs at the value of R at which the energy involved in the tangential motion of the orbiting partners (which is governed by

conservation of angular momentum) is equal to the energy gained as the atoms move closer under mutual attraction. In Appendix 2 it is shown that this barrier determines the value of β under the conditions where Equation (5.27) is valid, provided that $\Delta > E_k$, which is nearly always the case in the reactions studied in this thesis. When $\Delta > E_k$, β is given by

$$\beta^2 = \frac{2\sqrt{E_k \Delta}}{(\Delta + E_k)} .$$

Although the cross-section cannot be expressed in terms of a simple analytical expression, numerical solution of Equation (5.26) is straightforward. Smith and Olson have expressed the integral in Equation (5.26) in the form of the graph reproduced in Figure 5.8 When the atomic eigenenergies are of the form shown in Figure 5.7, the quantity g of Figure 5.8 is defined as

$$g = \eta \left[\frac{2}{\mu} (E_k + \Delta) \right]^{-\frac{1}{2}} \qquad (5.29)$$

Actual values calculated using this method depend critically on the choice of H_{12}. However, Bauer, Olson & Smith[30] have analysed a wide range of experimental and theoretical data which they find on the basis of the SLZ formulae predict within a factor 3 an interaction energy very similar to that used by Rapp and Francis:

$$H_{12} = 0.662 \frac{I R_x}{e^2} \exp\left\{ -0.429 \gamma \frac{R_x}{a_c} \right\} \qquad (5.30)$$

5-4 DISCUSSION

5-4.1 Regions of Application

The zone formulation and the crossing formulation do not describe different physical events, but rather represent two solutions to one problem, strictly applicable only to two limiting cases.

The zone formulation is applied when the critical region is extended, so that the quasi-molecule has time to oscillate between the states ϕ_1 and ϕ_2 as the atoms approach one another. This situation will occur in the case when $\delta\alpha$ is small, so that H_{11} and H_{22} follow each other closely over an extended region from $R = \infty$ to $R < R_z$. The study of reactions such as[14]:

$$I^+(^3P_2) + Hg(^1S_0) \longrightarrow I(^2P_{\frac{1}{2}}) + Hg^+(^2S_{\frac{1}{2}}) + 0.019\,eV,$$

which has verified the zone formulation, represents such a case. In addition, because Δ is so small R_z will lie well outside the centrifugal barrier, so that the assumption of a rectilinear orbit is justified (see Appendix 2, which shows that for small Δ most orbits leading to an interaction are open, corresponding to $b > b_L$ in Figure 5.1).

The effect of non-linear orbits on the zone formulation will be to increase the cross-section when Δ is comparable with or greater than E_k. Orbiting behaviour is only easily described by the Langevin orbiting model, which is just the limit of the zone formulation when orbiting dominates. This corresponds to the collision partners orbiting closer to each other until the critical zone is reached. On leaving the zone again (the inward spiralling having been reversed when the repulsive terms in the interaction become important) the probability that a transition has taken place is 0.5.

In Appendix 3 it is shown that in the cases of interest in this thesis it is unlikely that a critical zone does exist, so that the most suitable formulation is the curve-crossing model. This formulation is applied when the critical region is traversed so fast that the

$\sin^2$ term in Equation (5.12) has insufficient time to oscillate. This will be the case when $H_{,2}$ is small, corresponding to crossings occurring at large values of R and when $\delta\alpha$ is not small.

However, before an application of these ideas can be made, it should be noted that in all the calculations except the orbiting model the interaction of just two states has been considered. One might expect that at an inner critical region alternative final states with roughly the same energy defect would be populated proportionally to their statistical weight, but the problem of crossings is much more severe. Each state will cross neighbouring states at a different R_x, and, as has been shown, the particular quantum numbers involved will play an important but quantitatively uncertain role in determining the transition probability. Nor will the forces causing the crossings themselves be limited to dipole polarizability and quadrupole susceptability. The orientation of the angular momentum to the inter-nuclear axis will play a major role, and in addition l-s and even s-s coupling may cause the most complicated inter-mixing of energy levels as the atoms move from a free state to a quasi-molecular state[31, 32]. It is by no means clear, therefore, what the probability for a transition to one particular final state will be if there are several possible final states available to the charge transfer reaction.

5-4.2 Conclusions

Of the four features of charge transfer cross-sections mentioned in Section 5-1, which are open to analysis by the experimental methods described in this thesis, it has been shown that at the present stage of development the theories presented cannot evaluate the influence on the cross-section of either a) the angular momentum of the final state, or b) the participation of a third body in the reaction. The influence of c), the reduced mass of the system, is illustrated in Table 5.1 for the case of constant E_k. For

each model discussed, with the exception of the SLZ formula, the reaction rate (proportional to $\sigma/\sqrt{\mu}$ when E_k is constant) decreases to a greater or lesser extent as the reduced mass is increased. The influence of d), the energy defect, is also shown in Table 5.1 in which W_z appears in place of Δ in the zone formulae. The relation of W_z and Δ is given by Equation (5.14) and depends on the location of the zone of interaction. It can readily be seen that if Δ is zero, W(R) increases monotonically with decreasing R. A minimum value of W_z will occur when Δ has a small positive value.

With the exception of the Langevin orbiting model, which is independent of energy defect, and the empirical model due to Hasted, which strictly should be expressed in terms of W_z rather than Δ, all the models presented indicate that a small, positive energy defect will enhance the cross-section. This is quite unlike the reaction between neutral atoms, in which the energy defect must be very small for excitation transfer to take place.

The physical interpretation is that when $\Delta \rightarrow 0$ the critical region will occur at a very large value of R, where the overlap of the atomic wave functions is small. In these circumstances the target presented to the collision partners is large, but very "transparent". Increasing Δ will bring the critical region to smaller R where the overlap is much larger so that the target presented will be smaller, but much more "opaque" so that the total cross-section will be larger. As the transition probability approaches 0.5 a further increase in Δ will reduce the cross-section by reducing the size of the target. In the crossing formulation, in which the target can be thought of as a shell of non-zero transition probability, increasing Δ beyond the point where (1-P)=0.5 also decreases the opacity of the target because the shell is crossed twice.

5-4.3 A Numerical Example

In the case of a rare gas ion and a metal atom it is reasonable to assume i) $\beta \simeq 0$ ii) $\alpha_1 \simeq \delta\alpha$. When using the SLZ formula it is possible to make a rough estimate of the behaviour of the cross-section with energy defect by assuming further that iii) $\Delta \gg E_k$ and iv) the probability for charge transfer between atomic states (1-P) is small. Under the conditions specified Equation (5.26) may be approximated by

$$\sigma = 4\pi b_{max}^2 (1-P) \qquad (5.31)$$

in which $$1-P = 1 - e^{-\eta/u}$$

$$\simeq \eta/u .$$

By using Equation (5.30) to provide a semi-empirical value for η the cross-section for a given system can be expressed as a proportionality in terms of Δ only:

$$\sigma \propto \Delta^{-\frac{9}{4}} \exp\left\{-0.858 \frac{\gamma}{a_0}\left(\frac{\delta\alpha\, e^2}{2\Delta}\right)^{\frac{1}{4}}\right\} \qquad (5.32)$$

It is easy to show that this expression has a maximum value when the exponent takes on the value 9. In terms of I and $\delta\alpha$, expressed in arbitary units, the maximum cross-section occurs when Δ is given by

$$\Delta_{max} = 1.65 \times 10^{-4} \frac{I^2 \delta\alpha}{e^2 a_c^2} \qquad (5.33)$$

The values of Δ_{max} calculated from Equation (5.33) for reactions involving charge transfer between helium, neon and argon ions and zinc, cadmium and magnesium are given in Table 5.2, in which the values of α are taken from Refs. 33 and 34.

The general shape of the σ v. Δ curve given in Equation (5.32) is illustrated in Figure 5.9. which is calculated for the helium-cadmium reaction. Although the curve represents a very crude approximation, valid only for s states, it serves to illustrate the general features of all charge transfer reactions between rare

gas ions and metal atoms:

i a positive energy defect will enhance the cross-section, and

ii in most cases the cross-section is not critically dependent on the energy defect.

REFERENCES - CHAPTER 5

1 Massey, H.S.W., Rep.Prog.Phys., 12, 248 (1949)

2 Hasted, J.B., Adv. Electronics & Electron Physics, 13, 1 (1960)

3 Perel, J., and Daley, H.L., to be published (Phys.Rev)

4 Hasted, J.B., J. Appl. Phys. 30, 25, (1959)

5 Gioumousis, G., and Stevenson, D.P., J. Chem.Phys. 29, 294, (1958)

6 Langevin, P., Ann. Chim.Phys. 5, 245 (1905)

7 Dunkin, D.B., Fehsenfeld, F.C., Schmeltekopf, A.L. and Ferguson, E.E., J. Chem.Phys. 49, 1365 (1968)

8 Bohme, D.K., Hasted, J.B., and Ong, P.P., J.Phys.B 1, 879 (1968)

9 Stueckelberg E.C.G., Helv.Phys.Acta 5, 370 (1932)

10 Gallagher, A., Phys.Rev. 179, 105 (1969)

11 Demkov, Ju.N., Sov.Phys. JETP, 18, 138 (1964)

12 Rapp, D. and Francis, W.E., J.Chem.Phys. 37, 2631 (1962)

13 Peterson, J.R. and Lorents, D.C., Phys.Rev. 182, 152 (1969)

14 Perel, J., Vernon, R.H. and Daley, H.L., Phys.Rev. 138A, 937 (1965)

15 Edmonds, P.H., and Hasted, J.B., Proc.Phys.Soc. 84, 99 (1964)

16 Kaneko, V., Megill, L.R., and Hasted, J.B., J.Chem.Phys. 45, 3741 (1966)

17 Dalgarno, A., Phil.Trans.Roy.Soc., A72, 674 (1958)
See also Gurnee, E.F. and Magee, J.L., J.Chem.Phys. 26, 511 (1957)

18 Popescu Iovitsu, I., and Ionescu-Pallas, N., Sov.Phys.Tech. 4, 781 (1960)

19 Lee, A.R., and Hasted, J.B., Proc.Phys.Soc. 85, 673 (1965)

20 Storm, D., and Rapp, D., J.Chem.Phys. 53, 1333 (1970)

21 Landau, L., Phys.Z. Sowjet, 2, 46 (1932)

22 Zener, C., Proc.Roy.Soc. A137, 696 (1932)

23 Bykhovskii, V.K., Nikitin, E.E. and Ovchinnikova, M. Ya., Sov.Phys. JETP 20, 500 (1965)

24 Bates, D.R., Proc.Roy.Soc. A 257, 22 (1960)
See also Nikitin, E.E., Comments At.Mol.Phys. 1, 166 (1969)

25 Heinrichs, J. Phys.Rev. 176, 141 (1968)

26 Olson, R.E., Phys.Rev. A2, 121 (1970)

27 Rosenthal, H., and Foley, H.M., Phys. Rev. Let. 23, 1480 (1969)

28 Bates, D.R., 'Atomic and Molecular Processes', Ed. Bates., New York: Academic Press.

29 Smith, F.T., and Olson, R.E., private communication

30 Bauer, E., Olson, R.E. and Smith, F.T., private communication

31 Dasherskaya, E.I., Voronin, A.I., and Nikitin, .E.E., Can.J.Phys. 47, 1237 (1969)

32 Lichten, W., Phys.Rev. 164, 131 (1967)

33 Shabanova, L.N., Opt.Spec. 27, 205 (1969)

34 Rothe, E.W., and Bernstein, R.B., J.Chem.Phys. 31, 1619 (1959)

TABLE 5.1

Summary of charge transfer theories at low velocity

Theory	Interaction Energy H_{12}	Cross-section	Dependence on μ (E_k constant, C arbitary constant)	Dependence on Δ ($\Delta > E_k$, C arbitary constant)
Hasted empirical (Adiabatic hypothesis)	–	$B \exp\left\{-\frac{k A \Delta}{h v}\right\}$	$e^{-\sqrt{\mu} k}$	$e^{-\Delta}$
Langevin orbiting	–	$\frac{2\pi}{v}\sqrt{\frac{\alpha e^2}{\mu}} = 2\pi\sqrt{\frac{\alpha e^2}{2E_k}}$	1	1
Stueckelberg C_3	$\frac{C_3}{R^3}$	$\frac{32\pi N_3 C_3^{4/3}}{\hbar^2}\cdot\frac{W_z^{2/3}}{v^2}\cdot\exp\left\{-\frac{C_3^{1/3}}{\hbar}\cdot\frac{W_z^{2/3}}{v}\right\}$	$e^{-\sqrt{\mu} k}$	$W_z^{2/3}\, e^{-W_z^{2/3} k}$
Stueckelberg C_4	$\frac{C_4}{R^4}$	$\frac{32\pi N_4 C_4^{5/4}}{\hbar^3}\cdot\frac{W_z^{7/4}}{v^3}\cdot\exp\left\{-\frac{C_4^{1/4}}{\hbar}\cdot\frac{W_z^{3/4}}{v}\right\}$	$\mu^{3/2} e^{-\sqrt{\mu} k}$	$W_z^{7/4} e^{-W_z^{3/4} k}$
Demkov	$e^{-\gamma u t/a_0}$	$4\frac{\gamma\hbar}{a_0}\cdot R_z^2\cdot\frac{v}{W_z}\cdot\exp\left\{-\frac{\pi a_0}{\gamma\hbar}\cdot\frac{W_z}{v}\right\}$	$\mu^{-1/2} e^{-\sqrt{\mu} k}$	$W_z^{-1} e^{-W_z k}$
Rapp & Francis	$\gamma\frac{R}{a_0} e^{-\gamma R/a_0}$	$\frac{9(1{\cdot}202)}{\pi}\cdot\frac{\gamma^2\hbar^4}{a_0^2}\cdot\frac{v^4}{W_z^4}$	μ^{-2}	W_z^{-4}
SLZ	–	$\pi R_x^2\int_0^{b_{max}} 2P(1-P)b\,db$, in which $P = \exp\left\{-\frac{2\pi\lvert H_{12}\rvert^2}{u\hbar\lvert H_{11}' - H_{22}'\rvert_{R_x}}\right\}$	$\mu^{1/2}$	$\Delta^{-9/4} e^{-k\Delta^{-1/4}}$ where $H_{12} = I R e^{-\gamma R/a_0}$

TABLE 5.2

Energy defect Δ_{max} cms^{-1}, at peak cross-section

	α_1, a_o^3 (Ref. 32)	Zn	Cd	Mg
α_2, a_o^3 (Ref. 33)	-	34.1	38.0	61.0
He	1.39	970	1,080	1,760
Ne	2.75	710	800	1,330
Ar	11.08	280	330	610

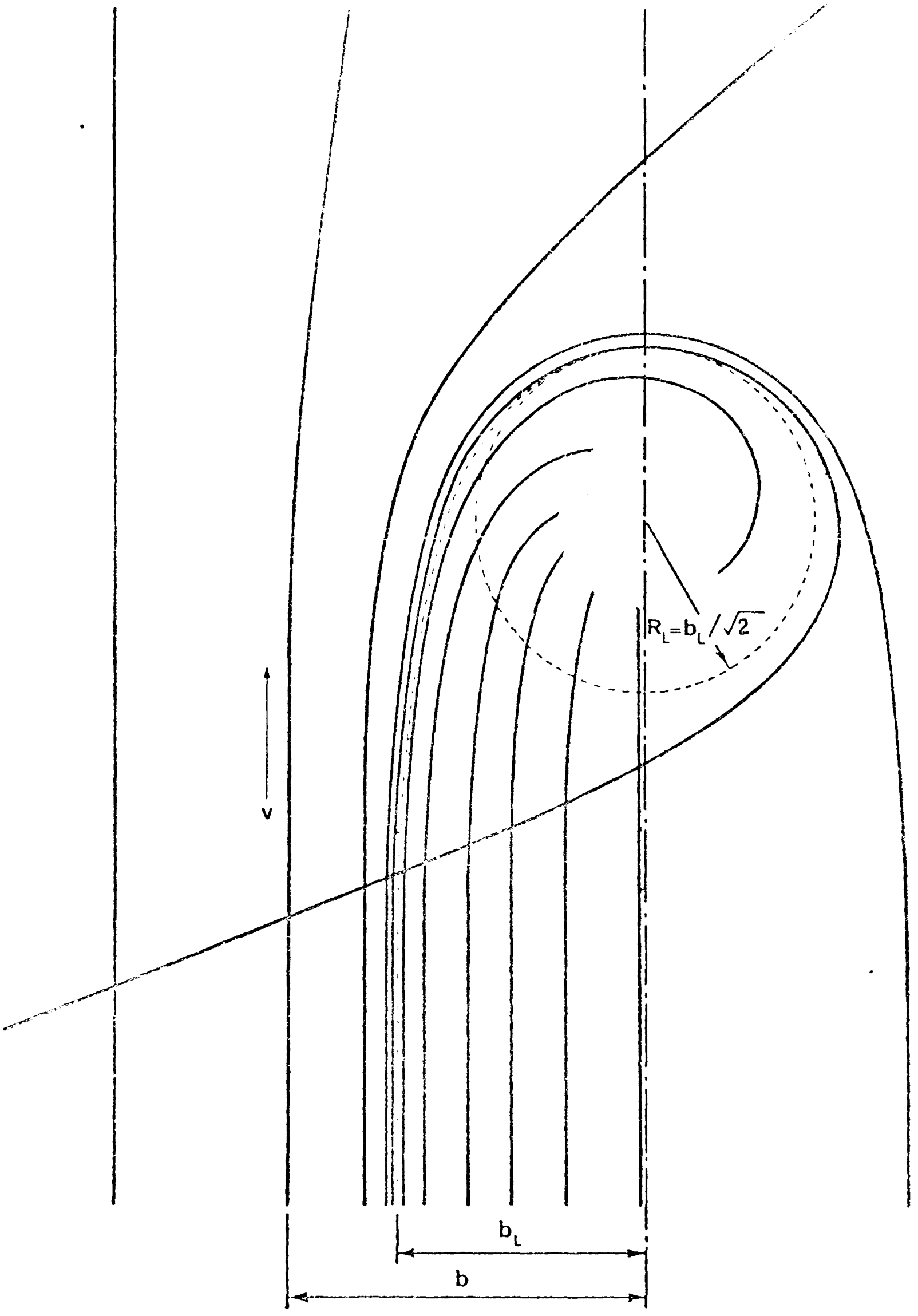

Figure 5.1 Family of trajectories for an inverse fourth power law of potential (reproduced from reference 5, Chapter 5)

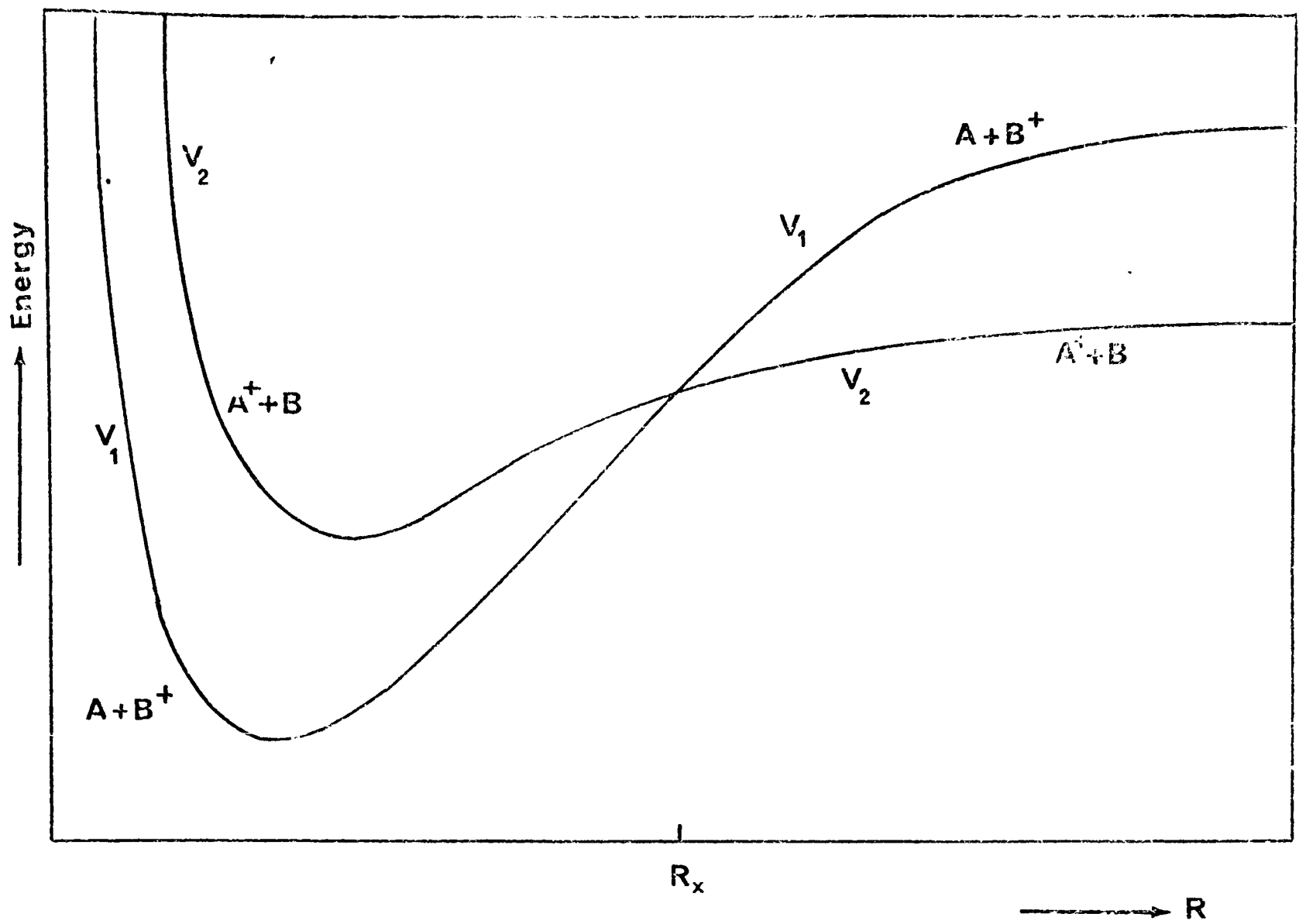

Figure 5.2 - Crossing of atomic energy levels

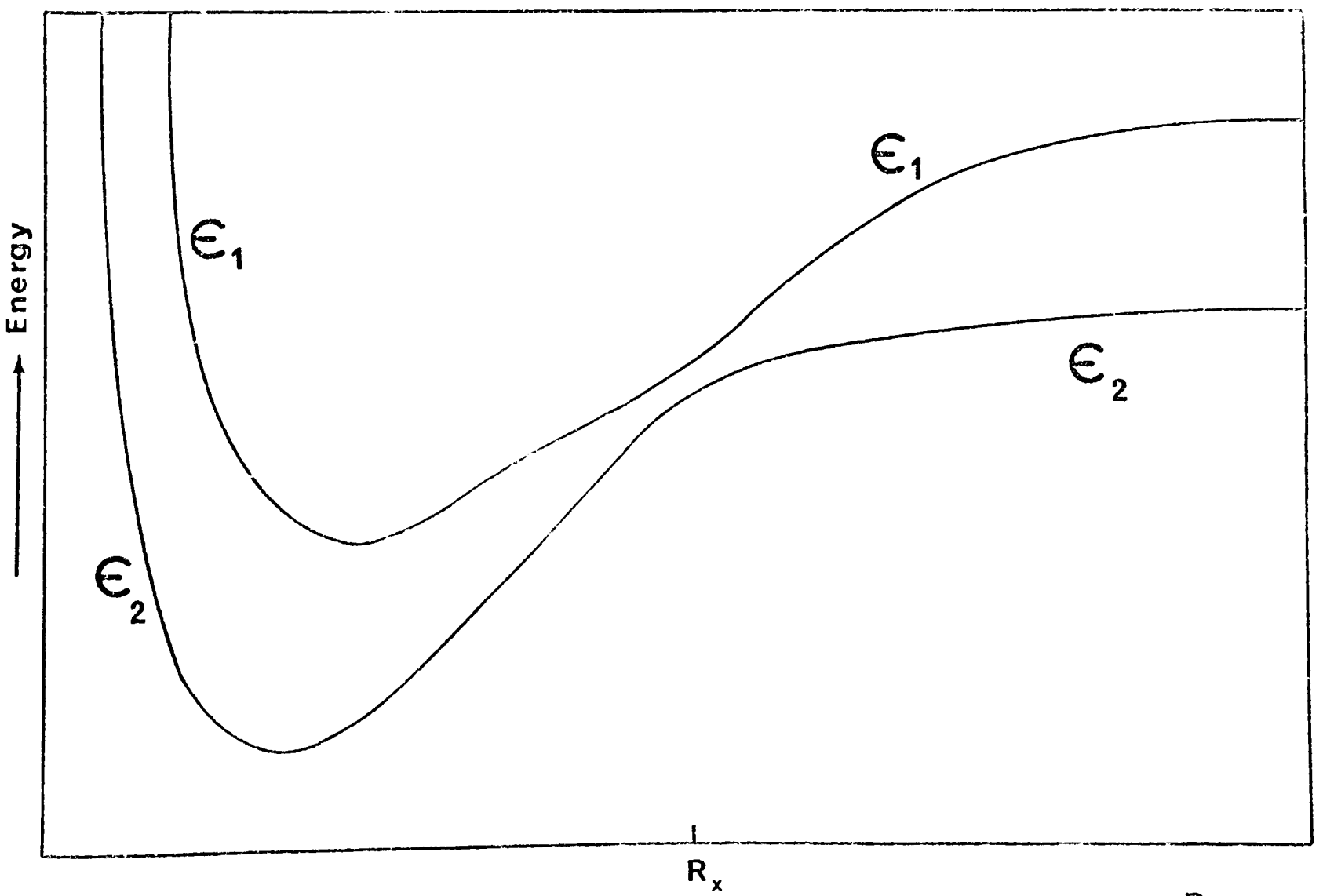

Figure 5.3 - Pseudo-crossing of molecular energy levels

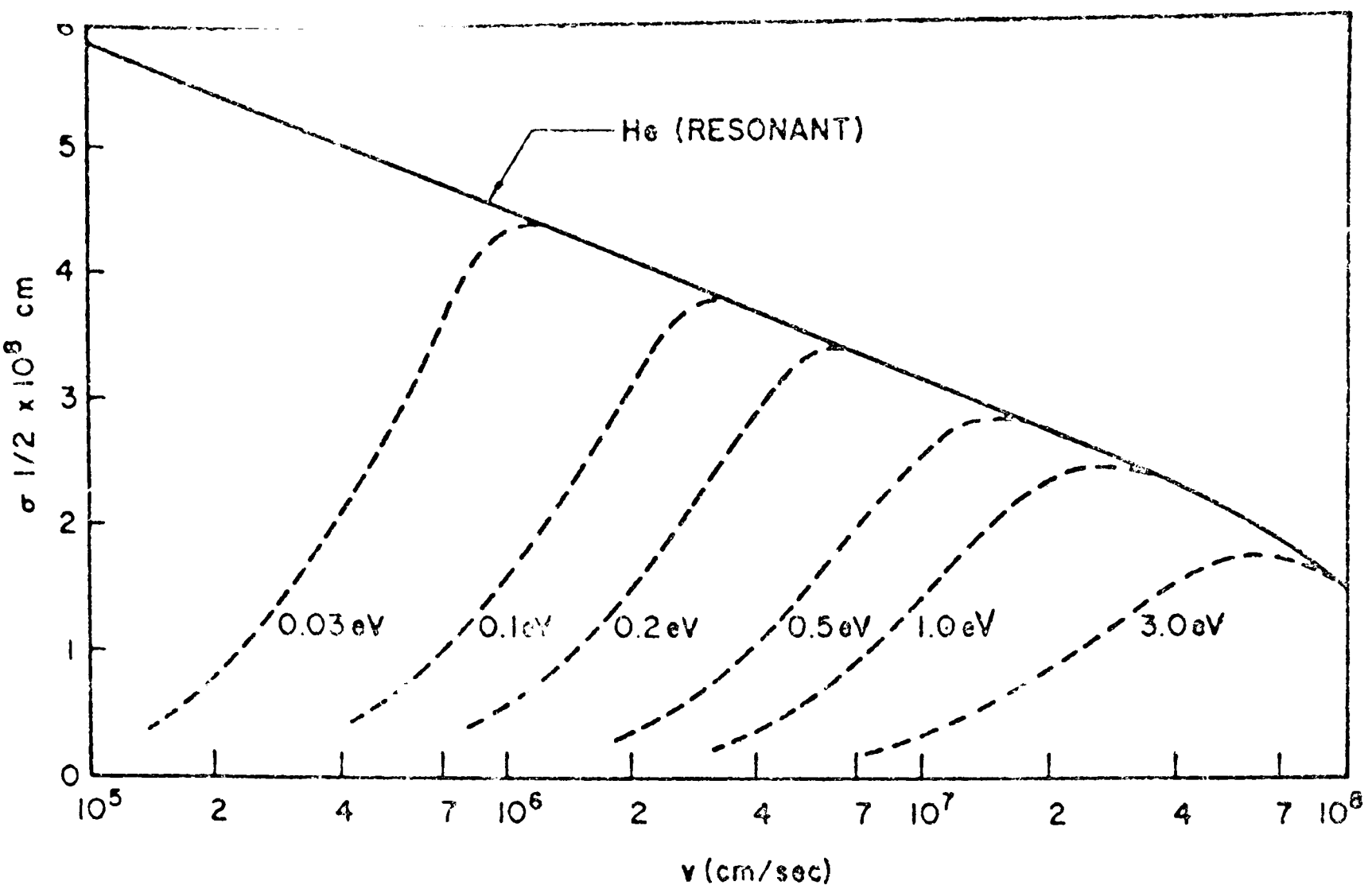

Figure 5.4 Velocity dependence of helium charge transfer cross-section for various W_z, Rapp and Francis model (reproduced from reference 12, Chapter 5)

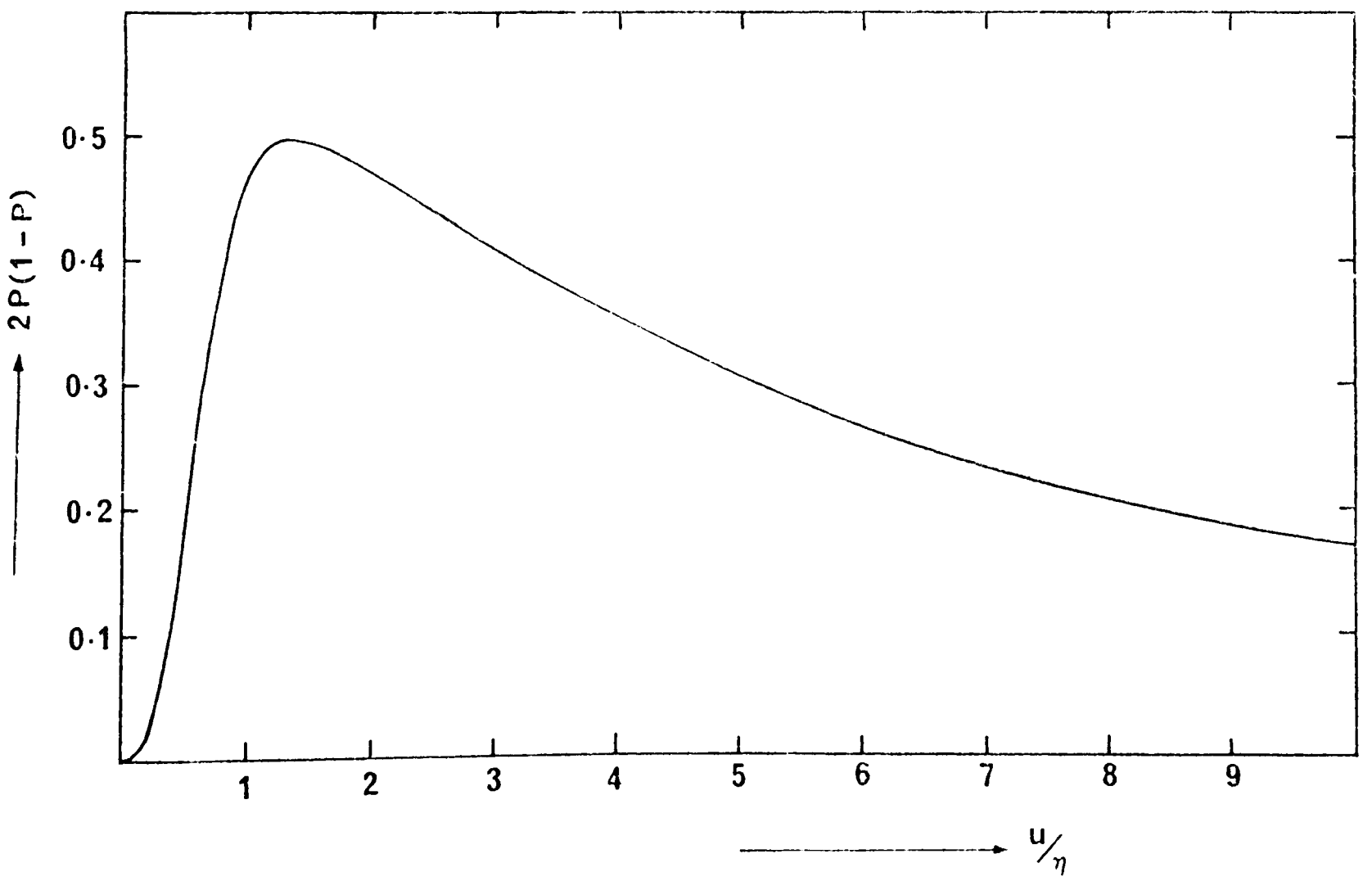

Figure 5.5 SLZ Transition Probability

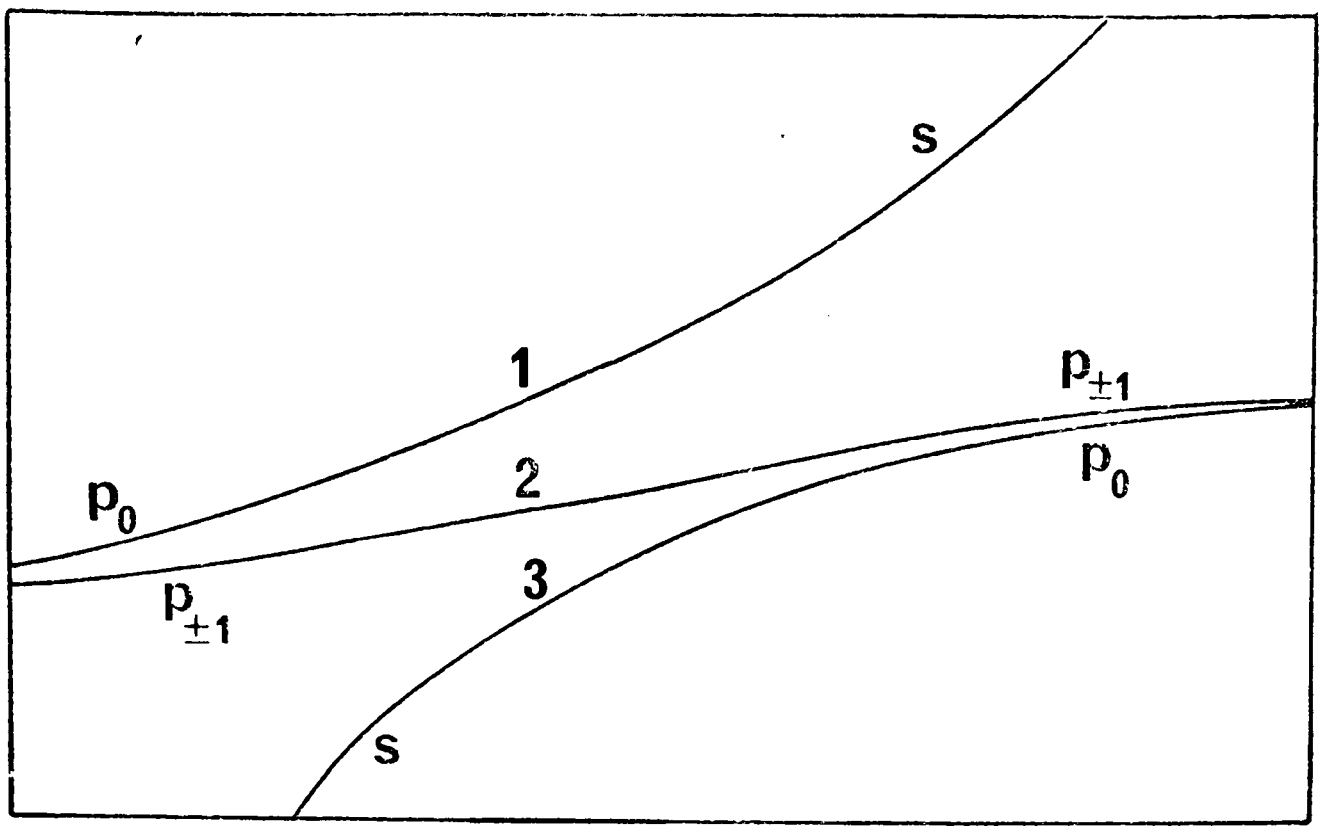

Figure 5.6 - Pseudo-crossing
involving non-s level

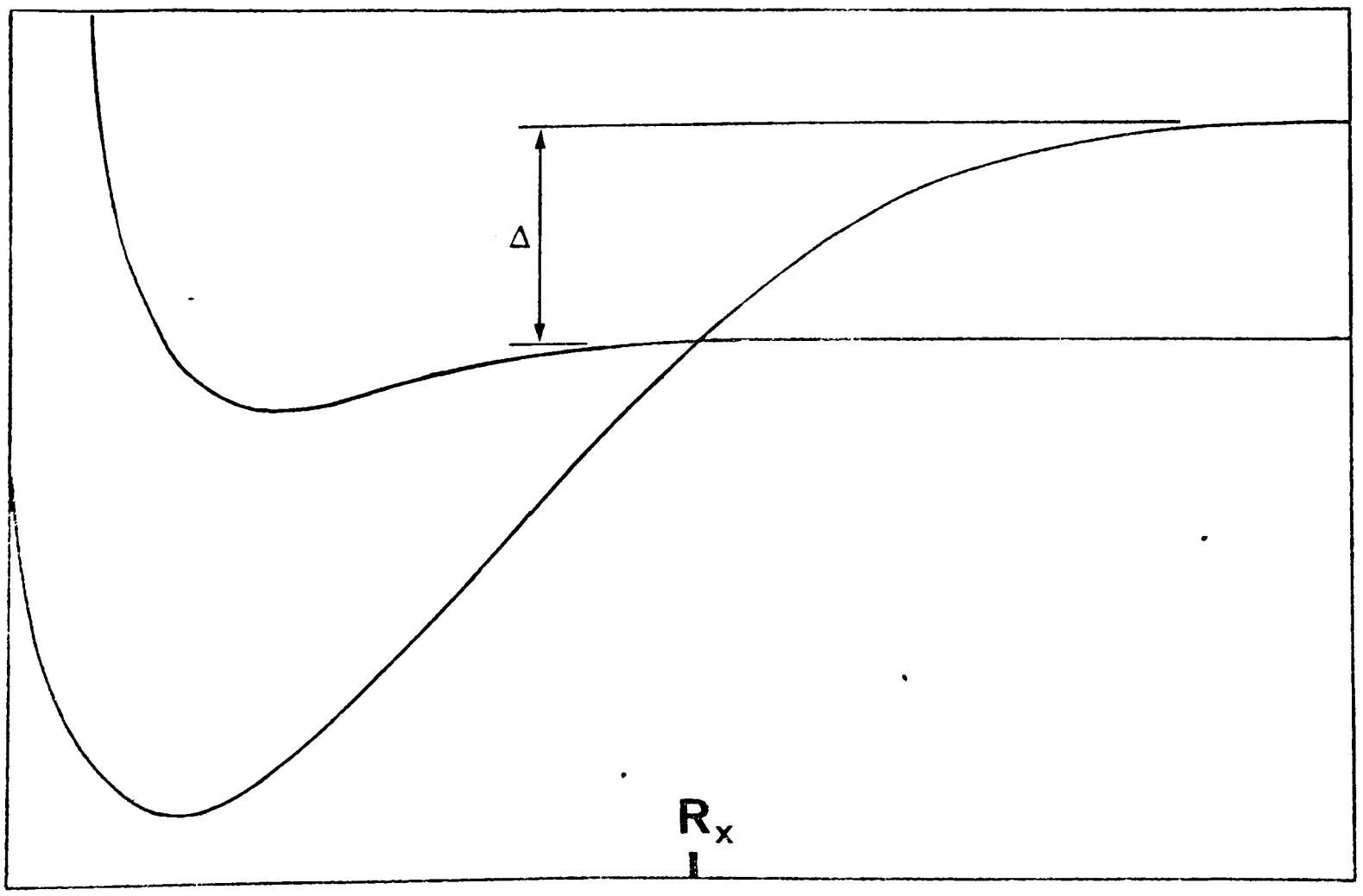

Figure 5.7 - Crossing of levels with $\alpha_2 \approx 0$

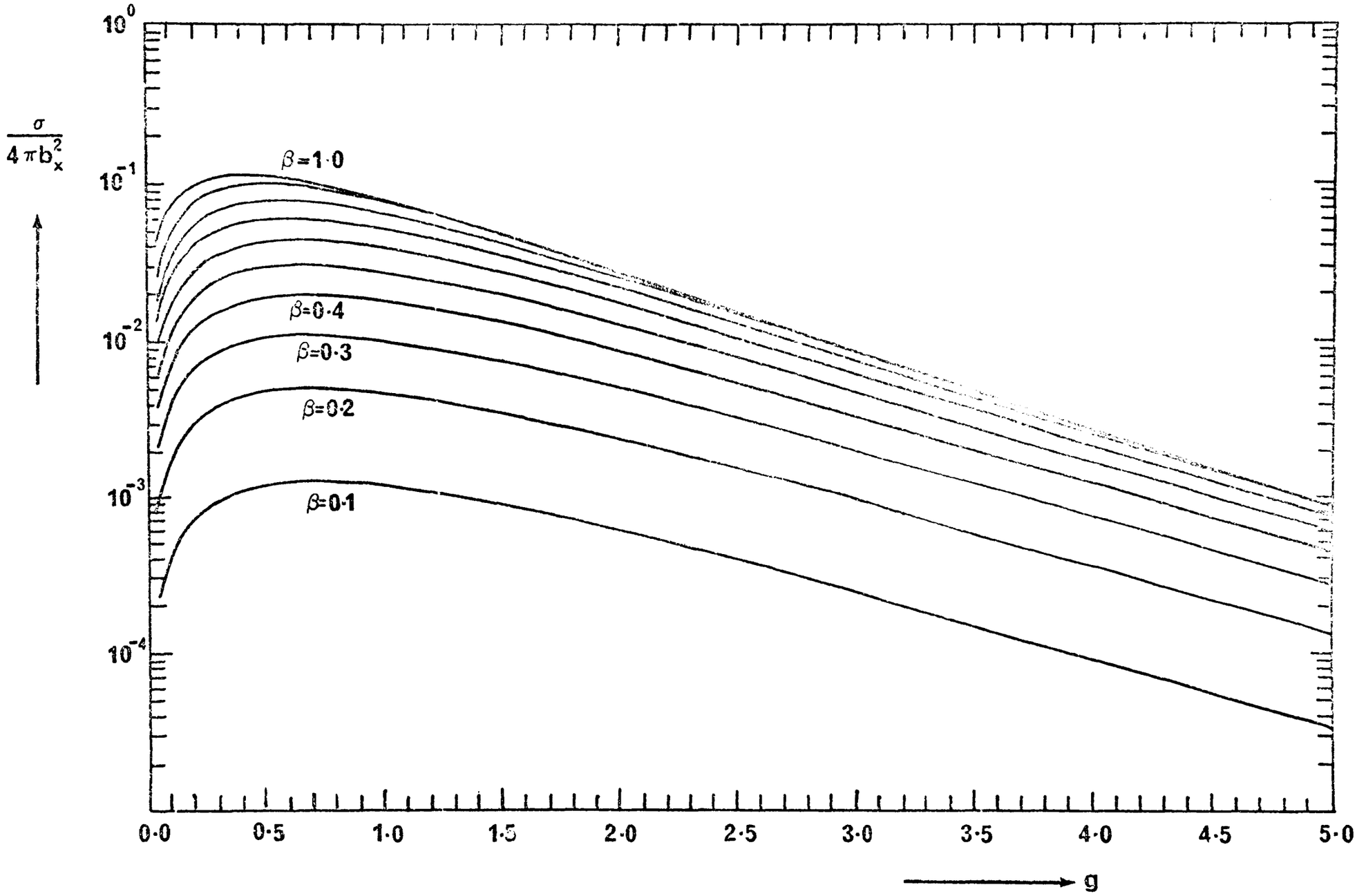

Figure 5.8 - Integral for SLZ formula,
Equations (5.26) and (5.29) (reproduced from reference 29, Chapter 5)

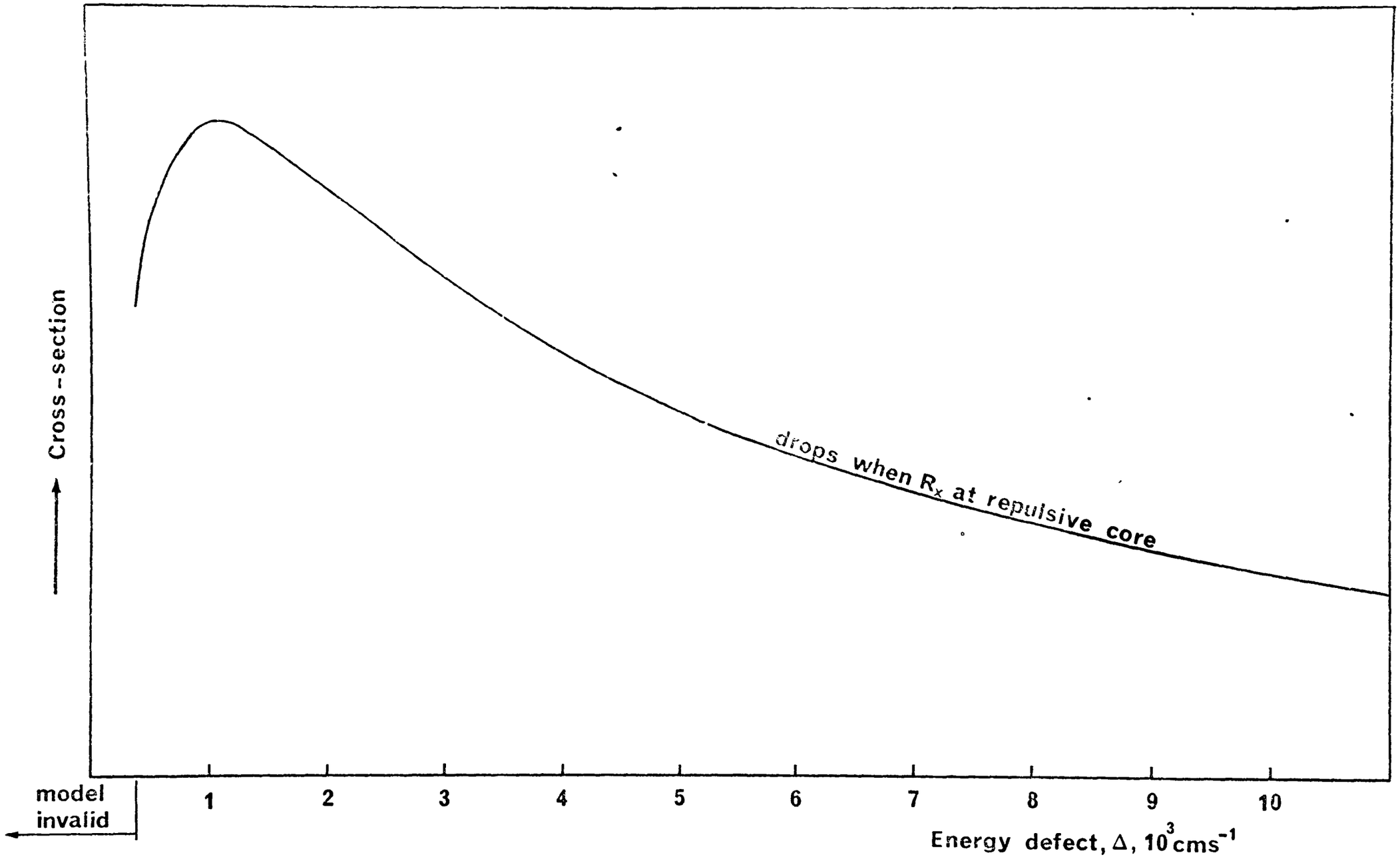

Figure 5.9 - Cross-section v. Energy defect for He - Cd charge transfer, based on an approximation to the SLZ formulation

CHAPTER 6

CONCLUSIONS

'The result proves the wisdom of the act'

Ovid

CHAPTER 6

Conclusions

6-1 STATISTICAL WEIGHT

A close correlation is apparent between the observed charge transfer rates (per unit statistical weight) to each level of the doublets of Zn II, Cd II and Mg II, indicated in column (12) of Tables 4.1(b), 4.2(b), 4.3(b) and 4.4(b). A measure of the correlation is given by the standard deviation of the rate per unit statistical weight from the mean of such rates into the doublet. The value of this deviation, calculated from the 14 doublets available, is 12%, which corresponds closely to the accuracy of the measurements themselves (Section 4-2.3). It is reasonable to conjecture, therefore, that charge transfer to each level is proportional to its statistical weight, and that when comparing excitation rates, it is the rate per unit statistical weight which should reveal some systematic dependence of cross-section on energy defect. This criterion is adopted in the following section.

A conspicuous exception to this rule is the $6p\ ^2P$ levels of Zn II from which the photon emission rates in the lines at 3171.5Å and 3178.6Å are in the ratio 1:8.8 instead of 1:2.3 predicted by considerations of statistical weight and branching ratio. No explanation for this anomalous behaviour can be offered at present. Notwithstanding, this doublet was included in the calculation of the standard deviation above.

6-2 ENERGY DEFECT

A theoretical estimate of the dependence of the charge transfer cross-section on energy defect, based on the highly simplified, semi-quantitative model developed in Section 5-4.3, is illustrated in Figure 5.9 for the helium-cadmium reaction. It shows the cross-section rising to a maximum at a positive value of energy defect of order 1000 cm^{-1}. The cross-section falls off at larger energy defects at a speed largely determined by the size of the repulsive core of the ion-atom system. The corresponding curve for the neon-magnesium reaction may be shown to be almost identical.

Corresponding experimental results are shown in Figure 6.1, in which charge transfer reaction rates for the helium-cadmium and neon-magnesium reactions are plotted together against energy defect. Only for these two reactions is it possible to present the results in this form because a) the results for the helium-zinc reaction are insufficiently numerous to enable a suitable normalising factor for the reaction rates to be estimated and b) the results for the helium-selenium reaction cannot be fully analysed (see Section 4-6). The general shape of the curve delineated by the results in Figure 6.1, is very similar to that shown in Figure 5.9, and therefore confirms the general conclusions of the theory with regard to the dependence of the cross-section on energy defect. In the light of the possibility, discussed in Section 4-3.2, that the neon-magnesium reaction may be assisted by a third body, it is perhaps surprising that the results for He-Cd and Ne-Mg can be normalised to define a curve of similar shape.

The enhancements observed by Duffendack and co-workers, illustrated in Figure 1.1, indicate behaviour largely consistent with excitation dominated by charge transfer reactions. However, an improbably high ion temperature would have to be postulated to account for population by charge transfer of the levels of large negative energy defect, claimed by the early workers. In the present experiments (but with the exception of selenium, see Section 4-6) charge transfer was observed to take place only to levels of positive energy defect, or small ($\sim kT_{gas} = 200\ cm^{-1}$) negative energy defect. The general rule would appear to hold that excitation by charge transfer cannot take place to levels of higher energy than the sum of the initial ion ground state energy and the energy of relative motion (which is also available for optical excitation[1]). This conclusion is no more than would be expected on the grounds of energy conservation.

In spite of the small amount of data which it is possible to collect for the helium-zinc reaction it would appear that the observed reaction rate to the 5d levels of Zn II is anomalously large. The explanation for this is not known, but, as zinc and cadmium have very similar electronic configurations, the absence of a corresponding

anomaly in the d levels of Cd II implies that the effect is not simply due to the influence of statistical weight or angular momentum.

6-3 SPIN

Schearer[2] has recently observed transfer of spin polarisation in Penning reactions of helium metastables in a flowing afterglow with various metals, including zinc and cadmium. His results have supported the prediction of the Wigner spin rule[3] that transfer of energy in atomic collisions is most likely between states which would conserve the total spin of the colliding system.

Application of the rule to the systems investigated here indicates that preferential excitation should take place to the doublet systems of Zn II, Cd II, Mg II and Pb II, the triplet system of Al II, the quartet system of Se II and the septet system of Mn II. In the case of zinc, cadmium magnesium and lead there are, in any case, few levels available in their quartet systems to test the rule. However, the triplet and septet systems respectively of aluminium and manganese were observed to be preferentially excited, despite the availability of levels in other multiplets for which the energy defect would appear to be closer to optimum.

No strong preference for the quartet system of selenium is revealed by the data in Tables 4.5. The behaviour of selenium presents a number of anomalies, however, sc that this evidence cannot be taken to invalidate the conclusion that the Wigner spin rule is at least fairly well obeyed.

6-4 REDUCED MASS

Theoretical predictions regarding the influence of reduced mass on charge transfer collisions differ from model to model.

The SLZ formulation predicts a reaction rate independent of reduced mass, while other formulations predict a reaction rate decreasing by different extents as the reduced mass is increased.

Unfortunately the influence of reduced mass cannot be inferred with any certainty from the experimental observations, because of the limited number of systems investigated. However, the charge transfer rate from neon was observed generally to be slightly smaller than that from helium, and in the few cases in which they might be expected to be rapid, reactions with argon were very much slower than either helium or neon.

6-5 3-BODY REACTIONS

There is good evidence that, in the case of reactions involving ground state helium ions, a third body does indeed influence the reaction rate into certain final levels (Section 3-7). In the case of reactions involving neon the experimental evidence is somewhat less conclusive (Section 4-3.2). Apart from the contrasting pressure dependence, however, the dependence of 3-body reaction rates on statistical weight, energy defect spin and reduced mass apears to be similar to that of 2-body reaction rates.

6-6 SUMMARY

The general conclusions of this study concern charge transfer reactions at thermal energies between rare gas ions and metal atoms, leading to the formation of metal ions in excited states.

The conclusions are:

i) The reaction rate is proportional to the statistical weight of the final excited level of the metal ion.

ii) The reaction rate is maximised for transitions to levels with an energy defect of order 1,000 cm^{-1} to 3,000 cm^{-1}.

iii) Reactions may occur with decreasing efficiency to levels with greater positive energy defects up to, and possibly exceeding, 8,000 cm^{-1}. Reactions do not take place to levels with an appreciable negative energy defect.

iv) Wigner's spin rule is fairly well obeyed.

v) The presence of a third body (a neutral atom) may enhance the reaction rate in certain cases.

The conclusions have been gathered from the study of a limited number of ion-atom systems and must inevitably remain somewhat tentative. Nevertheless, for the first time it has been demonstrated directly that thermal energy charge transfer excitation can occur with reasonable efficiency between a wide variety of collision partners. In addition, the dominant excitation mechanisms of the laser transitions in Cd II and Zn II have been classified unambiguously as either Penning reactions or charge transfer reactions. The factors which most significantly effect the efficiency of production of ions in excited states by thermal energy charge transfer have been established.

REFERENCES

1 Zapesochnyi, I.P., Zavilopulo, A.N. and Shpenik, O.B., Opt. Spec., 28, 465 (1970)

2 Schearer, L.D., Phys. Rev. Lett., 22, 629 (1969). See also Schearer, L.D. and Holton, W.C., Phys. Rev. Lett., 24, 1214 (1970)

3 Wigner, E., Gott. Nachr., 375 (1927)

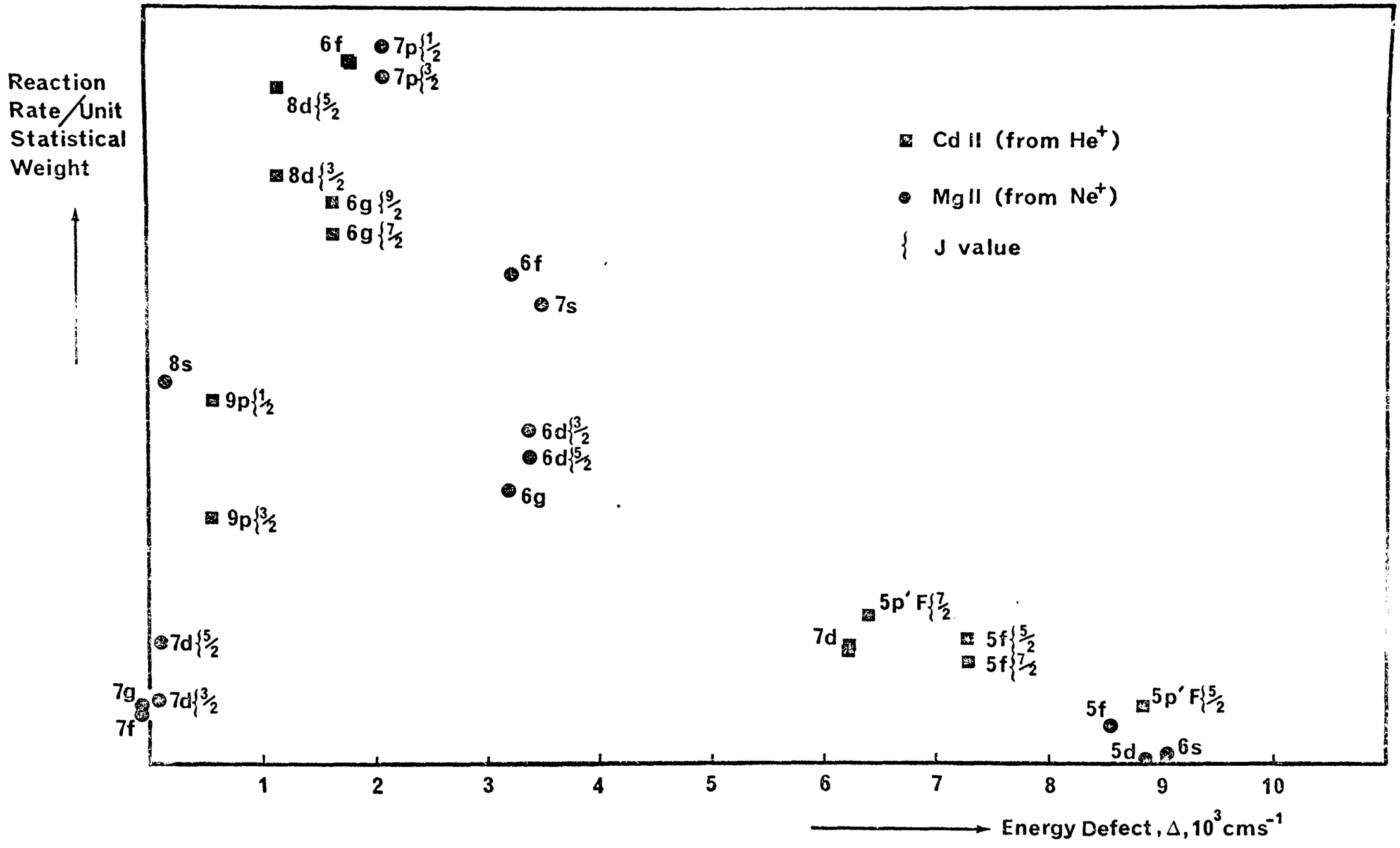

Figure 6.1 - Energy defect dependence of the Reaction Rates for He - Cd and Ne - Mg charge transfer

APPENDICES

'Impassion'd logic, which outran
The hearer in its fiery course.'

Tennyson

APPENDIX 1

FLOATING DOUBLE PROBES

An ideal double probe characteristic for probes of unequal area is shown in Figure A1.1. The theory of the floating double probe for probes of equal area given by Johnson and Malter[1] may be extended to the case of probes of unequal areas A_1 and A_2. The result is that the electron density, n_e, is given in terms of the sum of the saturation currents, I (defined in Figure A1.1), and the mean velocity of the ions, $\bar{v}$, by

$$n_e = \frac{4\,I}{(A_1 \quad A_2)\, e\bar{v}} \qquad (A1.1)$$

The ion temperature from which the mean velocity may be calculated may be taken to be 300K in the flowing afterglow.[2]

The electron temperature is given by the voltage difference, ΔV, between the intercepts of the tangent drawn to the characteristic, exactly half way between the saturation currents, and the asymptotes to the saturation currents (see Figure A1.1). Expressing the electron temperature, T_e, in terms of an equivalent voltage, where 1 volt corresponds to 11,600K, it can be shown that

$$T_e = \frac{\Delta V}{4} \qquad (A1.2)$$

The problem in finding the plasma density from Equation (A1.1) lies in determining the effective values of A_1 and A_2, which are strictly speaking the areas of the positive ion sheaths around the probes from which ions are collected. Bettinger and Walker[3] have derived an expression for the radius of the ion sheath about a cylindrical probe which is a linear function of [the probe voltage with respect to the plasma potential] raised to the power 0.75. The good saturation characteristics shown in Figure 3.3 confirmed that the

effect of the sheath was small. A good approximation to the correct saturation current for a collection area given by the probe dimensions can be found, therefore, by using the construction shown in Figure A1.2. In this, I is measured between the intercepts of the asymptotes to the saturation current with the origin of voltage, taken to lie at the centre of symmetry of the charateristic.

REFERENCES

1 Johnson, E.O., and Malter, L., Phys.Rev., 45, 3199 (1967)

2 Fehsenfeld et al. J. Chem. Phys., 44, 4087 (1966)

3 Bettinger, R.T., and Walker, E.H., Phys.Fluids, 8, 748 (1965)

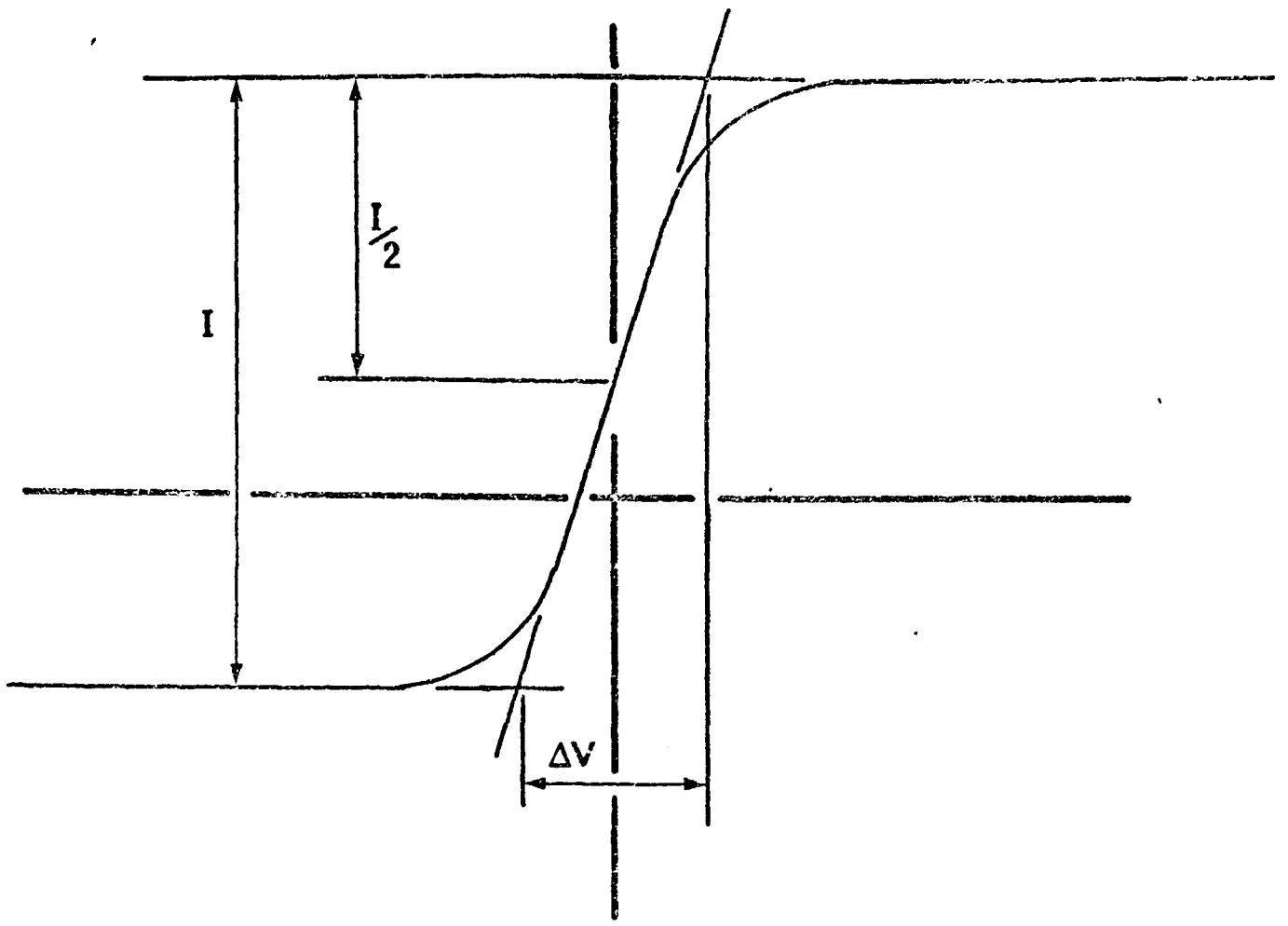

Figure A1.1 - Ideal assymetrical double probe characteristic

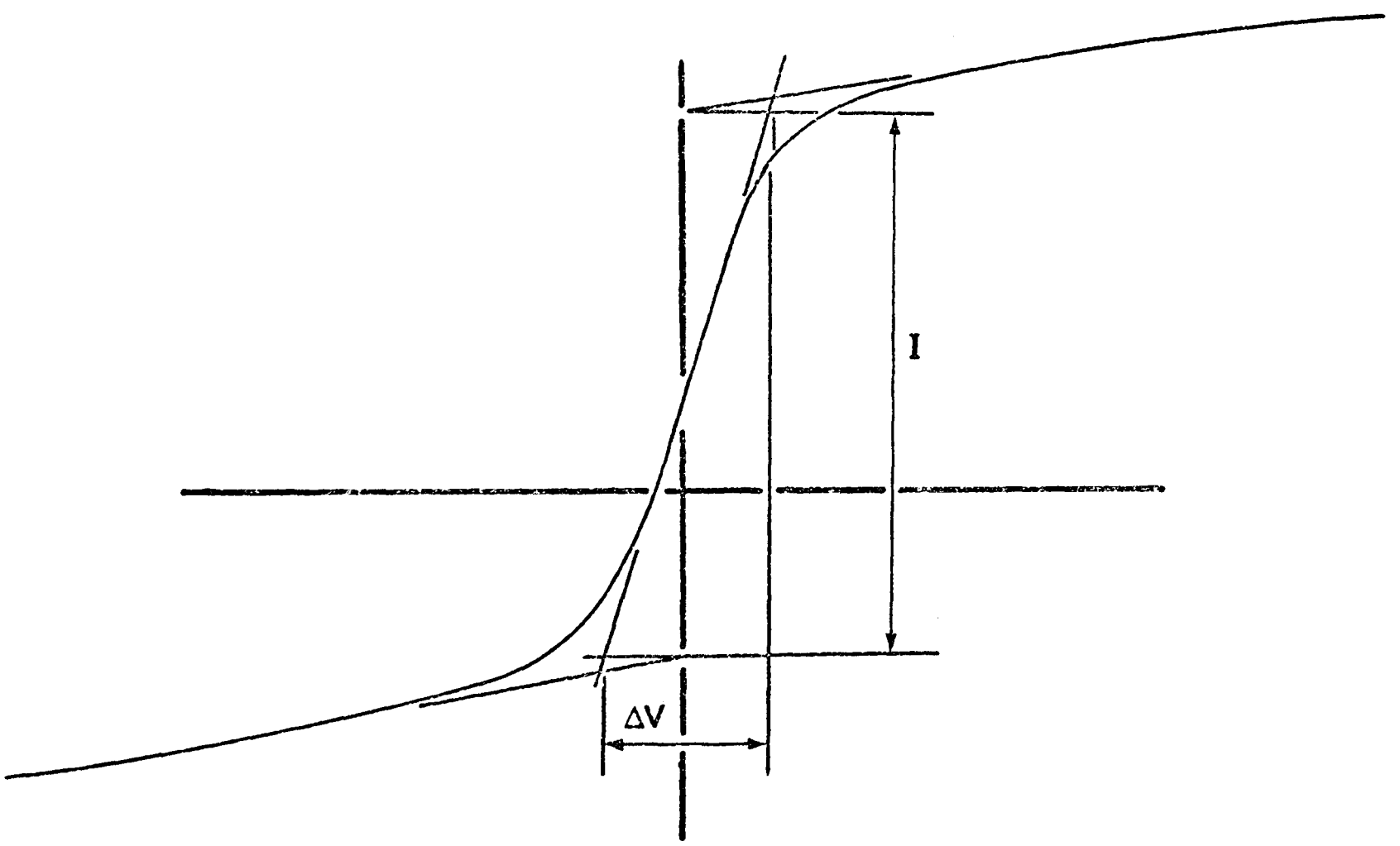

Figure A1.2 - Non-saturating double probe characteristic

APPENDIX 2

Orbiting limitations

The Langevin orbiting model, described in Section 5-2, divides orbits into two classes: those with closed orbits ($b < b_L$) and those with open orbits ($b > b_L$). This corresponds to the effect of a centrifugal barrier, illustrated by Figure 5.1.

If the tangential velocity is v_t, then a centrifugal barrier as defined in Section 5-3.7 occurs at R_b given by

$$\frac{1}{2}\mu v_t^2 = E_k + \frac{\alpha e^2}{2R_b^4} \qquad (A.2.1)$$

Conservation of angular momentum enables Equation (A.2.1) to be re-written

$$\frac{b^2}{R_b^2} E_k = E_k + \frac{\alpha e^2}{2R_b^4} \qquad (A.2.2)$$

This equation is a quadratic in Rb^2 which may be solved to give

$$R_b^2 = \frac{b^2}{2}\left(1 \pm \sqrt{1 - \frac{2\alpha e^2}{E_k b^4}}\right). \qquad (A.2.3)$$

If

$$\frac{2\alpha e^2}{E_k} > b^4 \qquad (A.2.4)$$

then R_b will be imaginary and no centrifugal barrier will exist. But the largest value of b which allows a crossing to be reached is b_x given by

$$b_x^2 = R_x^2 \frac{(\Delta + E_k)}{E_k}$$

$$= \sqrt{\frac{\alpha e^2}{2\Delta}} \frac{(\Delta + E_k)}{E_k} .$$

Substituting b_x for b in the inequality (A2.4) it is found that R_x lies outside the centrifugal barrier when $E_k > \Delta$. In this case β, the maximum value of b/b_x, is unity. When this condition is fulfilled, integration over all impact parameters will include a large or dominant contribution due to orbits which are virtually rectilinear.

If, however, $\Delta > E_k$ then a centrifugal barrier is important for $Rb > R_x$. In this case R_x will only be reached when the condition for no centrifugal barrier is fulfilled, that is $b^4 < \frac{2\alpha e^2}{E_k}$. In this case b_{max} will be given by

$$b_{max}^4 = \frac{2\alpha e^2}{E_k} \qquad \text{(A2.5)}$$

which yields a value for $\beta = \frac{b_{max}}{b_x}$ given by

$$\beta^2 = \frac{2\sqrt{E_k \Delta}}{(\Delta + E_k)} \qquad \text{(A2.6)}$$

Comparison of Equation (A2.5) with Equation (5.3) shows that $b_L = b_{max}$. The Langevin orbiting model as applied in Section 5-2 will, therefore, yield the cross-section for the SLZ formula which occurs when P=0.5.

APPENDIX 3

Existence of a Critical Zone

The following calculation, which is similar to the work of Smith and Olson (Chapter 5, Ref. 11) is designed merely to assess the probable importance of the zone formulation and is not intended to be an accurate analysis.

The calculations are made in atomic units and are based on the model

$$H_{12} = \rho e^{-\rho}, \qquad \text{(A3.1)}$$

in which $\rho = R\gamma$

and

$$W(R) = \Delta - \frac{\delta\alpha}{2R^4} = \Delta - \frac{\delta\alpha\,\gamma^4}{2\rho^4}. \qquad \text{(A3.2)}$$

The condition for a critical region to exist is

$$2\,|H_{12}| \geqslant |W(R)| \qquad \text{(A3.3)}$$

One obvious solution to Equation (A3.3), true at all R, is W(R)=O. This corresponds to the narrow critical region about a crossing. The boundaries of a critical zone will be given by the solution to the following equation, derived from Equations (A3.1), (A3.2) and (A3.3):

$$2\,|\rho e^{-\rho}| = \left|\Delta - \frac{\delta\alpha\,\gamma^4}{2\rho^4}\right| \qquad \text{(A3.4)}$$

If the critical zone is outside a crossing then $\Delta > \frac{\delta\alpha\,\gamma^4}{2\rho^4}$ and in most cases the approximation $\Delta = |W(R)|$ will be valid. If the critical zone is inside a crossing, then $\Delta < \frac{\delta\alpha\,\gamma^4}{2\rho^4}$ in which case (A3.4) is well approximated by

$$\rho^5 e^{-\rho} = \frac{\delta\alpha\,\gamma^4}{4} = \delta\alpha\, I^2 \qquad \text{(A3.5)}$$

Now $\rho^5 e^{-\rho}$ has a maximum value of about 21.1. In most cases of interest $\delta\alpha\, I^2 > 21.1$, so that no critical zone exists.

A similar argument applies in the case of ion-quadrupole attraction.

ACKNOWLEDGEMENTS

The author would like to express his gratitude to:

Professor B. Bleaney, F.R.S. for the facilities of the Clarendon Laboratory during the course of the work.

Dr. C.E. Webb for his supervision and for his unfailing encouragement and guidance at all stages of the work.

Dr. J.H. Sanders for his continued interest in the work and for his supervision during the initial period of study.

Mr. J.M. Green for his cheerful assistance in the more onerous tasks of research and for developing the computational techniques required to produce the theoretical values listed in the tables in Chapter 4.

Dr. F.T. Smith for disclosing the results of his theoretical calculations and for helpful discussions.

Dr. L.D. Schearer for disclosing the results of his own observations of charge transfer reactions in flowing afterglows and for interesting discussions.

Dr. J.R. Moore, Dr. O.C. Jones and staff at the N.P.L. for advice on optical calibration procedures and for calibrating the standard lamps.

Mr. G.A. Krivacska for his skilled and intelligent assistance in making the metal components of the apparatus.

The technical staff of the Clarendon Laboratory for excellent tuition and advice in technical matters and for their willing assistance at all times.

Mrs. Heather Majoo for so patiently decyphering and presenting the manuscript.

The Ministry of Defence, Navy Department (C.V.D.) for financing the research and the Science Research Council for providing financial support for the author.